UNIVERSITÀ DEGLI STUDI DI MILANO

SCUOLA DI DOTTORATO

FISICA, ASTROFISICA E FISICA APPLICATA

DIPARTIMENTO DI FISICA

CORSO DI DOTTORATO DI RICERCA IN

FISICA, ASTROFISICA E FISICA APPLICATA

CICLO XXV

Radio-Frequency Generation of an Electron Plasma in a Malmberg-Penning Trap and its Interaction with a Stationary or Pulsed Electron Beam

Settore Scientifico disciplinare FIS/03

Tesi di Dottorato di:

Muhammad Ikram

Supervisore: Dr Massimiliano Romé

Coordinatore: Prof. Marco Bersanelli

Anno Accademico 2013-2014

COMMISSION OF THE FINAL EXAMINATION

1) Prof. Francesco Pegoraro
   Department of Physics, University of Pisa, Italy

2) Prof. Giuseppe Gorini
   Department of Physics, University of Milano Bicocca, Italy

3) Dr. Marco Cavenago
   INFN Laboratori Nazionali di Legnaro, Italy

Final examination
Date: March 28, 2014

Università degli Studi di Milano, Dipartimento di Fisica, Milano, Italy

Acknowledgements

I am grateful to Prof. Marco Bersanelli, the director of PhD school of physics astrophysics and applied physics university of Milan and the examination committees of the XXV cycle for admission to the PhD courses for providing me with the opportunity to pursue a Ph.D. in plasma physics group.

I would like to heartiest thanks of my supervisor Dr. Massimiliano Rome, whose friendly attitude; practical advice and fruitful discussion contributed enormously to the success of this thesis possible. I acknowledge useful discussions with Prof. Roberto Pozzoli, Dr. Giancarlo Maero, Dr Bruno Paroli and Prof. Franca De Luca of Plasma Physics Group, Department of Physics, University of Milano.

I would also like to thanks Dr. Marco Cavenago, INFN Laboratori Nazionali di Legnaro, Prof. Pegoraro, university of Pisa and Prof Giuseppe Gorini, university of Milano Bicocca for reading the manuscript of my Ph.D. thesis and giving me valuable comments.

I offer special thanks to the Andrea Zanzani (secretary of PhD school) and Dr Bruno Paroli for their cooperation on very short notice at numerous occasions during my stay in Milano.

Thanks to Francesco Cavaliere director of the mechanical workshop and members staff Daniele Vigano, Attilio Gandini for the constant and fundamental contribution in experimental research work.

I am thanking to professor Dr. Robert E. H. Clark University of Texas San Antonio (UTSA), USA for his continuous encouragement advices time-to-time as well as fruitful scientific and daily life discussions.

I personally obliged to chairman emerging nation science foundations (ENSF), Professor K. Tahir Shah and his team for their remarkable contribution to promote scientific research and sustainable technological development in emerging nations across the world. I thanks to get two-travel grant from the ENSF to attend doctoral admission examination and to return to Islamabad from South Korea to proceed to attend PhD School, Department of Physics at University of Milano.

I particularly owe my deepest gratitude to my sweet father Ghulam Sarwar (late) who was one of education loving person. I always remember his continuous meeting and discussions with my school/college teachers in connection of my educational output, shortcoming and improvement. I am thanking of my love-full mother, brothers professor Muhammad khan, Bashir Muhammad and sisters for their valuable teachings, love, and blessings, which always help me to achieve my goals.

It will be unfair if I not thanks to my caring wife Neelofar for her affection, her support and most importantly her patience during our stay in via Risorgimento 161, Sesto rondo Milano. My lovely daughter Laiba born on dated 13 January 2014 was very excitement movement for my wife and me during the tough time of writing of this thesis. I would like to dedicate this thesis to all of them.

In general, during my stay and experiences here I feel pleasures to say that Italy is my second home country.

Muhammad Ikram Safi

Abstract

Experiments and numerical investigations on trapped electron plasmas and traveling electron bunches are discussed.

A Thomson backscattering diagnostics set up was installed in the ELTRAP (Electron TRAP) device, a Penning-Malmberg trap operating at the Department of Physics of the University of Milano since 2001. Here, an infrared (IR) laser pulse collides with nanosecond electron bunches with an energy of 1-20 keV traveling through a longitudinal magnetic field in a dynamical regime where space-charge effects play a significant role. The backscattered radiation is optically filtered and detected by means of a photomultiplier tube. The minimum sensitivity of the backscattering diagnostics has been estimated for the present set-up configuration. Constraints on the number of photons and thus on the information one can obtain with the Thomson backscattering technique are determined by the relatively low density of the electron beam as well as by noise issues. Solutions to increase the signal level and to reduce the noise are briefly discussed.

The generation of an electron plasma by stochastic heating was realized in ELTRAP under ultra-high vacuum conditions by means of the application of low power RF (1-20 MHz) drives on one of the azimuthally sectored electrodes of the trap. The relevant experimental results are reviewed. The electron heating mechanism has been studied by means of a two-dimensional (2D) particle-in-cell (PIC) code, starting with a very low electron density, and applying RF drives of various amplitudes in the range 1-15 MHz on different electrodes. The axial kinetic energy of the electrons is in general increasing for all considered cases. Of course, higher temperature increments are obtained by increasing the amplitude of the RF excitation. The simulation results indicate in particular that the heating is initially higher close to the cylindrical wall of the device. These results on the electron heating point in the same direction of the experimental findings, where the plasma formation due to the ionization of the residual gas is found to be localized close to the trap wall. The simulations indicate also major heating effects when the RF drive is applied close to one end of the trap. Similar results are obtained for an electron plasma at higher densities, simulating a situation in which the RF is applied to an already formed plasma.

With the aim to extend these RF studies to the microwave range, a bench test analysis has been performed of the transmission efficiency of a microwave injection system up to a few GHz. The

test was based on the use of a prototype circular waveguide with the same diameter and length of the ELTRAP electrode stack and of a coupled rectangular waveguide with dimensions suitable for a future installation in the device.

Electromagnetic PIC simulations have also been performed of the electron heating effect, again both at very low and relatively high electron densities, applying a microwave drive with a frequency of approximately 3 GHz close to the center and close to one end of the trap.

Both the bench test of the injection system and the numerical simulations indicate that the new microwave heating system will allow the extension of the previous RF studies to the GHz range. In particular, the electron cyclotron resonance heating of the electrons will be aimed to increasing the electron temperature, and possibly its density as a consequence of a higher ionization rate of the residual gas. The installation of the new RF system will open up the possibility to study, e.g., the interaction between the confined plasma and traveling electron bunches.

Table of Contents

Chapter FOUR

Waveguide design and microwave injection bench test

Chapter FIVE

Numerical simulations of the RF heating of a non-neutral plasma in a Penning-Malmberg trap

Chapter SIX

Summary

List of Figures

List of Tables

Chapter ONE

1.1 Overview of non-neutral plasmas

A considerable progress has been made in the physics of non-neutral plasmas with the use of Penning traps in the last few decades. Penning traps have gained increasing importance also in the field of experimental nuclear physics and play an important role in many other fields, like the study of nuclear structure and beam physics. E.g., there are a variety of applications for trapped positrons in Penning-like traps, such as the study of the electron-positron plasmas, the search for resonance states in electron-positron scattering experiments, positron annihilation studies, the production of low emittance positron beams and the formation of anti-hydrogen [14-18]. In a different research field, the investigation of electron plasmas in carefully prepared conditions turns out to be equivalent to direct experiments on two-dimensional, almost dissipation-less, fluids. Thus, basic fluid dynamics issues often connected with a variety of applications can be studied using traps for electron plasmas. Non-neutral plasma physics play an important role in beam transport systems and coherent radiation devices such as free electron lasers, cyclotron auto-resonance masers and magnetrons. Pulsed electron beams are used in a wide range of applications, for example to generate coherent X-rays in free electron laser (FEL) and in Thomson back-scattering X-ray sources. Electron beams are also used to generate intense ion beams with electron-beam-ion-sources (EBIS).

Reviews of the physics of non-neutral plasmas are available in two remarkable books by Ronald C. Davidson entitled "*Theory of non-neutral plasmas*" (Benjamin, 1974) and "*Physics of non-neutral plasmas*" (Imperial College Press and World Scientific, 2001). A general review about trapped pure electron plasmas can be found in the papers by T. M. O'Neil [4-10].

1.2 Physics of a single-component plasma in a Penning Trap

A non-neutral plasma is a many-body collection of charged particles in which there is not overall charge neutrality. Such systems are characterized by intense self-electric fields (space-charge

fields), and in high-current configurations by intense self-magnetic fields. Examples of non-neutral plasma systems include:

1. One-component nonneutral plasmas confined in Malmberg-Penning traps.
2. Intense charged particle beams and charge bunches in accelerators, transport lines, and storage rings.
3. Coherent radiation sources (magnetrons, gyrotrons, free electron lasers).

Non-neutral plasmas have a number of experimental advantages over their neutral counterparts. Due to the conservation of canonical angular momentum (see next section), the radial diffusion of a non-neutral plasma is strongly limited, allowing for theoretically infinite confinement times. Most experimental studies are conducted in cylindrically symmetric Penning traps, in which radial confinement is achieved by a homogeneous magnetic field and axial confinement is achieved by an externally imposed electrostatic potential well formed by negative (electrons trapping) or positive (ions trapping) biasing two cylindrical electrodes. The behavior of the plasma depends on the quality of vacuum used in the experiments. E.g., in the ELTRAP apparatus operating at the Department of Physics of the University of Milano, three different pumps working efficiently in different regimes of pressure are used to achieve ultra-high vacuum conditions. A first volumetric scroll pump, a turbo-molecular pump and an ion pump allow to reach a working pressure in the vacuum chamber of $\left(10^{-8} - 10^{-9}\right)$ mbar.

Non-neutral plasma exhibit a wide range of collective properties like neutral plasmas, such as plasma waves, instabilities, and Debye shielding. For example, the dispersion relation for Langmuir waves in a pure electron plasma is the same as that in a neutral plasma (except for the Doppler shift associated with the rotation of the electron plasma). Non-neutral plasma exhibit also Debye shielding [11, 17].

1.3 Confinement theory and limitation

Despite the presence of a self-repelling electric field, it is easier to confine a non-neutral plasma than to confine a neutral plasma. The radial confinement of a non-neutral plasma can be understood in terms of the total canonical angular momentum, given by

$$P_\theta = \sum_{i=1}^{N}\left[m v_{\theta i} \mathrm{r_i} + \frac{qB}{2} r_i^2 \right] \quad 1.1$$

where $m, v_{\theta i}, r_i \; and \; q_i$ are the mass, azimuthal velocity, radial position, and charge of the i_{th} particle, respectively. For a sufficiently high magnetic field, the vector potential contribution in the angular momentum dominates over the mechanical part. Hence

$$P_\theta \approx \frac{\mathrm{qB}}{2} \sum_{i=1}^{N} r_i^2 \quad 1.2$$

For a cylindrically symmetric system, the total canonical angular momentum P_θ is a constant of motion. Thus, the mean squared radius of a collection of like-charged particles is constant. Only a small fraction of the particles in such a collection can escape to a large radial position; the rest will always remain confined. Therefore, non-neutral plasmas are unique in the sense that the conservation of total canonical angular momentum provides a limitation on the allowed radial positions of the particles: if no external torques act on the plasma, the plasma cannot expand to the walls and in principle it can be confined forever. The theorem states that the sum $\sum_{i=1}^{N} r_i^2$ can change significantly only as a result of external torques and since the angular momentum of each particle depends on its sign of charge, electrons and ions can move to the wall together while the sum is preserved.

In practice there are some additional issues with the radial confinement of a plasma within a Penning trap. The most important of these issues are machine construction errors, field imperfections and collisions with the background gas (electron-neutral collisions). E.g., a fraction of neutrals (typically H_2) is always present inside the trap, and the collisions between the neutrals and the charged plasma column applies a torque which can alter the mean squared radius of the charged particles and allow the plasma to expand. This causes the collection of like charged particles to have a finite confinement time. The presence of unavoidable field imperfections is also the source of external torques which allow some of the plasma to reach the wall by increasing its mean square radius. This means that P_θ is, for any realizable trap, only approximately a constant of the motion. However, by minimizing field errors and maintaining a good vacuum to minimize

the effect of neutrals, confinement times of several days have been achieved for pure nonneutral plasmas [4, 6].

1.4 Motivation

The Penning-Malmberg trap ELTRAP has been used in the past for the study of collective modes on low-temperature electron plasmas. Recently, the device has been modified in order to perform studies on the dynamics of space-charge dominated low-energy (1–20 keV) nanosecond (4–5 ns) electron bunches produced by a photocathode source illuminated by a pulsed ultraviolet (UV) laser. Plasma collective effects tend to break the spatial coherence of charged particles beams, determining a fundamental limit on the beam brightness obtainable in accelerating devices. The control and diagnostics of these collective behaviors are therefore very important to achieve and maintain the desired beam properties. The longitudinal dynamics of the electron bunches has been characterized with different diagnostics, like electrostatic pick-ups and an optical system based on a phosphor screen and a Charge-Coupled Device (CCD) camera. The presence of longitudinal space-charge effects has been evidenced even at relatively low bunch density of $n_b = 4.3 \times 10^8 cm^{-3}$. The minimum sensitivity of the diagnostics was estimated in two different set-ups of the Thomson backscattering diagnostics by measuring the noise and computing the expected signal with a theoretical estimate of the scattered photons in relativistic regime. In the first set-up the laser beam was maintained collimated and the interaction could be moved in principle along the drift-tube. In the second set-up the laser is focused in a particular point to optimize the solid angle and the number of collected photons. In the first set-up (with a collinear laser injection) a sensitivity of 14 photoelectrons was estimated (for a bunch laser matched interaction), corresponding to a density of $10^{11} cm^{-3}$, while in a second set-up (with a focused laser injection) the measured sensitivity was 7 photoelectrons for a density of $3.6 \times 10^{10} cm^{-3}$. These result shows that the present bunch density is three order of magnitude less than the desired density.

The primary focus of this research work was to evaluate the sensitivity of the system installed in the ELTRAP device to perform the Thomson backscattering experiment. A series of upgrades have been implemented or are under way, aimed at increasing the signal to noise ratio (S/N). The solutions to increase the signal level and to reduce the noise issues are briefly discussed in chapter

2. These noise issues include the residual stray light of the UV and IR laser beam, the coherent noise produced by the IR and UV laser discharges and the electronic noise.

Numerical investigations performed by means of a commercial two-dimensional particle-in-cell code clarify the process of generation of an electron plasma by means of the application of a RF electric field to one of the trap electrodes under ultra-high vacuum conditions, observed in the experiments at low drive frequencies (1-20 MHz) and predict the plasma heating resulting from high frequency (cyclotron) drives (2-3 GHz). In addition to simulation studies a bench test analysis has been performed of the RF transmission efficiency of a RF injection system up to a few GHz to be installed in the Malmberg-Penning trap (ELTRAP) for the generation and heating of an electron plasma. The new heating system will allow the extension of the previous RF studies to the GHz range. In particular, resonant cyclotron excitation of the RF-generated plasma will be aimed at increasing the electron temperature and possibly its density as a consequence of a higher ionization rate of the residual gas. In the prospected solution the installation of the new RF system will open up the possibility to study, e.g., the interaction between the confined plasma and a traveling electron bunch.

1.5 Layout of the thesis

The remainder of the thesis is organized as follows:
Chapter 2 contains a description of the Malmberg–Penning trap (ELTRAP) apparatus and the major tools employed in the Thomson backscattering diagnostics, an estimate of the minimum sensitivity of the diagnostics and the possible improvements to be implemented in order to get the desired signal to noise ratio (S/N).

In chapter 3, studies of the wave-particle interactions in a non-neutral plasma are presented. The evidence of the electron plasma generation in ELTRAP by means of a low power radio frequency (RF) drive in the MHz range (1-20 MHz) applied on one of the trap electrodes under ultra-high vacuum (UHV) conditions is demonstrated. The theory of stochastic heating through a Fermi acceleration mechanism is also briefly examined.

In chapter 4, the design of the microwave transmission apparatus is briefly described. The microwave injection has been studied in a prototype circular waveguide, with the same

geometrical parameter (diameter 9 cm and length 102 cm) as that of the electrode stack of the ELTRAP device. The technical issues are properly addressed. Attenuations, waveguide modes transform and excitation technique are described. The details of power flow measurements devices as well as the transmission efficiency and return loss measurements are presented to predict the input and output power in ELTRAP.

Chapter 5 deals with Particle-In-Cell simulations of the RF heating of an electron plasma in a Malmberg-Penning trap. A realistic geometry of the ELTRAP device is used and the numerical simulations are used to clarify the underlying mechanisms involved in previous experimental measurements. Finally, conclusions are given in chapter 6.

Chapter TWO

Experimental system and Thomson backscattering diagnostics

2.1 The Malmberg-Penning trap ELTRAP

The ELTRAP device installed at the Department of Physics of the University of Milano is a Malmberg-Penning trap, with a magnetic field up to 0.2 T, equipped with a charge coupled device optical diagnostics. It is intended to be a small scale facility for electron plasma and beam dynamics experiments, and in particular for the study of collective effects, equilibrium states, and the formation of coherent structures in these systems [58]. Modifications and updates have been implemented in ELTRAP aimed at performing studies on the dynamics of space-charge dominated nanosecond electron bunches traveling along the magnetic field. In particular, a Thomson backscattering apparatus has been developed where an infrared (IR) laser pulse collides with the bunched electron beam. The frequency shifted backscattered radiation, acquired by means of a photomultiplier (PMT), can be exploited to evaluate information on energy, energy spread and density of the bunch. The achievable sensitivity of the diagnostics has been estimated, and valuable information on the main parameters affecting the signal-to-noise (S/N) ratio has been obtained.

In this chapter a brief description of the experimental set-up (trap electrodes assembly, vacuum system, magnetic field, electron source, 2D beam scanner, etc.) are given. A schematic description of the Thomson backscattering diagnostic for the study of nanosecond electron bunches in high space-charge regime and its challenging limitations as well as an estimate of the ELTRAP set-up minimum sensitivity of present experimental system are also presented.

2.2 Electrode assembly

The electrode assembly of the ELTRAP device consists of ten OFHC (oxygen-free high conductivity) copper cylinders, which are mounted (independently) on a holding aluminum (Al) bar held at ground as shown in figure 2.1. Eight cylinders (C1 to C8) have a length of 9 cm while electrodes S2 and S4, azimuthally sectored into two and four patches, respectively, have a length of 15 cm. All electrodes have a diameter of 9 cm and the inter-electrode spacing (obtained with macor insulators) is 1 mm. Two of the cylinders are segmented azimuthally, allowing the detection and/or the excitation of azimuthal charge perturbation modes: One cylinder has two insulated sectors, positioned 180° from each other, and the other four insulated sectors (S4, shown in figure 2.2), at 90° from each other. The electrode stack is housed in a stainless-steel vessel kept at pressures in the ultra-high vacuum range $\left(10^{-9}-10^{-8}\right)$ mbar to reduce collisional effects. The axial confinement of electrons is provided by negative voltages applied to two electrodes, and the resulting length of the plasma column can be varied from about 18 to 80 cm.

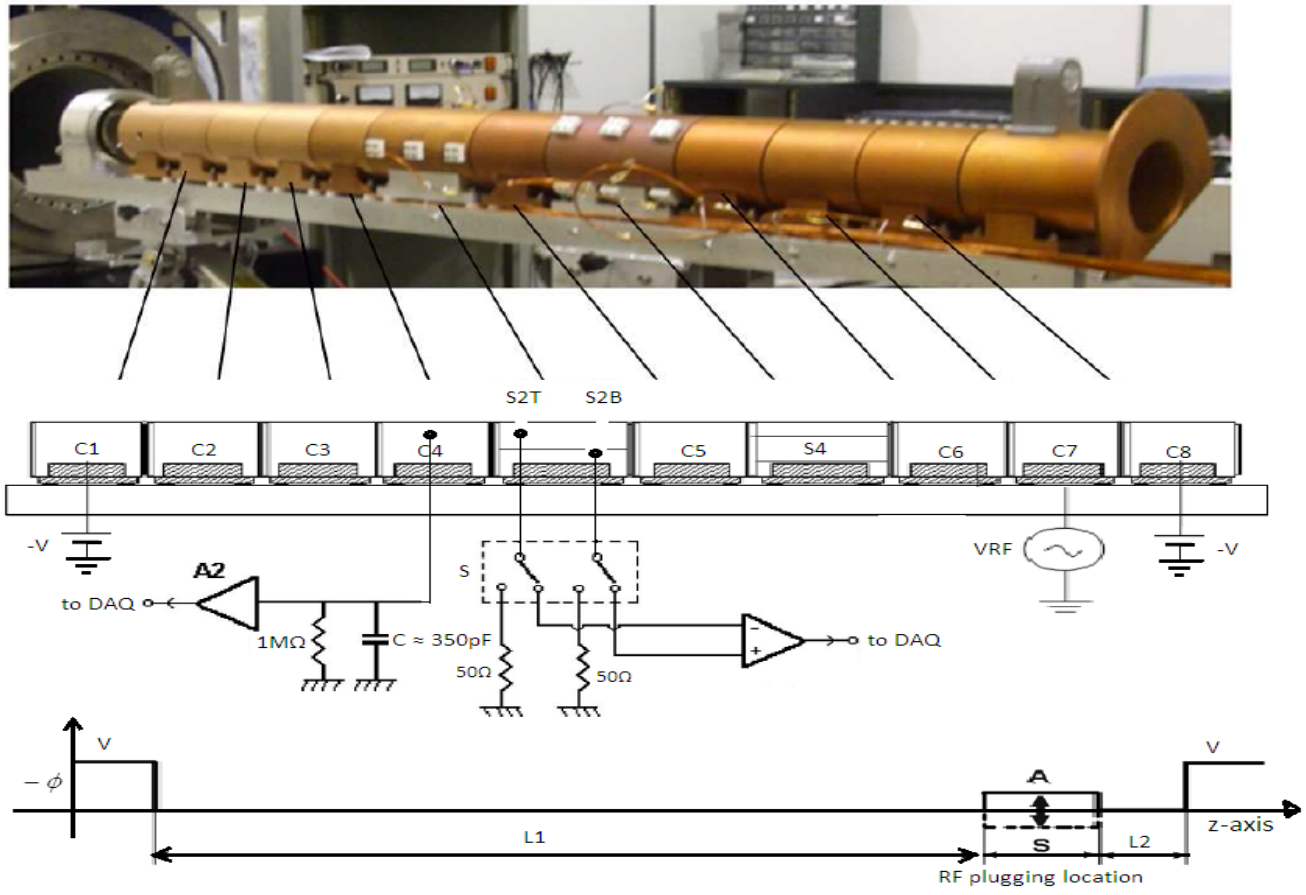

Figure 2.1 Picture and schematic of the internal OFHC electrodes assembly aligned and mounted on an aluminum bar, with the circuits used to measure the induced charge signals induced (e.g., on electrodes S2 and C4). Bottom: indicative scheme of the electrode potentials, with confinement between electrodes C1 and C8 biased at a negative voltage V and RF drive of amplitude 'A' on C7.

Figure 2.2 Picture of an azimuthally four sectored electrode, built of four insulated parts.

The potentials on the electrodes are controlled by an eight-channel waveform generator (time resolution 100 ns, voltage range ±100 V). All electrodes are connected with coaxial kapton insulated wires, compatible with high and ultra-high vacuum situations, with an impedance of 50 Ω. These transmission lines were measured and characterized with a reflectometry sending a pulse with a FWHM of 8 ns and receiving the reflected signal with an oscilloscope with 1 GHz bandwidth. These measurements are needed when the required bandwidth is limited by mismatches in the cable-feed through transitions and by the electrode capacitances. These effects becomes significant for frequencies greater than a few hundred MHz and are of fundamental importance in our case, to eliminate spurious effect of the distortions in the signal produced by the fast electrostatic beam diagnostics.

2.3 Vacuum system

A 25 cm diameter and 175 cm long vacuum tube, made of AISI 316L stainless steel to minimize magnetic field perturbations, encloses the electrodes. The chamber is equipped with a pumping system composed by three different pumps working efficiently in different regimes of pressure to achieve UHV conditions. A first volumetric scroll pump reduces the atmospheric pressure to about 10^{-3} mbar, a turbo-pump then reduces the pressure to about 10^{-7} mbar and an ion pump stabilizes the working pressure of the vacuum chamber at $\left(10^{-8}-10^{-9}\right)$ mbar. The turbo and the ion pumps can be isolated from the main chamber by means of an electro pneumatic stainless steel valves. These can be used, e.g., to increase the residual gas pressure in order to study the effect of collisions with neutrals on transport processes. The pressure in the chamber is measured with

three different vacuum gauges: a convection gauge working at a pressure ≥ 10^{-3} mbar, a cold cathode Penning type gauge working at ≥ 10^{-8} mbar and a nude ionization gauge working below 10^{-6} mbar. Since the pumping speed changes for different gases, the residual gas in the chamber should be mainly composed by molecules like Hydrogen and noble gases. Baking processes with heating bands that promote the degassing from the chamber walls are used to reach the final pressure in a shorter time.

2.4 Magnetic Field

The magnetic field used for the radial confinement of the electrons is generated by a normal-conducting solenoid of length 1.5 m with an inner diameter of 32 cm, corrected by 4 shims and 16 dipole coils, in order to obtain a large uniform magnetic field region. The solenoid consists of different layers of conductors connected in series and cooled by parallel water fluxes. In addition, the solenoid is enclosed in a soft iron cage made of two square end plates and twelves axial bars: this simplifies the support system, and also represents a shield against the Earth's magnetic field. The solenoid current is generated and controlled by a digitally controlled power supply with a current drift $\left(\frac{dI}{dt} = 10^{-5} A/h\right)$, a maximum current of ≤ 600 A and a maximum voltage of ≤ 120 V.

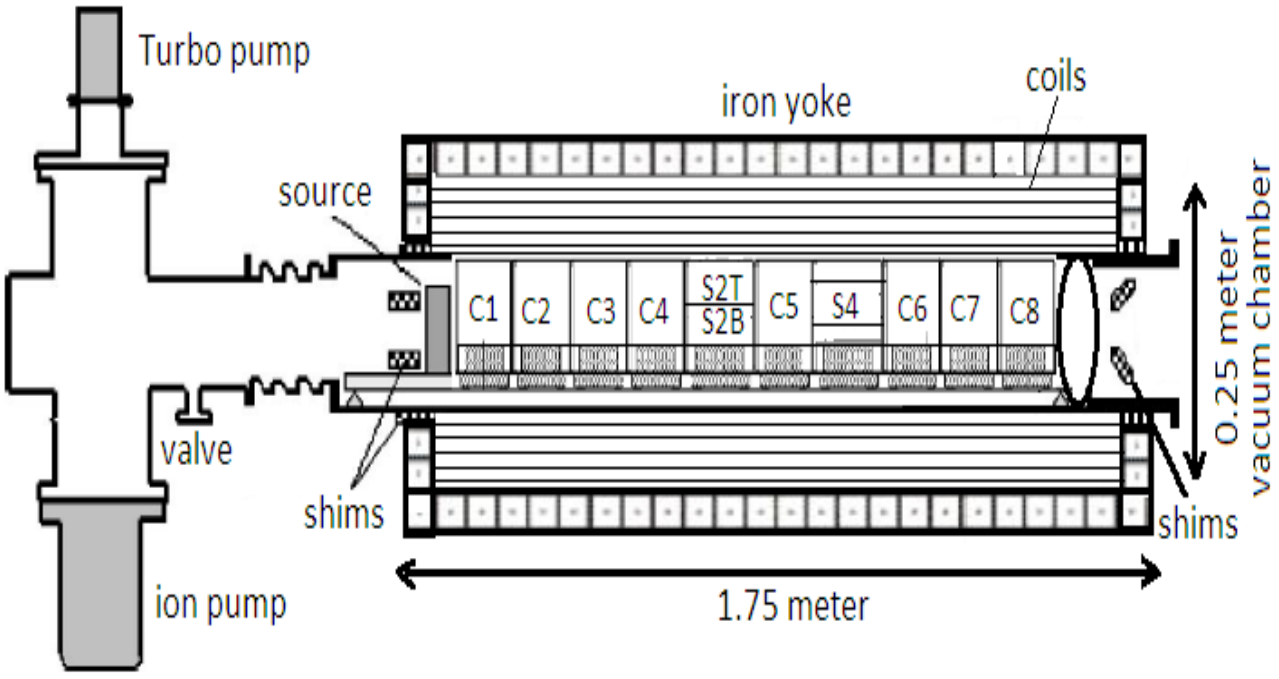

Figure 2.3 Schematic of the cylindrical electrodes assembly within the vacuum chamber with the reentrant flange, the pumping system and the solenoid with the iron yoke of ELTRAP. The iron

structures used to generate the magnetic field and some shims positioned at the coil ends concentrate the field's lines to the axis. The coil is made of three windings connected in series.

The maximum magnetic field strength obtained in the central region is 0.2 T. The field uniformity is better than 10^{-3} within a distance (from the center of the magnet) of 50 cm, and within a radius of 5 cm around the axis. Four additional dipolar coils are used to correct the axial direction of the main magnetic field. The schematic of the cylindrical electrodes assembly within vacuum chamber with a reentrant flange, the pumping system and the solenoid with the iron yoke of the ELTRAP device is shown in figure 2.3.

2.5 Electron source and 2D beam scanner

The source used for the generation of electron bunches is a barium-impregnated tungsten photocathode positioned at the end of the vacuum chamber and aligned to the geometrical axis of the trap. The properties of the electron bunches right after the emission are determined by the main parameters of the incident laser, the target (electron source) and the extraction geometry. We used a 337 nm ultraviolet (UV) nitrogen gas laser with a pulse duration ≤ 4 ns, an energy per pulse ≤ 400 mJ and a repetition rate up to 30 Hz. The laser is aligned to the source by means of movable UV silica mirrors. The laser beam has an original size of 7 × 7 mm reduced by a circular pin-hole to a diameter of 5 mm. The UV laser impinges on the photocathode mounted on an alumina body with an active area of diameter 6.35 mm. An internal heater, supplied by a current generator in the 0 – 2 A range, is used to reach the working temperature of $900-1200\ ^{0}C$ needed for the surface activation of the source. The whole target and its housing are set to a negative electrostatic potential of 1−20 kV, so that an electron cloud is extracted out of the source as a quasi-monochromatic bunch by a simple extractor made of a grounded plate with a central hole of 12 mm diameter (anode ring). Stationary beams can also be produced by thermionic emission, heating the photocathode at a higher temperature. The photocathode is immersed in an auxiliary magnetic field, generated by two Helmholtz coils, that can be raised to 50 G, with a 0.5G uniformity over a distance of 13mm from the emitter. This auxiliary magnetic field provides the initial focusing of the electrons. Then the bunch enters in the region with the main magnetic field where its original spot-size is radially compressed. The bunch should then interact with a high power Nd:Yag laser beam (≈1 J energy per pulse and 1064 nm wavelength) in the vacuum chamber.

Due to misalignments of the photocathode source and to small inhomogeneities of the magnetic field, the electron bunch reaches the end of the electrode stack with an appreciable offset (detected by means of a phosphor screen in previous experiments). The spatial matching between the laser beam and the electron bunch is ensured by an automated steering system. After aligning the IR laser beam with the trap mechanical axis, a radially movable Faraday cup is centered on the axis with the help of the IR laser itself. Then the bunch trajectory can be corrected by means of a so-called beam scanner. This is an electronic circuit that adjusts the currents flowing in two orthogonal sets of dipole coils in the transverse plane (by means of two synchronized sawtooth signals so that the bunch trajectory is steered in both X and Y directions). The two sets of correcting dipoles wound around the main solenoid (see figure 2.5) steer / deflect the bunch trajectory until the bunch transverse position reaches the interaction point. The optimal values of the currents are set by maximizing the electron beam charge signal detected by the Faraday cup. A schematic diagram of the self-alignment digitally controlled beam scanner, the electron source, the UV and IR laser and the Faraday cup is shown in figure 2.4 [64].

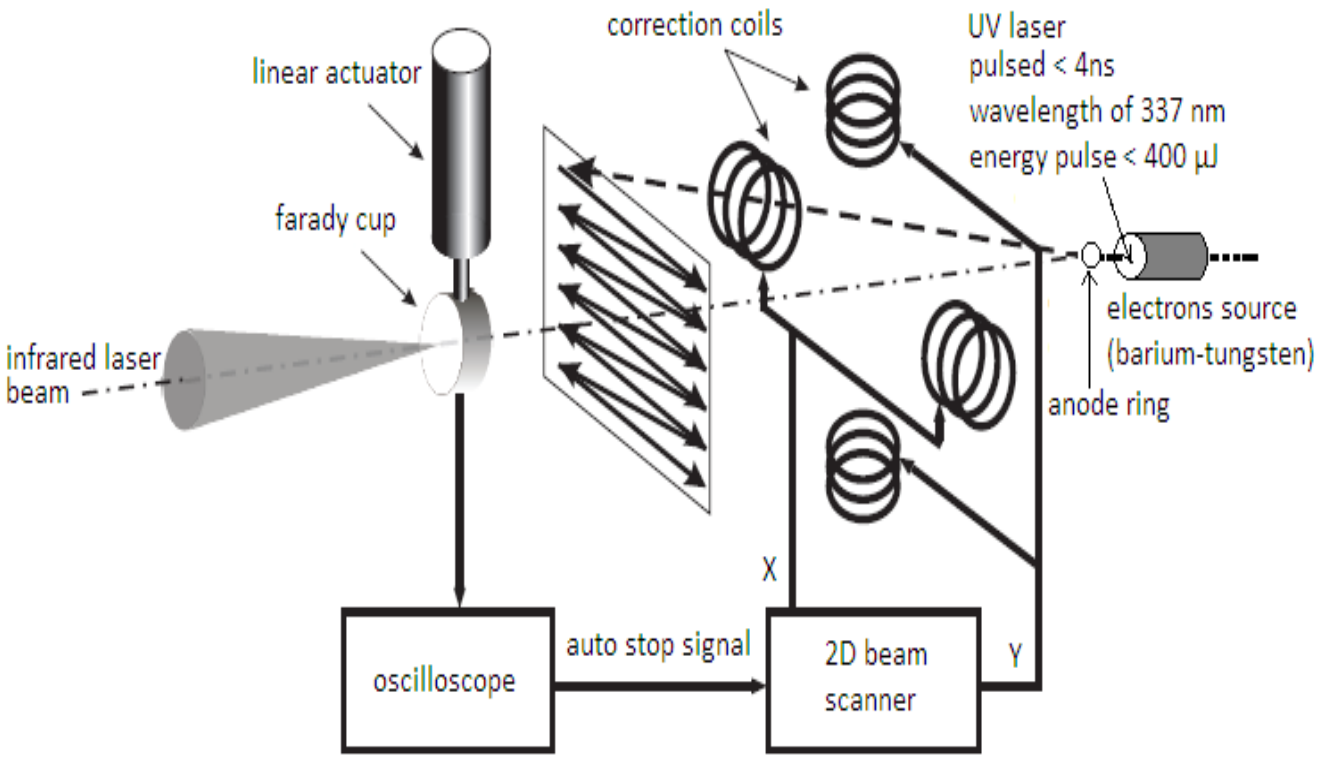

Figure 2.4 Schematic of the digitally controlled 2D beam scanner system for the electron bunch alignment at focal point of the infrared laser beam on the geometrical axis of the trap.

2.6 Thomson Backscattering diagnostics and limitations

The ELTRAP device was originally a trap for non-neutral plasmas but it was used here for the study of the dynamics of nanosecond electron bunches in high space charge regime with a Thomson backscattering diagnostics. The developments in high-power lasers, optical technologies and photon-counting techniques have made possible the use of this technique even in relatively low-temperature plasmas with electron densities down to a few $10^{10} cm^{-3}$ and the minimization of the noise is the main challenge for the detection of lower density beams. Our typical bunch densities and energies allow us to study space-charge phenomena that can also be scaled to high-energy, high-brilliance beams of interest in the accelerator and high-energy physics community. The backscattering technique is a good alternative to the electrostatic diagnostics used to characterize beams and bunches of energies of the order or greater than a few keV. The main advantages are the non-perturbative nature of this diagnostics and the potential to offer a wealth of information. The analysis of the radiation spectrum can give information on the beam longitudinal energy and energy spread, while the intensity of the scattered radiation is related to the bunch density.

A Thomson backscattering diagnostic apparatus has been implemented in ELTRAP, based on a 5 ns, 1064 nm, Nd:YAG laser pulse interacting with the traveling electron bunch as shown in diagram 2.5. Our aim is the study of bunches in the $10^{8} - 10^{10} cm^{-3}$ range. A previous characterization of the electron bunch showed that space-charge effects are relevant even at the relatively low density of some $10^{8} cm^{-3}$. Obviously, the density puts constraints on the number of photons and thus on the information one can obtain with the Thomson backscattering technique.

The Thomson scattering between a photon and an electron results in a wavelength shift,

$$\lambda_s = \lambda_i \frac{1-\beta\cos\theta}{1+\beta} \qquad 3.1$$

where λ_i and λ_s are the wavelengths of the incident and scattered radiation, respectively, $\beta = v/c$ is the ratio between the electron velocity and the speed of light, and θ is the scattering angle, i.e., the angle between the directions of the incident and scattered radiation. For beam energies of the order of 10–20 keV, the backscattered radiation turns out to be in the visible range, and is detected with a photomultiplier (PMT). An Electron Tubes 9113B PMT with a detection range 300–800 nm is used for the optical collection of scattered photons. In order to

increase the solid angle and to get as close as possible to ideal backscattering conditions, the PMT is positioned as close as possible to the viewport and to the longitudinal axis of the machine. However, the volume occupation of the device limits the minimum distance from the axis to h ≥ 30 mm. In order to reduce the stray light, filters have been placed in front of the PMT according to the expected spectrum of the scattered light. This filter package also limits the solid angle acceptance of the detector, thus reducing the relative contribution of the stray light in the detected signal.

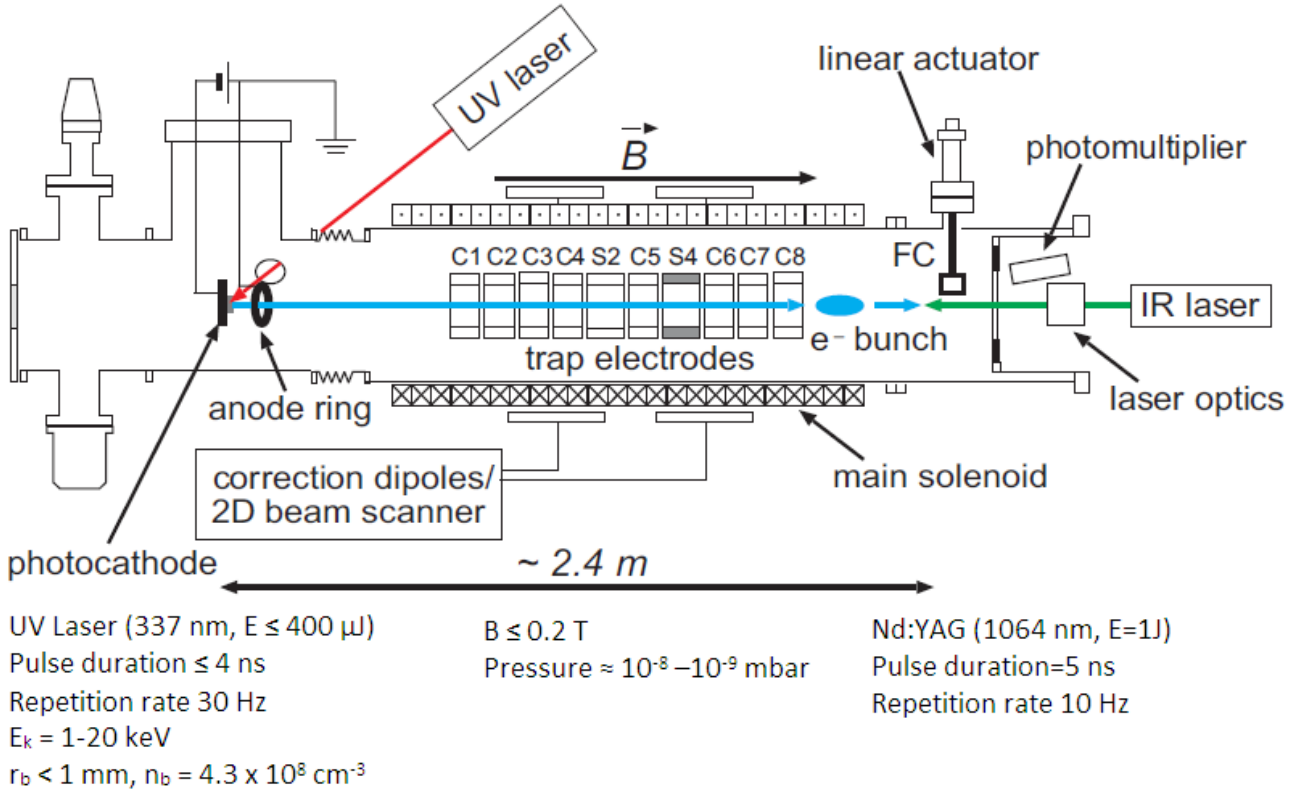

Figure 2.5 Sketch of the Thomson backscattering diagnostic set-up. A pulsed electron bunch is extracted by an UV laser beam impinging on a photocathode set at a potential of 1-20 kV. The bunch is focused by the axial magnetic field B ≤ 0.2 T of the trap. The trap electrode S4 can be used to detect the bunch crossing via induced current. A 2D beam scanner, combined with the charge readout from a Faraday cup, sets the current flowing in two orthogonal sets of dipole coils and deflects the bunch transversally until the bunch transverse position reaches the desired interaction point. The radiation of an IR laser is filtered and focused onto the same interaction point by a suitable optical system. The backscattered radiation is optically filtered and detected by a photomultiplier (PMT).

Indeed, although conceptually simple the realization of the Thomson backscattering experiment presents several complications and limitations. First of all, the main limitations is the relatively low density of the electron beam as well as noise issues which limit the photon detection capabilities. Second, the short duration and the small cross section of both electron bunches and laser pulses (below 1 mm) require an accurate time and space coincidence. Third, the duration of both laser and electron pulses requires a timing with an accuracy ≤ 1 ns. Moreover, the situation is

complicated by the UV laser jitter being of the order of 20 ns. The implementation of a system for the time coincidence, i.e., the simultaneous arrival of the electron and laser bunch in the interaction point, is therefore mandatory. The Faraday cup and the electrostatic signal from the S4 electrode are used for the laser-bunch time coincidence while the beam scanner is used to compensate for small mismatches in the relative transverse position of electron and laser pulses for the space coincidence. With the present setup, the estimated sensitivity of the Thomson diagnostics corresponds to a detectable density beyond the yield of the photocathode source.

Noise sources include the coherent disturbance produced by the IR and UV laser discharges and the noise due to the detection electronics. The electronic noises can be reduced by using suitable low-noise amplifiers for the PMT signal, but the detection capability of the backscattered photons is strongly limited by the stray light due to reflections/reemissions of the laser radiation from the internal structures of the trap. Suitable optical and filtering systems have been introduced to reduce this effect, both for the injection of the IR radiation (reducing both the laser higher harmonics content and the entrance of the flash lamp light), and for the detection of the scattered photons (limiting the bandwidth of the PMT to an interval in the visible range). Of course, the optimization of the noise suppression affects the intensity of the useful signal as well. To reduce the complication of the time coincidence system and additionally to increase the electron bunch density, a new UV laser has been implemented very recently, which features a higher pulse energy and a jitter of about 1 ns [64].

2.6.1 Estimate of the minimum sensitivity

In order to estimate the minimum density detectable with our Thomson backscattering set-up we define the sensitivity as the amplitude of the signal detected by the PMT equivalent to the noise i.e. the signal amplitude which is necessary to obtain a signal-to-noise ratio (S/N) equal to 1. The noise level is experimentally measured for the present set-up configuration and includes the residual stray light of the UV and IR laser beam, the coherent noise produced by the IR and UV laser discharges and the electronic noise. The PMT residual signal after subtracting the coherent noise component for three different averaging times, i.e. 0.1, 1 and 5 s, corresponding to the signals of 1, 10, 50 shots respectively shown in figure 2.6. The maximum computed root-mean-square (RMS) noise level were taken for ten different measurements and the maximum values are 1028 μV averaging on 10 shots and 736 μV averaging on 50 shots for averaging times of 1 and 5 s, respectively. The average is not extended to much more than 50 signals due to relatively long time

drifts in the stray light produced by the IR and UV lasers, which make the averaging-subtracting technique ineffective. To measure the expected time of the scattered light a time-resolved technique was used. The Faraday cup is positioned near to the laser trajectory until a portion of the laser beam hits the ceramic back face of the Faraday cup. The diffused light is acquired by the PMT and occur at a time of ≈ 2 ns before the stray light of the IR laser beam. This means that the scattered radiation signal would be expected to start at 28 ns. Notice that the noise level increases in the second part of the time window, after 30 ns, due to the IR laser reflection and induced fluorescence coming from the inner walls of the vacuum chamber.

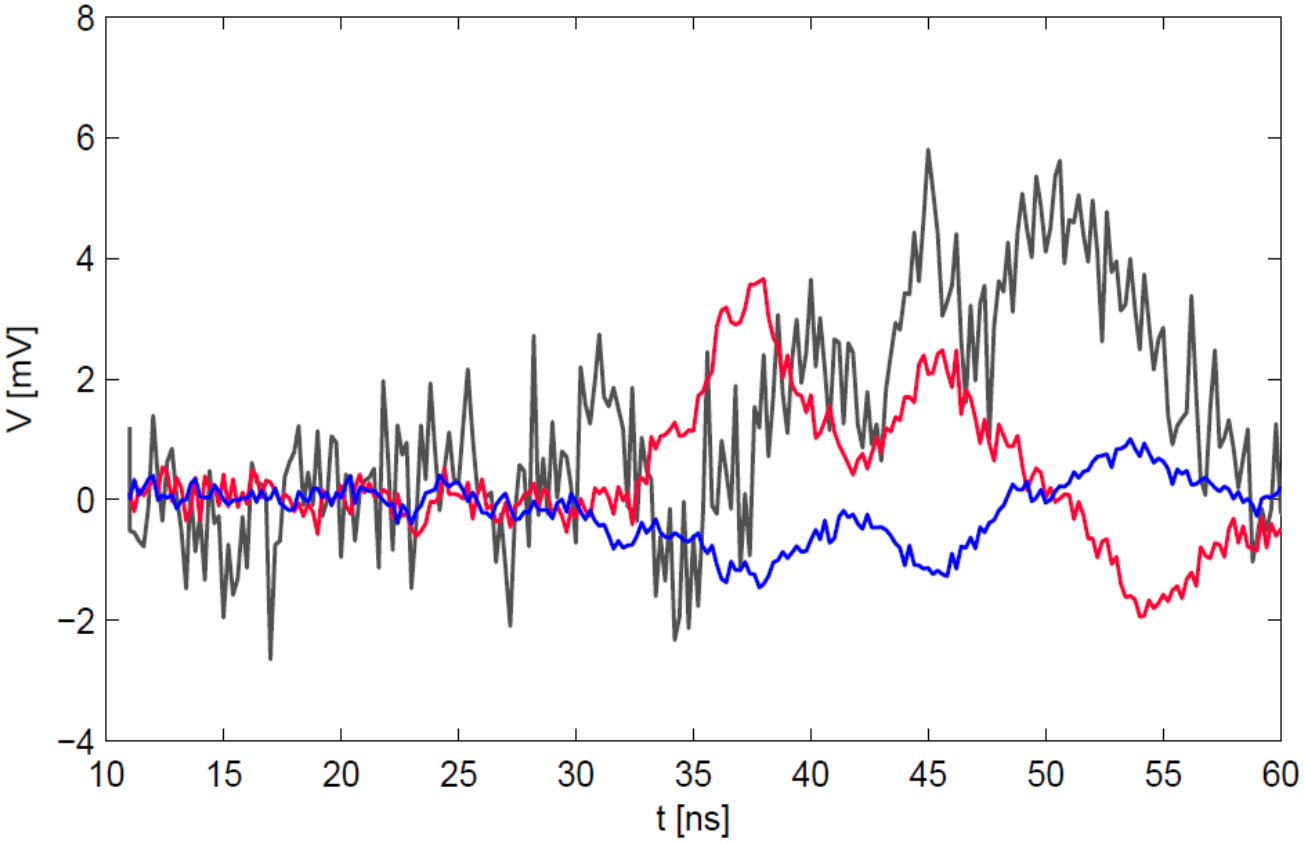

Figure 2.6 Residual background noise measured by PMT after subtracting the coherent noise for averaging times of 0.1 s (gray), 1 s (red) and 5 s (blue), respectively. After t = 30 ns the noise level increases due to the stray light produced by the laser hitting the internal structures of the vacuum chamber.

The identification of the noise source is confirmed by its timing. Considering a bunch-laser interaction starting at 28 ns and lasting for a time of about 5 ns, a portion of the scattered radiation signal will be overlapped with the stray-light signal. The noise level also limits the maximum PMT gain to $G \approx 6 \times 10^4$. Considering these noise levels and assuming a time duration $\Delta t_{\text{int}} = 5ns$ for the bunch-laser interaction, the PMT gain and an impedance load $R_L = 50\Omega$ we

can estimate the signal level as $S = eGR_L N_{phe} / \Delta t_{\text{int}} = 100 \mu V N_{phe}$, where N_{phe} is the number of produced photoelectrons. Considering the condition S/N= 1 we obtain $N_{phe} \approx 10$ averaging on 10 shots for 1 s and $N_{phe} \approx 7$ averaging on 50 shots for 5 s of averaging time. The minimum number of detectable photons is then $N_{ph} = N_{phe} / \eta$. The minimum density can now be estimated computing the integral of the equation:

$$N_p = \int (1 + \beta \cos\alpha) n_p n_e \int_{\Delta\Omega} \frac{d\sigma}{d\Omega} d\Omega \, d^4x \qquad 3.2$$

where $\frac{d\sigma'}{d\Omega'} = \frac{r_0^2}{2}\left(1 + \cos^2\theta'\right)$ is the Thomson differential cross section in the reference frame K' of the electron at rest and $r_0 = \frac{e^2}{mc^2}$ is the classical electron radius, with 'e' the elementary charge, 'm' the electron mass, 'c' the speed of light, and 'θ'' the scattering angle i.e. the angle between the directions of the incident and scattered radiation. Notice that all primed variables are referred to the frame K' and that the four-dimensional integration is performed over the region in space and time of the interaction. The Thomson differential cross section of the electron in the frame K is

$$\frac{d\sigma}{d\Omega} = \frac{r_0^2}{2}\left(1 + \cos^2\theta'\right)\left|\det J\right| \qquad 3.3$$

where 'J' is the Jacobian of the transformation from K' to K:

$$J = \begin{bmatrix} \frac{d\cos\theta'}{d\cos\theta} & \frac{d\phi'}{d\cos\theta} \\ \frac{d\cos\theta'}{d\phi} & \frac{d\phi'}{d\phi} \end{bmatrix} \qquad 3.4$$

Therefore, $N_p = \int (1 + \beta \cos\alpha) n_p n_e \int_{\Delta\Omega} \frac{r_0^2}{2}\left(1 + \cos^2\theta'\right)\left|\det J\right| d\Omega d^4x$ 3.5

where 'n_p' is the photon density of the incident laser and 'n_e' is the electron bunch density. The maximum number of scattered photons occurs at $d_{\text{int}} \approx 10\,cm$ for given a distance between the

PMT and the longitudinal axis h = 30 mm, and a PMT active area $A_{PMT} = 3.8cm^2$ of the PMT. The photon density is computed considering an energy of the incident laser beam of $\approx 0.92\,\eta_L J$ and the geometry of the laser injection optics. The bunch density is estimated for a cylindrical uniform electron charge distribution of radius $r_b \approx 0.3mm$ propagating rigidly with a velocity $V_e = \sqrt{\frac{2E}{m_e}}\,(E = 15keV)$ and for a collinear interaction. The minimum electron density is $n_e = 5.1\times10^{10}\,cm^{-3}$ and $n_e = 3.6\times10^{10}\,cm^{-3}$ averaging on 10 and 50 shots for 1 and 5 s of averaging time, respectively. Therefore, this is the required range of density in order to perform a Thomson backscattering experiment.

In order to make a comparison with the typical electron density in the present experimental set-up, the longitudinal dynamics of the bunch has been investigated as a function of the energy using both destructive and non-destructive methods, i.e. exploiting the aluminum coating of the phosphor screen as a charge collector and measuring the current induced on a sector of the S4 (four insulated sectors) electrode by the bunch crossing. It was thus possible to estimate the length and in turn the longitudinal spreading of the bunch during its transport due to space charge effects. Both methods showed bunch lengths L_b between 10 and 30 cm after transport through the trap for kinetic energies E_k in the 1−15 keV range. The data are consistent with a rigid longitudinal profile $L_b \cong \Delta t_b \sqrt{2E_k / m}$ (for this energy range the non-relativistic formula is consistent with the more accurate relativistic one within a few percent) for energies above 8 keV, while a deviation from the formula towards larger values of L_b is found for lower energies, where we expected indeed space charge effects to become more important.

With a sufficiently high resolution (obtained, e.g., by suitably focusing the IR laser beam), information on the bunch density profile could also be accessible .The optimization in the injection of the high power IR laser and in the collection of the scattered radiation are fundamental issues in achieving the maximum spatial resolution and maximum sensitivity. The maximum sensitivity is achieved when the focal point is 10 cm after the viewport. We can characterize the spatial resolution defining the scattering length $L_s \approx \frac{2r_b}{r_{Lv}.d_{\text{int}}}$, where r_{Lv} is the laser spot radius on the viewport. As L_s increases moving the focal point away from the viewport, the spatial resolution

decreases. In this configuration L_s is about 10 mm. This an acceptable value when compared to typical bunch lengths of 10−30 cm.

Using the transversal and longitudinal properties evaluated here we can estimate the bunch density in the high magnetic field region as $n = \frac{Q}{\pi r_b^2 L_b}$, where Q is the bunch charge. Notice that the laser is focused in order to increase the interaction probability. Hence, only the charge of the inner, Gaussian part of the bunch will interact with the focused IR laser, therefore only this fraction of the total charge should be taken into account. For a set energy of 15 keV and a magnetic field of 0.01 tesla we get $Q \cong 6\,pC$ and $L_b = 29\,cm$, hence a density of about $n_b = 4.3\times10^8\,cm^{-3}$. Thus, densities up to some $10^8\,cm^{-3}$ in the high magnetic field region indicate that the electron bunch is not detectable with the present set-up configuration. In figure 2.7 the reported expected signal for a density $n_b = 3.6\times10^{11}\,cm^{-3}$, i.e. ten times the value corresponding to S/N = 1, assuming a Gaussian profile for the detected pulse with FWHM = 5 ns and averaging on 50 shots.

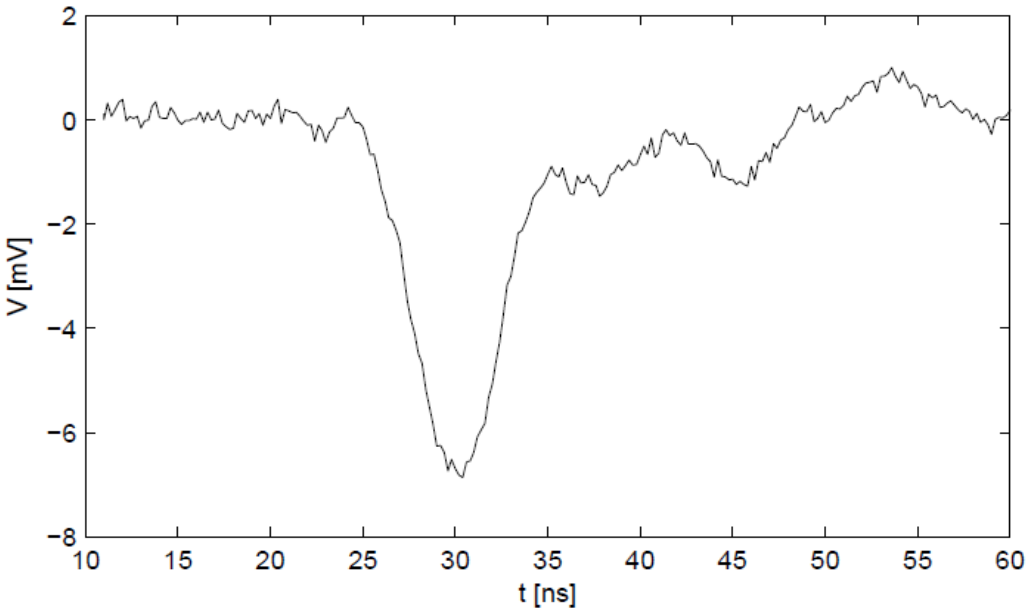

Figure 2.7 Expected scattered photons signal for a bunch of density $\approx 3.6\times10^{11}\,cm^{-3}$ and radius $r_b = 0.3mm$ in the present set-up configuration. We assume a Gaussian signal profile with a FWHM of 5 ns. Part of the signal is overlapped with the stray light noise (see also Fig. 2.6).

2.7 Improvements of the S/N ratio

Further progresses are needed to increase the sensitivity of the diagnostics. In regard to noise reduction, the main noise component is given by the IR laser reflections/re-emissions from the vacuum chamber surfaces to photomultiplier (PMT). An option to reduce this source of stray light would be a weaker focusing of the IR laser, which would possibly prevent part of the reflections on the chamber walls by better laser dumping at the other extremity of the machine. Of course, the optimization of the noise suppression affects the intensity of the useful signal as well. This weaker focusing could be possible by extending longitudinally the machine on the IR laser side in such a way that the injection viewport were more distant from the interaction point. On the other hand, the maximum number of detected photons is expected for an interaction distance from the photomultiplier of about 10 cm. By increasing the distance d_{int} the solid angle spanned by the photomultiplier would be decreased by a factor $1/d_{\mathrm{int}}^{2}$. This disadvantage could be avoided inserting a viewport for the PMT at $d_{\mathrm{int}} = 10\,cm$ in the 'extended' set-up. Yet, although this solution is technically possible, due to the weaker focusing the scattering length would linearly increase, i.e. the longitudinal spatial resolution would decrease with $1/d_{\mathrm{int}}^{2}$, furthermore affecting the energy resolution.

To limit the reflections from the inner surfaces of the vacuum chamber and of the internal electrodes to reach the PMT, a suitable light shield has been designed. This shield consists of a disc with a 20 mm hole mounted on the trap stack holding bar. The hole allows the IR beam propagation up to the laser-bunch interaction point, but its backside, structured with deep grooves, prevents most of the light reflected by the chamber walls to reach the PMT. It is also to be noted that the reduction of the overall noise level would yield the further advantage of increasing the (presently limited) gain of the PMT, and therefore the signal level. An improvement in the dynamic range can also be obtained by replacing our PMT with a different one featuring a better quantum efficiency in the expected wavelength range of the backscattered radiation. PMTs with quantum efficiencies above 10% in the visible range are commercially available.

In order to increase the electron density and in turn the detectable signal we will evaluate both source modifications and a replacement. The present source was installed as a test one, having in mind its possible intrinsic limitations (namely, particle density). Yet the compactness and ease of

use of such a small source has been very handy in the characterization of the beam by electrostatic means and in the validation of the space and time coincidence systems. Furthermore with this source we have already observed the generation of a much larger charge (easily above 1 nC) when the focusing of the UV laser on the photocathode is increased, but the charge is not well extracted. A better extraction geometry will be also evaluated for future experiments. As an alternative, quasi-continuous or pulsed electron sources reaching densities up to $10^{11}cm^{-3}$ are already available.

Finally we consider that this diagnostics can be extended at higher energies (some hundreds of keV), where the Thomson backscattering becomes more efficient and the scattered radiation is detected with higher quantum efficiency. Furthermore, light reflected by walls is not Doppler shifted, and is then more easily filtered out. A similar apparatus is under development as a non-destructive diagnostics of low energy electron beams in cooling devices [73].

2.8 Conclusions and outlook

In addition to the diagnostics for bunched electron beams, new diagnostic and/or control systems for confined electron plasmas are being developed in ELTRAP. Recently, it has been shown [25] that an electron plasma can be generated by means of a low-voltage (≤ 10 V peak-to-peak) RF drive in the 1–20 MHz range applied on an azimuthally sectored electrode of the trap under UHV conditions as discussed in chapter 3. A prototype microwave waveguide transmission has been designed and bench tested (see chapter 4). The electrostatic and electromagnetic simulation of RF heating and ionization process of electron plasma under ultra-high vacuum conditions has been analyzed also by means of a two-dimensional (2D) particle-in-cell (PIC) code (discussed in chapter 5).

Chapter THREE

Wave-particle interactions in non-neutral plasmas

3.1 Introduction

An electron plasma has been generated in ELTRAP without the use of a specific electron source (e.g., a thermo-cathode), by means of the application of low power (≤10 V peak-to-peak) radio frequency (RF) drives in the 0.1-20 MHz range on an azimuthally sectored electrode of the trap under ultra-high vacuum (UHV) conditions [B. Paroli, F. De Luca, G. Maero, F. Pozzoli, and M. Romé, Plasma Sources Sci. Technol. 19, 045013 (2010)]. The generation and heating of the electron plasma will be repeated in the future with a RF injection system up to a few GHz, for which microwave waveguide transmission has been designed and tested (see chapter 4). The new RF system will open up the possibility to study, e.g., the interaction between the confined plasma and traveling electron bunches.

3.2 RF electron plasma generation in a Penning–Malmberg trap

In order to generate an electron plasma, the few electrons initially present in a Penning trap must reach a sufficiently high energy in order to ionize the residual gas in the vacuum vessel. In other words, the electrons must have a kinetic energy larger than the first ionization energies of the residual neutral components, i.e. mainly H_2 or other light atmospheric gases. For these gases the energy threshold is between 10 and 20 eV and the peak of the ionization cross section approximately lies in the 70–100 eV range. Therefore, the electrons must reach an energy of some tens of eV to build up and sustain a plasma. That's why it is very important to know the heating mechanism by which electrons can gain energy in a Penning trap. The major heating mechanisms are collision-less or stochastic plasma heating by electrostatic waves, and electron cyclotron resonance heating (ECRH).

3.2.1 Stochastic heating

In non-neutral plasmas under ultra-high vacuum condition the electron mean free path is large enough for the electrons to be essentially collisionless. Let us remind that stable UHV conditions are obtained in ELTRAP with the use of a pre-vacuum scroll, a turbo molecular and an ion pump, reaching pressure values in the low 10^{-9} mbar, and that the electrode stack consists of ten OFHC cylinders each having a length and diameter of 9 cm except electrodes S2 and S4, azimuthally sectored into two and four patches, respectively, having a length of 15 cm. Potentials in the interval (-100 V - 100 V) can be applied on each cylinder by means of two 8-channel waveform generators (see diagram 3.1).

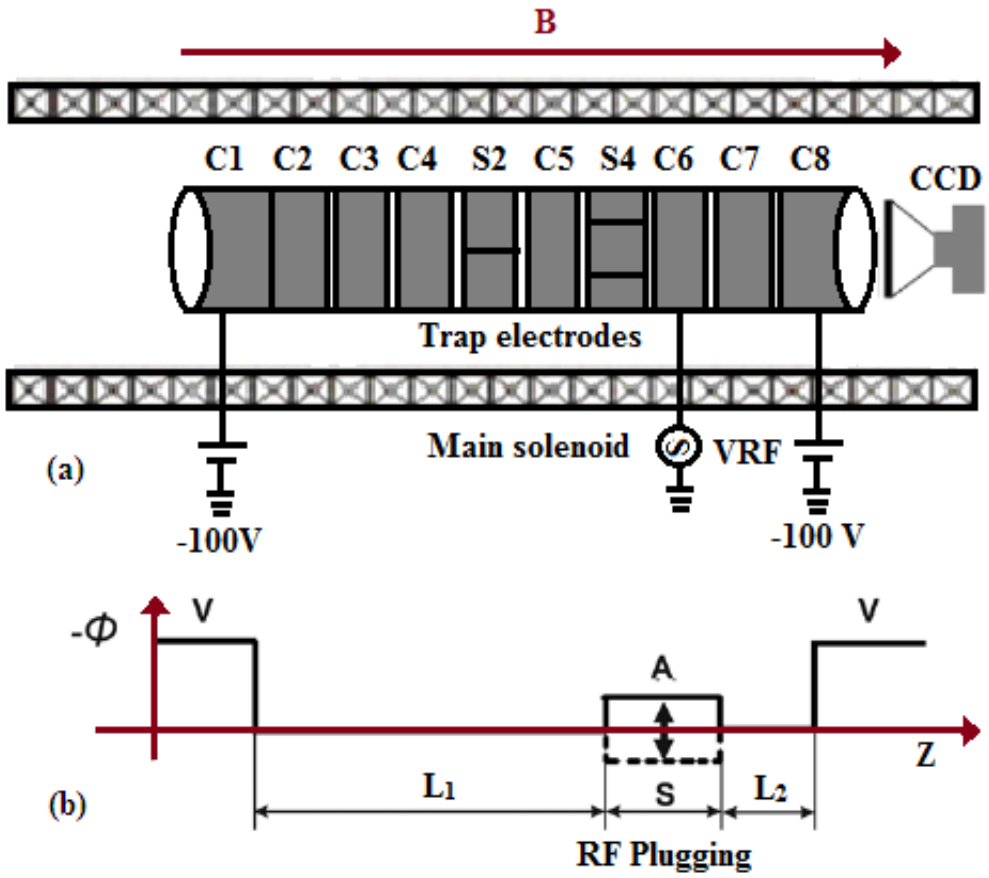

Figure 3.1 Sketch (a) of the ELTRAP set-up as used for RF discharge and plasma confinement experiments, with a CCD camera for optical diagnostics. Sketch (b): indicative scheme of the electrode potentials, with confinement between electrodes C1 and C8 biased at a negative voltage V and RF drive of amplitude 'A' on electrode C6.

The RF power for plasma generation and heating is given by a power supply capable of producing sinusoidal waveforms of amplitude ≤ 10 V and frequencies up to 80 MHz. The RF signal of the

power supply is directly imposed on a trap electrode suitably chosen as antenna through a 50 Ω impedance coaxial cable without any matching network. The power absorbed is of a few hundreds mW. A fraction of the electrons present in the trap can gain an energy of the order of a few tens eV. The ionization which results from energetic electron's impact with the background gas is increasing with the continuous application of the RF signal. The electrons produced by the ionization of the residual gas promote the self-sustainment of the discharge necessary to obtain appreciable charge densities. In the experiments, these electrons were confined radially by a static homogeneous magnetic field of 0.1 T and axially between electrodes C1 and C8 with an applied voltage of -100 V.

Experimentally, a quantitatively measurable plasma formation has been evidenced after ≈ 300 ms with the optical diagnostics. The plasma evolution over the first few hundred ms was recorded, for a RF amplitude of 3.8 V and a frequency of 8 MHZ applied to the C7 cylinder. After the selected excitation time the trapping potential of end cylinder C8 was lowered and the confined plasma was discharged/dumped onto a P43 three-layer aluminum-coated phosphor screen.

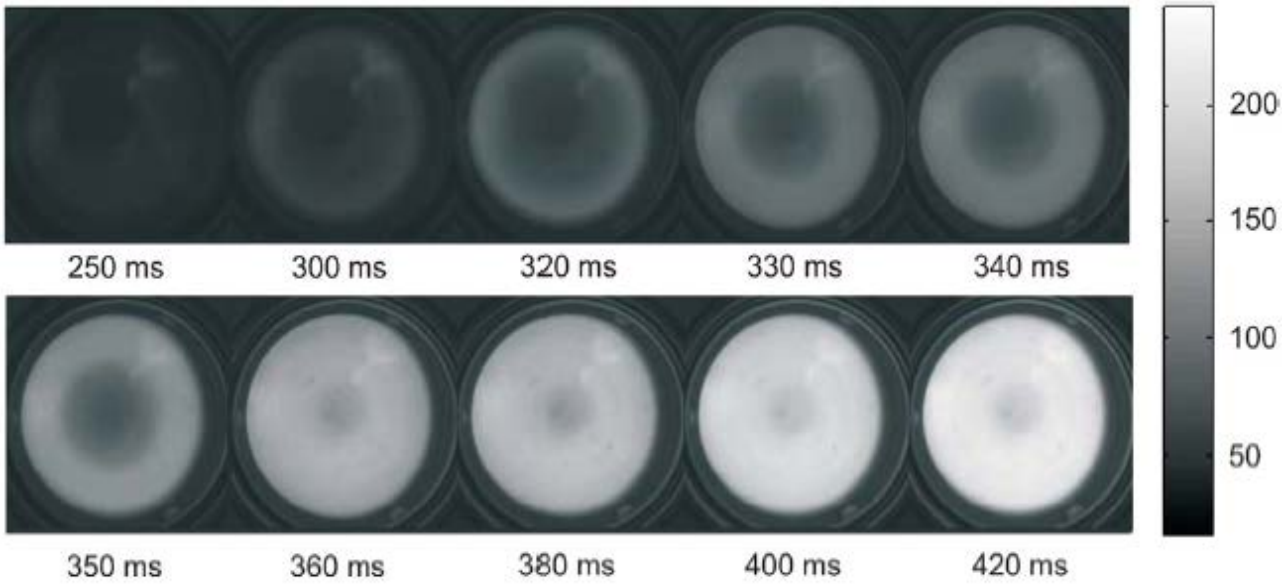

Figure 3.2. Optical measurement of the transverse density profile during the discharge. The plasma can be observed after ≈ 300 ms. The generation takes place initially mostly in the periphery and successively extends to the whole space.

The intensity of the light image emitted by the phosphor and detected by a charge-coupled device (CCD) camera with a resolution of 1344 × 1023 pixels and typical readout noise of ten electrons is proportional to the axially-integrated electron density n(r, θ). The plate is biased at ≈15 kV and has

a diameter of 11 cm, so that the whole plasma is collected on it and the energy is sufficient to produce an axially integrated image of the confined plasma. The screen can also be used without high voltage bias as a charge collector to yield the value of the total trapped charge. The charge density images obtained with RF excitations from 250 to 420 ms shown in figure 3.2 indicate that the plasma is produced mainly close to the trap wall and as time progresses it fills the central region of the trap. These observations are also confirmed by the radial profiles (a vertical cut passing through the symmetry center) of the distributions (see Figure 3.3 left). Integrating azimuthally the profiles, normalized to the total charge (see Figure 3.3 right) we obtain a grouping in three different shapes: (a) for 300−320 ms, (b) for 330−350 ms, (c) for 360−420 ms. This suggests the presence of complicated collective phenomena beyond a basic, continuous diffusion process.

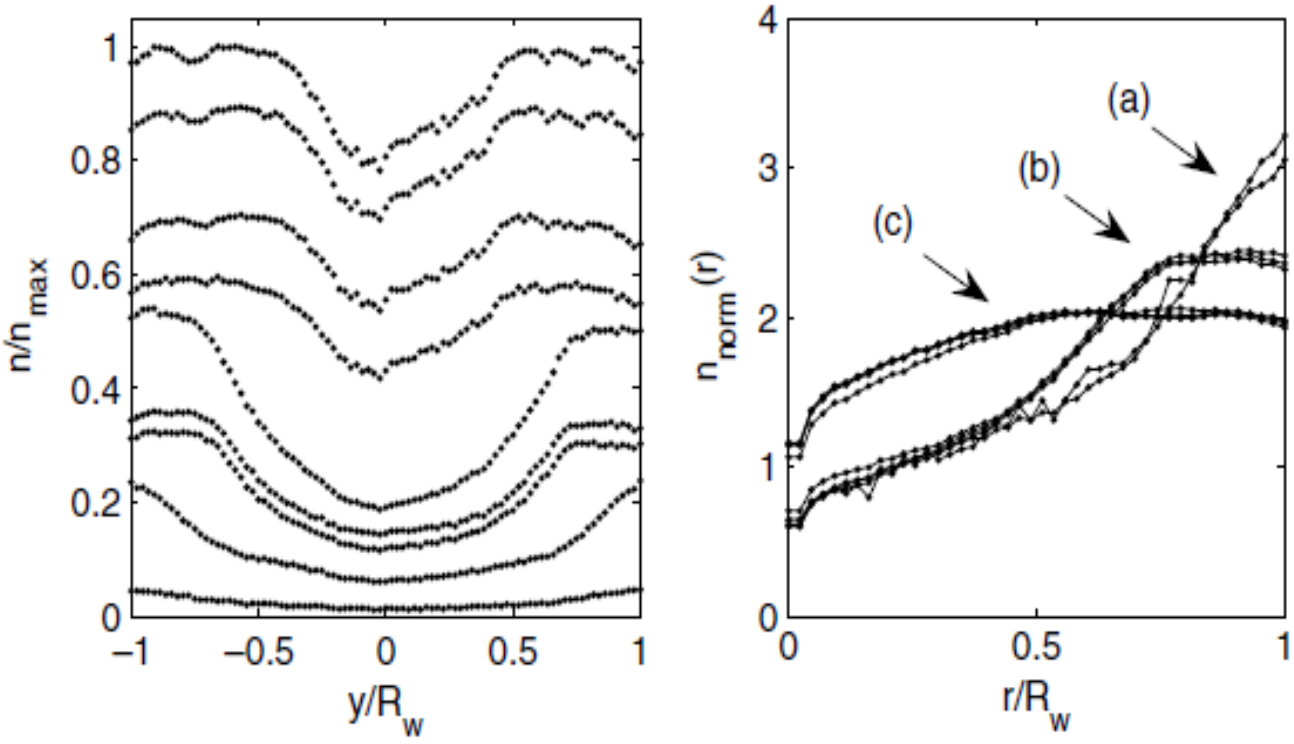

Figure 3.3: Axially-integrated density profiles during plasma formation, for times between 300 and 420 ms. On the left, profiles along the vertical axis y, normalized to the maximum measured value. On the right, azimuthally-integrated profiles, normalized to the total charge. The profile evolution is not continuous but follows three successive shape groups: (a) for 300−320 ms, (b) for 330−350 ms, (c) for 360−420 ms.

It is found experimentally that the amount of charge is influenced by the RF parameters as well as by the geometry of the trap. The plasma was generated by a continuous RF drive of amplitude 3.8 V under different conditions, namely the length of the trapping region, the cylinder used as

excitation antennas and the RF excitation frequencies ranging in the interval 0.1-20 MHz with a resolution of 100 kHz. The experimental results are shown in figure 3.4. In the first case the trapping region was between the electrode C1 and C8 (long trap) while in the second case was between S2 and C8 (short trap). For both configurations different electrodes (cylinders) were used for the RF application. For each frequency value, the excitation has been applied for 4.5 s in each geometry, after which the trapping voltage on the C8 electrode has been lowered and the plasma dumped on the phosphor screen, used as charge collector.

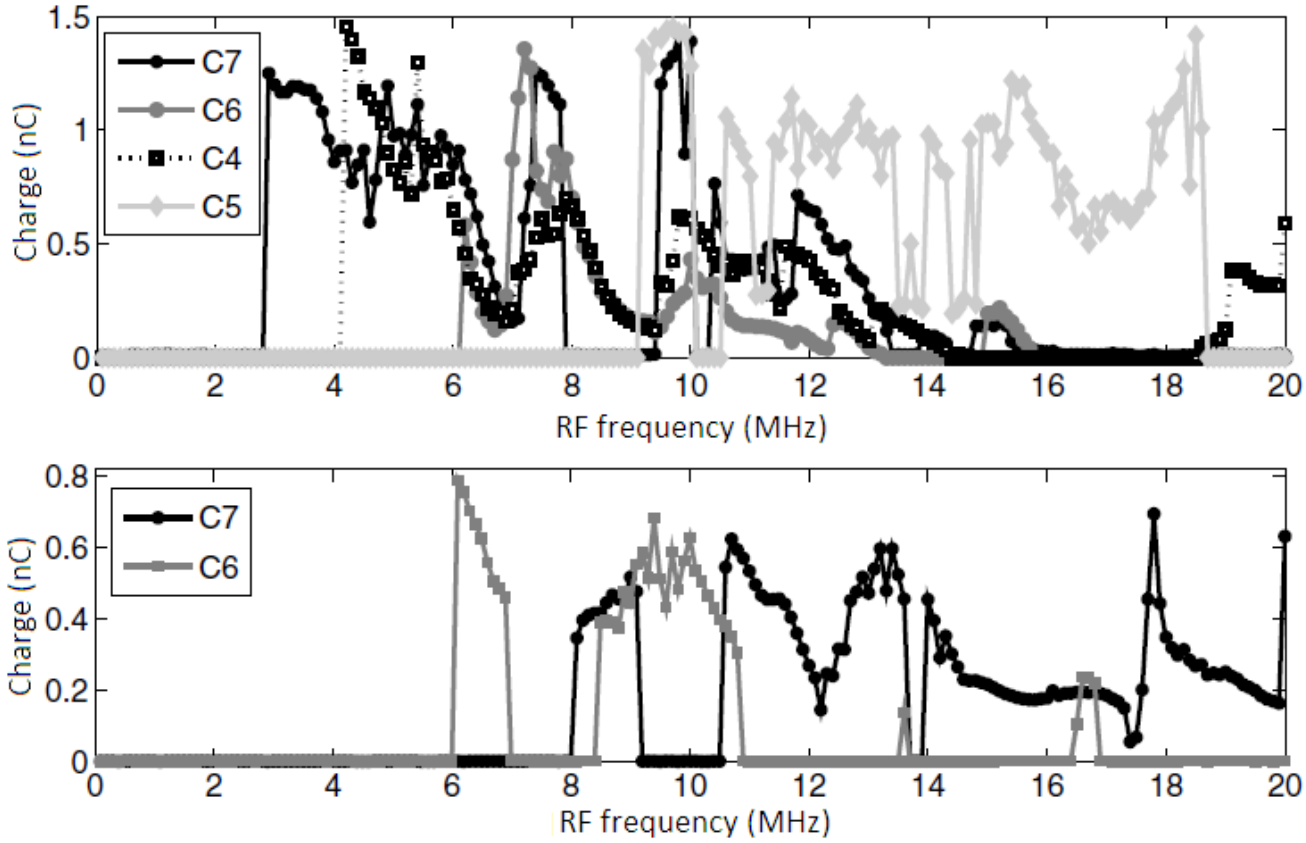

Figure 3.4. Total charge confined after 4.5 s. The plasma is formed and confined between C1 and C8 (top, long trap) or between S2 and C8 (bottom, short trap). The legend specifies the electrode used as antenna for the RF excitation.

The discharge signal has been filtered from the random noise (typically ≤ 90 mV rms) with a digital low-pass filter of the third order with cutoff frequency 500 kHz. The collected charge is then calculated as $Q = -V_{\min} C$. Here V_{min} is the minimum of the voltage discharge signal and C the capacity of the measurement system, i.e. essentially the capacity of the coaxial cable. The latter is obtained directly from the time constant 1/RC of the discharge, with a resistance R = 1 MΩ given essentially by the load of the oscilloscope. The phenomena appear to be non-resonant because a noticeable amount of plasma formation is detected beyond a certain threshold frequency, which

changes with the geometrical parameters, and occurs in broad frequency bands rather than resonance peaks. For each choice of the geometry and excitation antenna a threshold frequency exists under which no plasma is formed. Beyond this frequency, appreciable amounts of charge are created within wide frequency bands, whose upper cutoff is generally not as abrupt as the lower one. The total charge obtained in the short trap configuration is about half of that obtained with the long trap and no detectable plasma production has been observed with even shorter trapping lengths as shown in figure 3.4.

In both geometries, the total charge is of the order of 1 nC corresponding to a density of ≈ 10^6 cm^{-3} that is comparable to the densities obtained with the thermo-cathode sources used in past experiments [31, 32] as well as in similar set-ups [33]. The results are qualitatively in agreement with the one-dimensional model (electron–oscillating barrier interaction model) described below in that the lowermost threshold for plasma creation is obtained using the C7 electrode as RF antenna, while higher frequencies are needed with electrodes closer to the center of the trap. When the confinement length is reduced this argument is apparently no longer valid and in general the creation of the plasma is more difficult.

The density growth at the trap wall is compared with a theoretical estimate of the ionization rate according to the law

$$\frac{dn(t)}{dt} = N_n \langle \sigma(v) v \rangle n(t) \qquad 3.5$$

where we consider only the first ionization cross-section. At the working pressure of $P \approx 4 \times 10^{-9} mbar$ and at room temperature the neutral density of the residual gas is $N_n = \frac{P}{k_B T} = 9.7 \times 10^{13} m^{-3}$ (assuming that in the UHV conditions only molecular hydrogen is present), $n(t) \approx 10^{12} m^{-3}$ is electron density, $\sigma(v) = 1 \times 10^{-20} m^2$ is the electron-impact ionization cross section for H_2 [29] at the electron velocity $\overline{v} = \sqrt{\frac{2KT}{m_e}} \approx 5 \times 10^6 m/s$ corresponding to kT = 80 eV, i.e. the maximum energy of the particles confined in the trap. Using the above data $N_n \langle \sigma(v) v \rangle \equiv \frac{1}{\tau} = 3.3 s^{-1}$. Figure 3.5 shows the experimental densities at the trap wall, normalized to the maximum measured value, grouped consistently with the three groups found before i.e. (a)

for 300–320 ms, (b) for 330–350 ms, (c) for 360–420 ms. Partial fits yield $\frac{1}{\tau} = 81.3s^{-1}, 25.25s^{-1} and\ 9.9s^{-1}$ for groups (a), (b) and (c), respectively. In every case the experimental ionization appears much higher than expected. Likely, secondary production mechanisms play a dominant role in the plasma density growth.

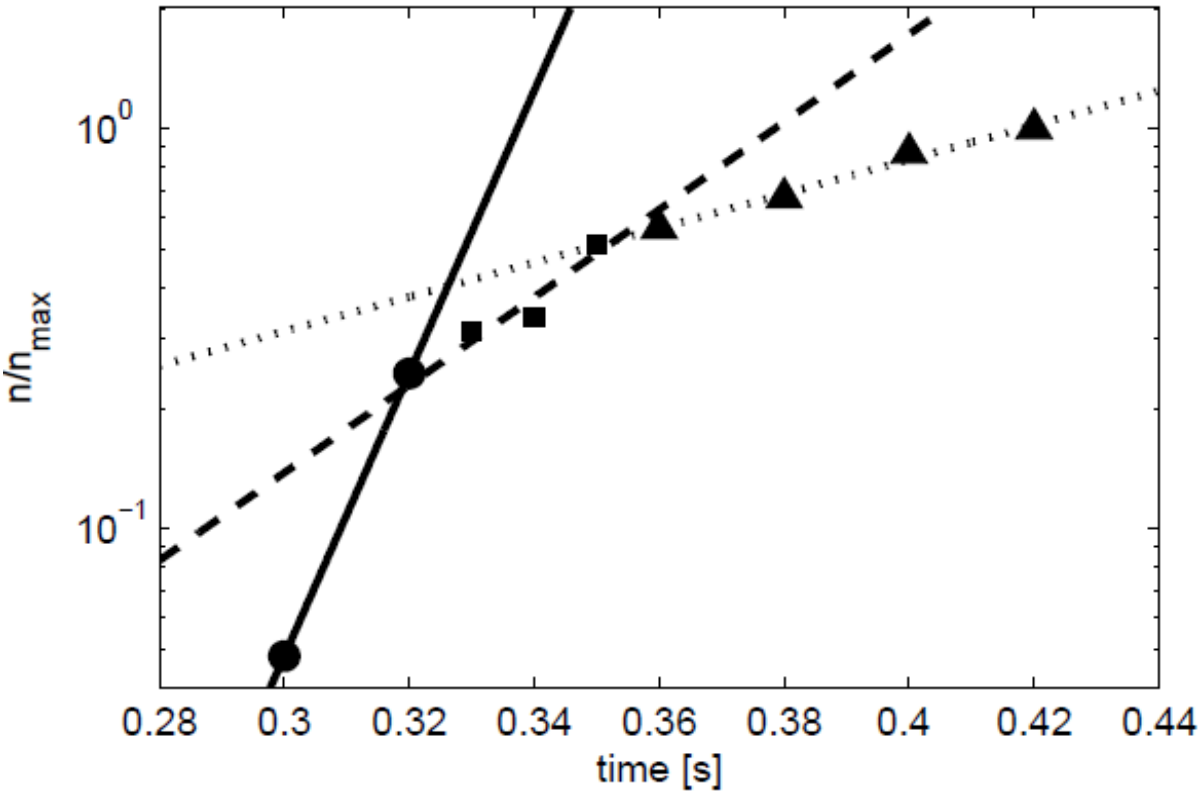

Figure 3.5: Ionization rate measured in terms of density growth at the trap wall, normalized to the maximum measured value. The data are grouped according to figure 3.3 (circles correspond to group (a), squares to (b) and triangles to (c)) and are fitted with exponential laws of inverse time constants 81.3, 25.2 and 9.9 s^{-1}, respectively.

3.2.2 Electron heating by a Fermi acceleration mechanism

A Fermi-like one-dimensional model is able to explain at least qualitatively that electrons can be heated beyond the energy threshold of the first ionization cross section for light gases (≈ 10–20 eV) with a low-power RF drive such as that used in the experiments. The model is sketched in Fig. 3.1 (bottom). An electron of charge −e and mass m is confined in a square potential well of depth V and interacts with a square barrier of amplitude $A\sin(\omega t)$, where ω is the frequency of the sinusoidal oscillation. When the electron interacts with the edges of the barrier its energy changes instantaneously of a quantity $\tilde{E} = E_i - eA\sin(\omega t)$. This variation occurs only when the electron

energy exceeds the amplitude of the barrier otherwise the electron is reflected. Taking into account many interactions, the electron energy state 'E_i' at the interaction 'i' is written in term of an iterative map:

$$\begin{cases} \tilde{E} = E_i + (-1)^{k_i} eA\sin\left[\omega\left(\sum_{j=0}^{i}\frac{l_{kj}}{\sqrt{\frac{2E_j}{m}}}\right)+\phi\right] \\ E_{i+1} = \tilde{E} \quad \text{if} \quad \tilde{\mathrm{E}} > 0 \\ \mathrm{E}_{i+1} = E_i \quad \text{if} \quad \tilde{\mathrm{E}} < 0 \end{cases} \qquad 3.6$$

where $l_k = (2L_1, S, 2L_2, S)$ is a vector indicating the lengths of the regions that the particle would go through over a complete bounce period without being reflected at the oscillating barriers. The region S has been replicated for a practical reason, namely that if no reflection takes place $(\tilde{E} > 0)$, the sequence of the indexes k = (0, 1, 2, 3), i.e. the sequence of regions travelled by the particle, is repeated always in the same order. On the contrary, every time that the particle is reflected by an oscillating barrier $(\tilde{E} < 0)$, it crosses again the last region and the order of the sequence k is inverted. For the implementation of the numerical algorithm, a flag σ is introduced that changes sign when a particle reflection occurs, i.e.

$$\sigma_{i+1} = \sigma_i \ \text{ for } \tilde{\mathrm{E}} > 0,\ \sigma_{i+1} = -\sigma_i \ \text{ for } \tilde{\mathrm{E}} < 0 \ \text{ and } \sigma_0 = 1$$

The iteration rules for k_i will then be:

$$\begin{aligned} &\bullet \ \text{If } \tilde{\mathrm{E}} > 0 \text{ and } \sigma_{\mathrm{i}} > 0 \rightarrow k_{i+1} = \mathrm{mod}(k_i + 1, 3), \\ &\bullet \ \text{If } \tilde{\mathrm{E}} > 0 \text{ and } \sigma_{\mathrm{i}} < 0 \rightarrow k_{i+1} = \mathrm{mod}(k_i - 1, 3), \\ &\bullet \ \text{If } \tilde{\mathrm{E}} < 0 \rightarrow k_{i+1} = k_i \end{aligned} \qquad 3.7$$

The equation 3.6 can be solved recursively changing the amplitude A and for different values of ω. For a number of interactions of the order of 10^7–10^8, corresponding to a few seconds, the energy distribution f (E), i.e. the count of energy values 'E_i' recorded at the interaction instants 'i', tends to a limit that is independent of the initial phase ø of the RF drive. Figure 3.6 shows the distribution function f (E) varying the amplitude and the frequency of the RF drive and for a geometry corresponding to a potential well between the electrodes C1 and C8 and with the RF applied on C7. An appreciable number of electrons exceeds an energy of 10 eV for RF amplitude greater than 1.8 V (for a drive frequency of 1 MHz), while for an amplitude of 3.8 V the electron energies are distributed to higher values increasing the drive frequency between 1 to 8 MHz. In both cases with a maximum RF amplitude of 3.8 V the electrons reach values exceeding the first ionization energy

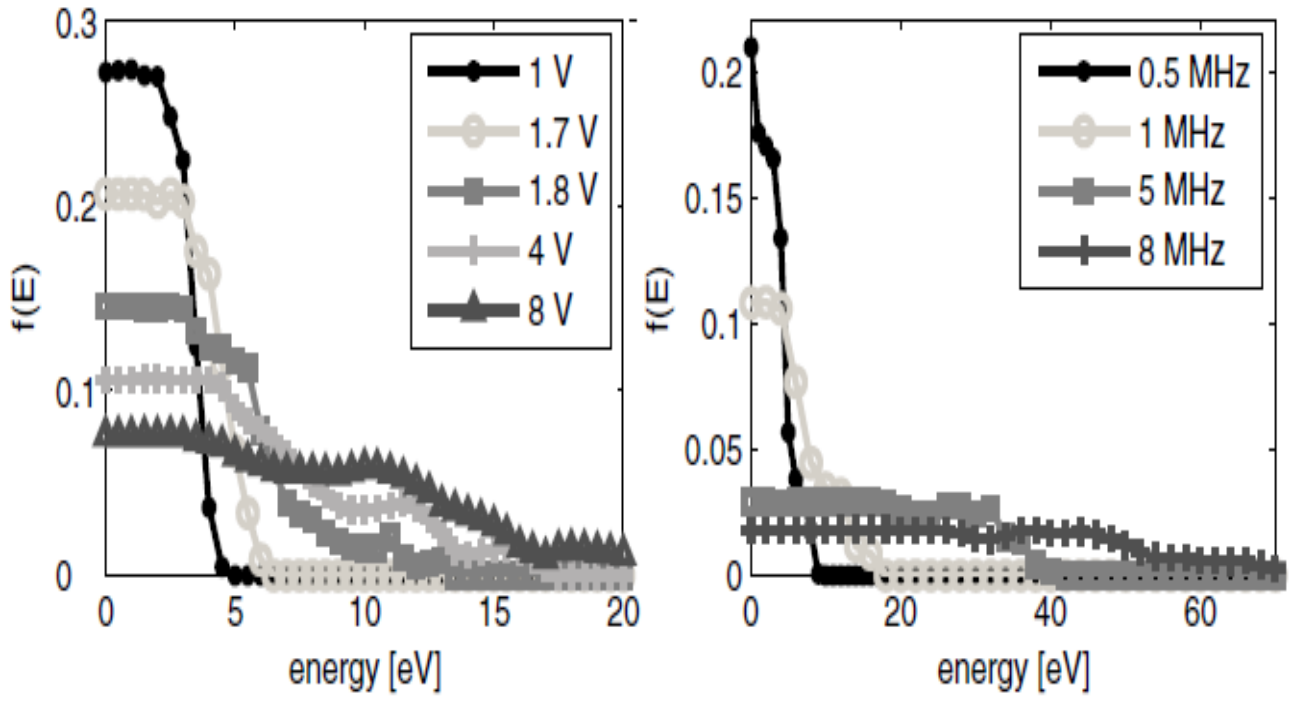

Figure 3.6: Limit energy distributions f(E) of a trapped electron, after 10^7 interactions with an oscillating barrier. Geometrical parameters of the ELTRAP device have been used: confinement between electrodes C1 and C8, RF drive on electrode C7. In the left panel, the amplitude of RF drive is varied while keeping the frequency at 1 MHz. In the right panel, the frequency is varied at a constant amplitude of 3.8 V.

of the residual gas (molecular hydrogen). This model is of course a strong simplification of the real system because the electron motion is forced to be one-dimensional, the electrons formed in the trap are non-interacting and the potential square well is an ideal case.

A plasma density $n \approx 10^{-6} cm^{-3}$ achieved by means of the stochastic heating/ionization mechanism is not suitable to promote a strong beam-plasma interaction. However, plasma compression induced by the same RF used for the electron heating can increase the plasma density of some orders of magnitude.

The heating mechanism has been analyzed also by means of a two-dimensional (2D) particle-in-cell (PIC) code (discussed in chapter 5). In the simulations, a realistic geometry of the apparatus is used, with a length of the electrode stack of 102 cm, and an internal radius of the conducting cylinders of 4.5 cm. The simulation studies confirm that initially the heating is higher near the wall of the cylinder and then extends to the whole space. Thus, it is confirmed that the RF heating is more effective in the outer radial part of the trap cylinder and electrons localized near to wall of the cylinders reach energies ≥ 20 eV, and are able to ionize the residual gas better than the electrons located close to the central part of the trap. A Monte-Carlo scheme is also applied in the PIC simulation to evaluate the ionization for different pressure values i.e. $P = 10^{-8} torr$, $P = 10^{-7} torr$ and $\mathrm{P} = 10^{-6}\ torr$ for different electron densities $5 \times 10^{7}\ m^{-3} and\ 10^{12}\ m^{-3}$, using hydrogen as a background gas.

Chapter FOUR

Waveguide design and microwave injection bench test

4.1 Waveguides

Waveguides are basically a device for transporting electromagnetic energy from one region to another. Typically, waveguides are hollow metal tubes constructed from conductive material of various types and different sections such as rectangular, circular, truncated or elliptical. Our aim is to use an RF generator (with a frequency up to 3 GHz) in order to inject microwaves into the ELTRAP device. The microwaves will heat plasma electrons, which in turn will collide with the atoms or molecules of the residual gas in the trap, causing ionization and allowing one to obtain an electron plasma with a higher density and temperature.

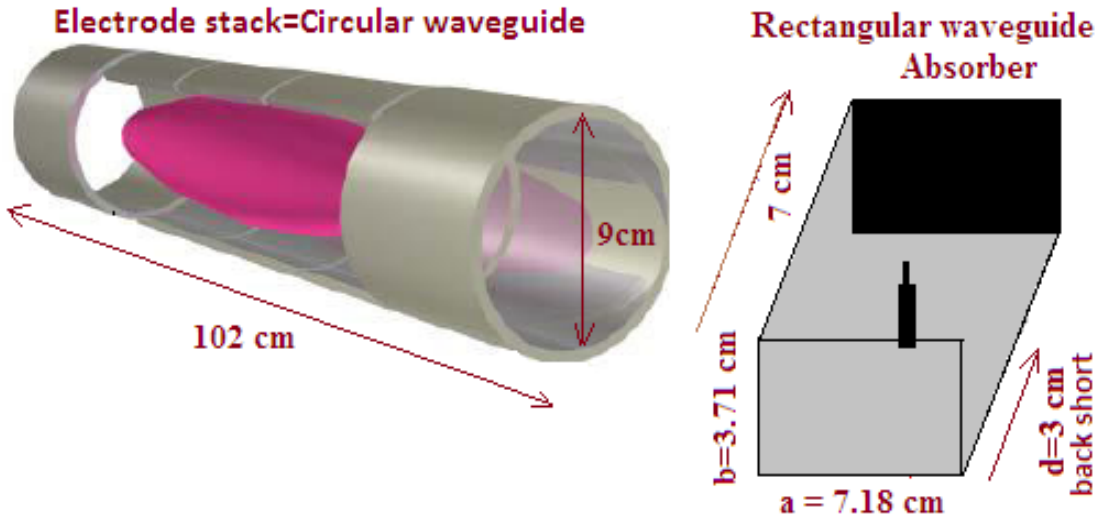

Figure 4.1 Sketch of a rectangular waveguide with dimensions a = 7.18 cm, b = 3.71 cm and length 7 cm with a coupling rod, and of a circular waveguide with a 9 cm diameter and 102 cm length.

The discussion is limited to rectangular and circular waveguides. The wave will propagate under ultra-high vacuum conditions, guided by the walls of the waveguide and that implies certain conditions that must be met. The boundary conditions for waveguides are:

1. The electric field must be orthogonal to the conductor surface.
2. The magnetic field must not be orthogonal to the surface of the waveguide.

The boundary conditions that apply to waveguides will not allow a TEM wave to propagate in these single conductor transmission lines because both the electric and magnetic field components would be transverse to the direction of propagation. Only higher modes in the form of transverse electric TEmn and transverse magnetic TMmn modes can propagate in the waveguide. The two subscripts (m, n) are integers that indicate the number of half-period variations in transverse field intensity along the 'a' and 'b' dimensions of the guide, respectively.

The waveguide acts as a high pass filter and each mode has a cut off frequency (fc) below which the mode is attenuated and has no propagation in the waveguide. The lowest excited mode in the waveguide is called the dominant mode. The cut off frequencies for rectangular waveguides are written as

$$\left(f_c\right)_{mn}^{TE} = \frac{1}{2\sqrt{\mu\,\varepsilon}}\sqrt{\left(\frac{m}{a}\right)^2 + \left(\frac{n}{b}\right)^2}\,(Hz) \qquad 4.1$$

where a, b are the width and the height of the waveguide, and μ and ε are the permeability and permittivity of material inside of the waveguide, respectively. Rectangular waveguides support only transverse electric TEmn modes, while a circular waveguide is capable to support both transverse electric (TEmn) and transverse magnetic (TMmn) modes. The cut off frequencies of the TE and TM modes are given by

$$\left(f_c\right)_{mn}^{TE} = \frac{C \times \chi'_{mn}}{2\pi\ \mathrm{r}}\,(\mathrm{Hz}) \text{ and } \left(f_c\right)_{mn}^{TM} = \frac{C \times \chi_{mn}}{2\pi\ \mathrm{r}}\,(\mathrm{Hz}) \qquad 4.2$$

where 'C' is the speed of light in vacuum and 'r' is the radius of the circular waveguide. The constants χ'_{mn} *and* χ_{mn} are reported in table 4.1 and 4.2, respectively, and represent the nth zeroes (n=1, 2, 3…..) of the derivative of the Bessel function Jm of the first kind of order m (m=0, 1, 2, 3…..).

The major issues to be addressed in waveguide propagation are attenuations and excitation of desired mode. The attenuations are determined by dielectric and conductor losses. Therefore, the dielectric used inside waveguides is usually air, which has a lower loss with respect to other insulating materials. Of course, this kind of loss becomes negligible under ultra-high vacuum conditions, while the loss determined by the conductor wall can be suppressed by using a metal tube made of a high conductive material. Furthermore, the attenuation may be improved by plating to reduce skin effect losses. Beside the attenuation problem another issue that requires attention is the excitation method (explained in section 4.3).

Table 4.1 TE (modes) zeroes χ'_{mn} of derivative $J'_m(\chi'_{mn}) = 0 (n = 1,2,3,....)$ of Bessel function $J_m(x)$

	$m=0$	$m=1$	$m=2$	$m=3$	$m=4$	$m=5$	$m=6$	$m=7$	$m=8$	$m=9$
$n=1$	3.8318	1.8412	3.0542	4.2012	5.3175	6.4155	7.5013	8.5777	9.6474	10.7114
$n=2$	7.0156	5.3315	6.7062	8.0153	9.2824	10.5199	11.7349	12.9324	14.1155	15.2867
$n=3$	10.1735	8.5363	9.9695	11.3459	12.6819	13.9872	15.2682	16.5294	17.7740	19.0046
$n=4$	13.3237	11.7060	13.1704	14.5859	15.9641	17.3129	18.6375	19.9419	21.2291	22.5014
$n=5$	16.4706	14.8636	16.3475	17.7888	19.1960	20.5755	21.9317	23.2681	24.5872	25.8913

Table 4.2 TM (modes) zeroes χ_{mn} of $J_{mn}(\chi_{mn}) = 0 (n = 1,2,3,....)$ of Bessel function $J_m(x)$

	$m=0$	$m=1$	$m=2$	$m=3$	$m=4$	$m=5$	$m=6$	$m=7$	$m=8$	$m=9$
$n=1$	2.4049	3.8318	5.1357	6.3802	7.5884	8.7715	9.9361	11.0864	12.2251	13.3543
$n=2$	5.5201	7.1056	8.4173	9.7610	11.0647	12.3386	13.5893	14.8213	16.0378	17.2412
$n=3$	8.6537	10.1735	11.6199	13.0152	14.3726	15.7002	17.0038	18.2876	19.5545	20.8071
$n=4$	11.7915	13.3237	14.7960	16.2235	17.6160	18.9801	20.3208	21.6415	22.9452	24.2339
$n=5$	14.9309	16.4706	17.9598	19.4094	20.8269	22.2178	23.5861	24.9349	26.2668	27.5838

The electromagnetic energy from the RF source may be injected into a waveguide through a suitable probe. The probe diameter, length and position are very important because the size and shape of the probe determine its frequency, bandwidth and power-handling capability. A greater power-handling capability is directly related to an increased surface area. As the diameter of a probe increases, the bandwidth also increases. The amount of transferred energy can be reduced by decreasing the length of the probe.

The injected electromagnetic energy propagates inside the waveguide with attenuation. The attenuation of a signal is given by:

$$A_{dB} = 10\log_{10}\frac{P_{input}}{P_{output}} \qquad 4.3$$

or in terms of dBm:

$$P\left(dBm\right) = 10.\log_{10}\left(\frac{P\left(watt\right)}{1watt}\right) + 30 \qquad 4.4$$

where P_{input} and P_{output} are the injected and output power levels [39, 83].

4.2 Waveguide design with the geometrical constraints of ELTRAP

We have tested the power flow from an RF generator with a frequency up to 3 GHz in a prototype circular waveguide, which has the same dimensions (9 cm diameter and 102 cm length) as the ELTRAP electrode stack.

It is necessary in particular to design a rectangular waveguide and set the appropriate coupling position within the geometrical constraints of the device. The electron source is located at one end of the device, while the other end can be used for the injection of the IR laser beam and the detection of the scattered radiation, and for the monitoring of the bunch dynamics with a Faraday cup. In the middle, sectored cylinders are used for plasma and bunch dynamics detection and manipulation (see figure 4.2). With these restrictions, the only suitable solution is the transverse injection of the microwave power close to one end of the cylindrical electrode stack. One advantage of this side injection is that it produces only a weak perturbation of the confining field of the plasma and a second advantage is that it determines a stronger heating of the electron plasma, as confirmed also by particle-in-cell (PIC) simulations (see chapter 5).

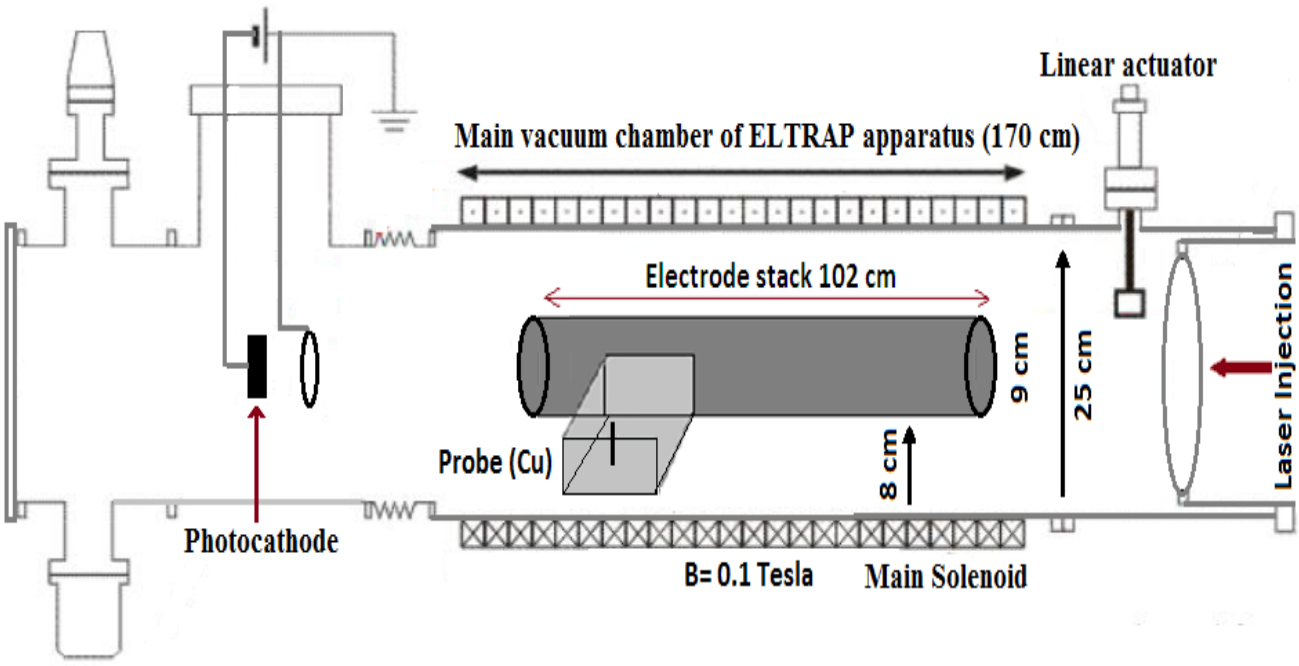

Figure 4.2 Schematic diagram of the waveguide design and coupling with the electrode stack of ELTRAP.

In order to have a similar field configuration at the interface (T-junction) between the two waveguides, the maximum permitted wavelength (dominant mode) of the rectangular waveguide should be less or equal the cutoff wavelength of the TE_{11} mode in the circular waveguide, i.e.

$$2a = \left(\lambda_c\right)^{TE}_{10,rect} \leq \left(\lambda_c\right)^{TE}_{11,cyl} = 1.706\,D \qquad 4.5$$

where in the present case D = 9 cm. This diameter puts therefore a limitation on the major axis of rectangular waveguide,

$$a \leq 7.677\ cm.$$

It is advantageous to work just above the cut-off frequency (dominant mode) of the desired mode (either TE_{mn} or TM_{mn}) to reduce the attenuation in the waveguide (see section 4.3), and reducing the wavelength of the excited mode in both waveguides results in a better transition. In this arrangement both waves have essentially the same field configuration at the interface, and so the wave is able to pass easily from the rectangular to the cylindrical waveguide.

To avoid abrupt dimensional changes and generation of higher-order modes, the length of the rectangular waveguide should be twice that of the guide-wavelength i.e. 2 λg = 30.708 cm. However, the geometrical constraints of the vacuum chamber of the apparatus do not allow to use such a long waveguide. Namely, the length of the rectangular waveguide should be less than 8 cm to be accommodated in the space between the external wall of the cylindrical electrode stack and the internal wall of the UHV chamber of ELTRAP as shown in figure 4.2. Thus, taking into account the above mentioned limitations we opted for an already available rectangular waveguide of dimension a = 7.18 cm, b = 3.71 cm and length 7 cm. The cut off frequency of the rectangular waveguide and of a circular waveguide of diameter 9 cm are as below:

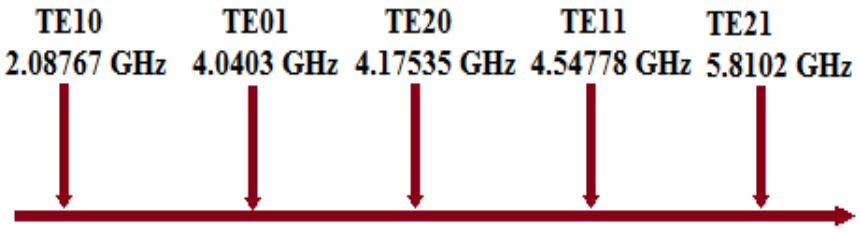

Figure 4.3 The cut-off frequency of rectangular waveguide of dimension a= 7.18 cm and b=3.71 cm

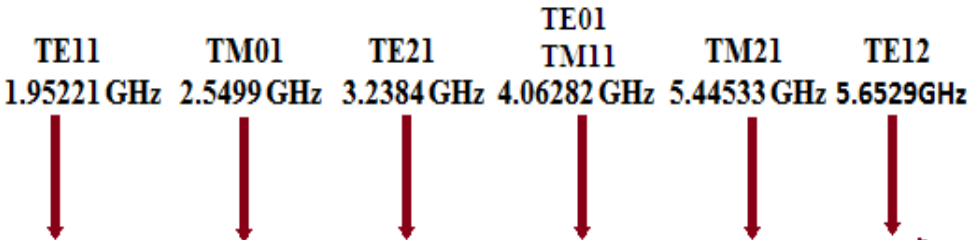

Figure 4.4 The cut-off frequency of circular waveguide of diameter 9 cm

The general properties of the modes in the circular waveguide are similar to those for the rectangular waveguide. However, in contrast to the rectangular waveguide, the dominant mode in the circular waveguide is TE_{11} instead of TE_{10}. Secondly, due to the frequency limitation at 3 GHz of the available RF power supply only a single polarized mode (TE_{10}) can propagate in the rectangular waveguide, while in the circular waveguide both polarizations i.e. both TE_{11} and TM_{01} can be excited (see figures 4.3 and 4.4). The schematic diagram 4.5 shows how the power can be transferred from the TE_{10} rectangular waveguide mode to the TE_{11} and TM_{10} circular waveguide modes.

The probe is a wire made of conductive material. Since there is no loop for current to flow in and create a magnetic field, the probe must be an electric field transformer. The probe is placed near the maximum of the field pattern of the desired mode in the waveguide. The most efficient place

to locate the probe is in the center of the “a” wall, parallel to the “b” wall, and one quarter-wavelength from the shorter end of the waveguide (backshort). This is the point at which the E field is maximum in the dominant mode. Therefore, energy transfer (coupling) is maximum at this point. Note that the quarter-wavelength spacing is at the frequency required to propagate the dominant mode.

In order to characterize the transmission efficiency, a suitable absorber has been put at the end of the circular waveguide, in order to avoid the reflection of the propagating modes (and therefore the generation of standing wave) due to an impedance mismatch between the waveguide and the free space.

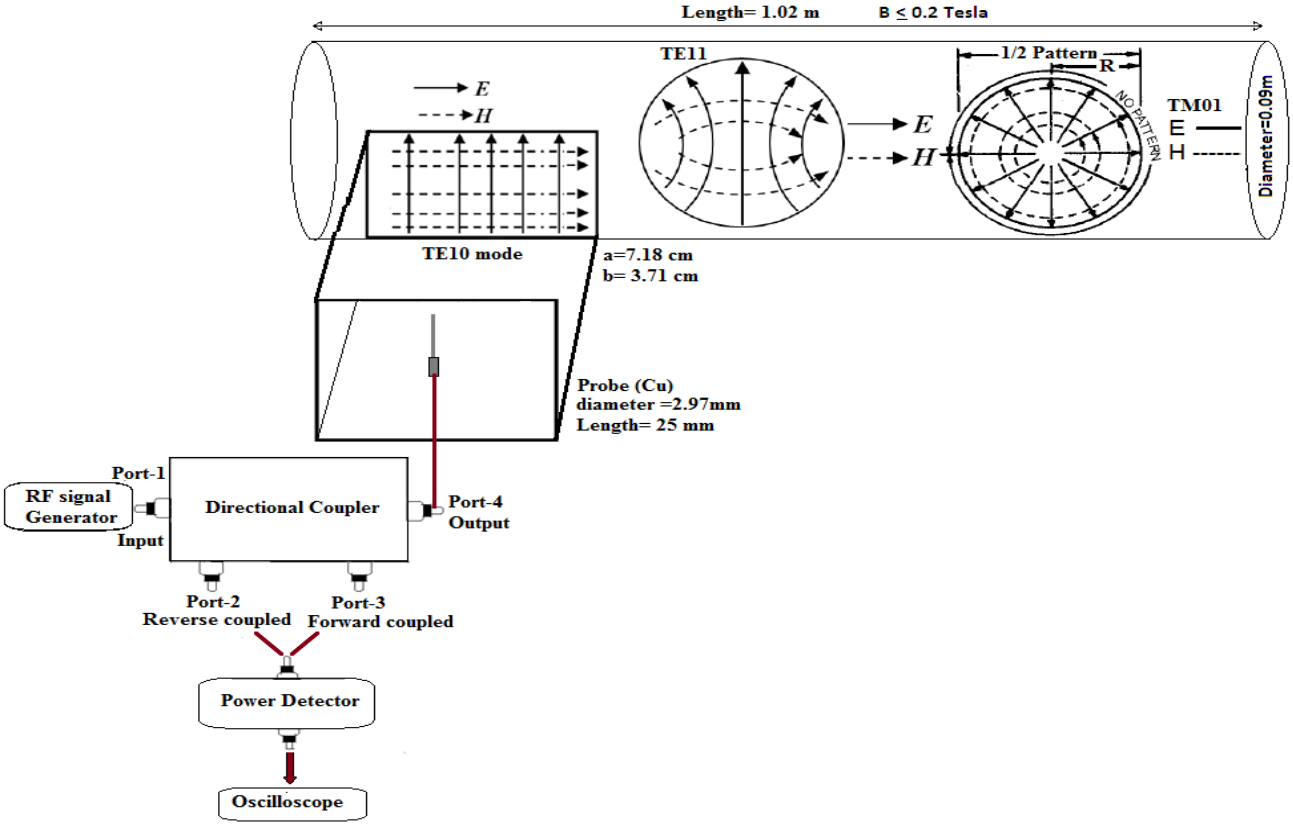

Figure 4.5 Schematic diagram of field transition from rectangular (TE_{10} mode) to circular waveguide (TE_{11} and TM_{01} modes) via T-junction.

4.3 Waveguide mode transform, attenuation and excitation technique

The schematic diagram of the microwave transmission system and the field’s transition from the rectangular to the circular waveguide is shown in figure 4.5. The directional coupler is a four-port

network waveguide device used to accurately sample the injected microwave power from the RF source into the device under test (waveguide). The RF signal generator is connected to port 1 of the directional coupler to inject the desired power into the prototype circular waveguide via a metal probe in the rectangular waveguide, which is connected to port 4 of directional coupler. The power detector connected on the auxiliary line of the directional coupler at port 2 and 3 samples a portion of the reflected and transmitter wave and the data are recorded on an oscilloscope connected to the power detector.

In the T-junction it is necessary to couple the power from the rectangular waveguide to the circular waveguide with a low return loss. In order to achieve this result, the basic principle is to try to ensure that the electric and magnetic field patterns on the two sides of the junction are roughly similar. Since the field patterns do not usually match, some of the RF power is scattered into higher order modes. Provided these are in cut off, no power can propagate in them and it therefore remains stored as reactive energy in the region close to the junction. The mismatch caused by this reactance can be tuned out by the addition of matching elements (posts or irises) to give a good overall voltage standard wave radio (VSWR). Rather different problems arise when the higher order modes can propagate because significant power can then be transferred into undesired modes. This should not normally happen at the fundamental frequency, but it can cause problems at higher frequencies. With the available RF source up to 3 GHz and a ≤ 0.2 T homogeneous magnetic our working range is practically the fundamental frequency. When the rectangular waveguide is terminated into the circular one, the resulting wave has magnetic field lines which are approximately circular in shape, so that little field distortion happens at the interface as shown in figure 4.5.

The field pattern for the two modes TE_{10} and TE_{20} in a rectangular waveguide is shown in figure 4.6.

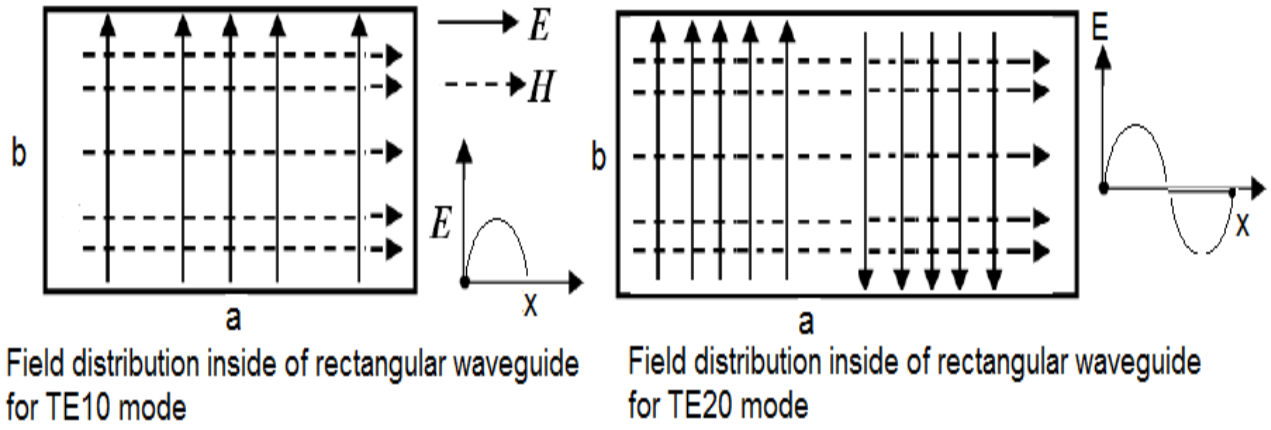

Figure 4.6 Field distribution inside of rectangular waveguide for TE10 and TE20 modes

1. In both cases, E only varies in the x direction; since n = 0, it is constant in the y direction.
2. For TE_{10}, the electric field has a half sine wave pattern, while for TE_{20} a full sine wave pattern is observed.

The field pattern for the two modes TE_{11} and TM_{01} in a circular waveguide is shown in figure 4.7.

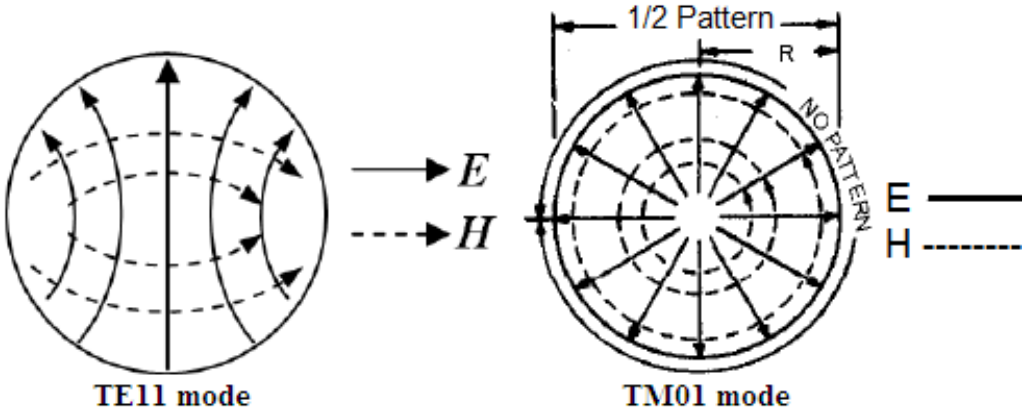

Figure 4.7 Field distribution inside of circular waveguide for TE_{11} and TM_{01} modes

Attenuations in the waveguide commonly derive from dielectric and conductor losses. The fields associated with the propagating waveguide modes produce currents that flow in the walls of the waveguide. In ELTRAP, OFHC (oxygen-free high conductivity) copper cylinders of conductivity $\sigma_c = 5.8\times10^7\ \Omega/m$ are used. Under ultra-high vacuum conditions the dielectric loss is negligibly small. The wave impedance in a rectangular waveguide of the TE_{10} dominant mode at 3 GHz operating frequency is

$$Z_{10}^{TE} = \frac{120\,\pi\,\Omega}{\sqrt{1-\left(\frac{f_c}{f}\right)^2}} = \frac{377\Omega}{\sqrt{1-\left(\frac{2.08767}{3}\right)^2}} = 524.961\Omega \quad (4.6)$$

The wave impedance in a circular waveguide of the TE_{11} dominant mode at 3 GHz operating frequency is:

$$Z_{11}^{TE} = \frac{120\,\pi\,\Omega}{\sqrt{1-\left(\frac{f_c}{f}\right)^2}} = \frac{377\Omega}{\sqrt{1-\left(\frac{1.95221}{3}\right)^2}} = 496.51\Omega \quad (4.7)$$

where the wave propagation constant of the TE_{11} mode is:

$$\beta_g(TE_{11}) = \frac{2\pi f}{c} \times \sqrt{1-\left(\frac{f_c}{f}\right)^2}\, m^{-1} = 47.7419 m^{-1} \quad (4.8)$$

The ratio of the transverse electric field to the transverse magnetic field for a propagating mode at a particular frequency is the waveguide impedance.

The impedance of the TE_{11} mode at 3 GHz propagating in a circular waveguide with a length of l = 1.02 m is

$$Z(circular) = Z_{11}^{TE} \tan(\beta l) = 565.09\Omega \quad (4.9)$$

The wave impedance of the TM_{01} mode at 3 GHz is

$$Z_{01}^{TM} = 377 \times \left(\sqrt{1-\left(\frac{f_c}{f}\right)^2}\right) = 198.6173\Omega \quad (4.10)$$

where the wave propagation constant of the TM_{01} mode is

$$\beta_g(TM_{01}) = \frac{2\pi f}{c} \times \sqrt{1-\left(\frac{f_c}{f}\right)^2}\, m^{-1} = 33.125 m^{-1} \quad (4.11)$$

Finally, the impedance of the TM_{01} mode at 3 GHz propagating in a circular waveguide with length l = 1.02 m is

$$Z(circular) = Z_{01}^{TM} \tan(\beta l) = 132.901\Omega \qquad 4.12$$

Equation 4.6 and 4.12 indicate that the impedance in a rectangular waveguide is higher than in a circular waveguide.

In case of the TE_{mn} mode, for the wave impedance given in equations 4.6 and 4.7 it results that:

1. Above the cut off it is real and greater than the intrinsic impedance of the medium inside the waveguide.
2. At cutoff the impedance is infinite.
3. Below cut off it is imaginary and inductive. This indicates that the waveguide below cutoff behaves as an inductor that is an energy storage element.

In case of the TM_{mn} mode, for the wave impedance as shown in equation 4.10 it results that:

1. Above cut off it is real and smaller than the intrinsic impedance of the medium inside the waveguide.
2. At cut off impedance is zero.
3. Below cut off it is imaginary and capacitive. This indicates that the waveguide below cutoff behaves as a capacitor that is an energy storage element.

In order to calculate the attenuation constant of the TE_{11} and TM_{01} modes in a copper circular waveguide, it is necessary to take into account the surface resistance of the circular waveguide 'R_s' which depend on the skin depth 'δ' by the relation

$$R_s = \frac{1}{\delta_s \sigma_c} = 0.01429\Omega \quad \text{where} \quad \delta = \frac{1}{\sqrt{\pi\ f\ \mu_0\ \sigma_c}} = 1.20655\mu m\ \left(\text{skin depth}\right)$$

The skin depth of the copper circular waveguide walls at the operating frequency of 3 GHz is 1.20655 µm. The attenuation constant of the TE_{11} mode in a circular waveguide is

$$\left(\alpha_c\right)_{11}^{TE} = \frac{R_s}{a\eta'\sqrt{1-\left(\frac{f_c}{f}\right)^2}}\left[\left(\frac{f_c}{f}\right)^2 + \frac{m^2}{\chi_{mn}^2 - m^2}\right] = 9.3391\times10^{-4}\frac{N_p}{m} \quad 4.13$$

$$\left(\alpha_c\right)_{11}^{TE} = 9.3391\times10^{-4}\frac{N_p}{m} \quad 4.14$$

where Np is the neper. Passing to decibel,

$$20\log_{10}\left(e^{-\left(\alpha_c\right)_{11}^{TE}L}\right) = -0.0082741\,\text{dB/m} \quad 4.15$$

In term of power loss

$$A_{dB}\left(TE_{11}\right) = -0.0082741 = 10\log_{10}\left(\frac{P_{input}}{P_{output}}\right)$$

$$P_{input}\left(TE_{11}\right) = 0.99917P_{output} \quad 4.16$$

The attenuation constant of the TM_{01} is

$$\left(\alpha_c\right)_{01}^{TM} = \frac{R_s}{a\eta'\sqrt{1-\left(\frac{f_c}{f}\right)^2}} = \frac{0.01429}{(0.045)(377)\sqrt{1-\left(\frac{2.5499}{3}\right)^2}} = 0.0015988\frac{Np}{m} \quad 4.17$$

where Np is the neper. Passing to decibel,

$$20\log_{10}\left(e^{-\left(\alpha_c\right)_{01}^{TM}L}\right) = -0.014165\,\text{dB/m} \quad 4.18$$

In term of power loss $$A_{dB}(TM_{01}) = -0.01416478 = 10\log_{10}\left(\frac{P_{input}}{P_{output}}\right) \quad 4.19$$

$$\mathrm{P}_{\mathrm{input}}(TM_{01}) = 0.99858P_{output} \quad 4.20$$

Equations 4.16 and 4.20 shows that the power losses of the TE_{11} and TM_{01} modes in the circular waveguide is negligibly small, meaning that the position of the T-junction does not play a big role regarding attenuation. However equations 4.13 and 4.17 (see figures 4.8 and 4.9) indicate that for a constant power in the waveguide the f_c/f component decreases as the operating frequency increases and approaches zero at infinite frequency. In the opposite case, attenuation rises very sharply and approaches infinity when the operating frequency decreases toward cut off but the approximations under which these equations were developed are not valid in the region immediately adjacent to the cut off wavelength $f = f_c$.

The study of electric and magnetic field components in a circular waveguide show that the only tangential magnetic field component to the conducting surface of the waveguide for all these TE_{0n} (n=1, 2, 3…) modes is the H_z component, while the electric field lines are circular. Therefore, these modes are usually referred to as circular electric modes. When the frequency increases at a constant power level, the H_z component decreases accordingly and simultaneously the current density and conductor losses on the waveguide walls also decrease and approach zero with increasing frequency. On the contrary, TM_{mn} modes have a component of the electric field parallel to the guide axis, but a magnetic field component that is everywhere transverse to the axis.

Plots of the attenuation coefficient computed from equations 4.13 and 4.17 versus the normalized frequency f_c/f are shown for six modes for a circular waveguide of radius 1.5 cm in figure 4.8 and radius 3 cm in figure 4.9. The cut off frequency used is the dominant TE_{11} mode with corresponding value of 5.8566 GHz in figure 4.8 and 2.9283 GHz in figure 4.9. Inside the waveguide the dielectric is free space and the walls are made of copper ($\sigma_c = 5.8\times10^7\,\Omega/m$).

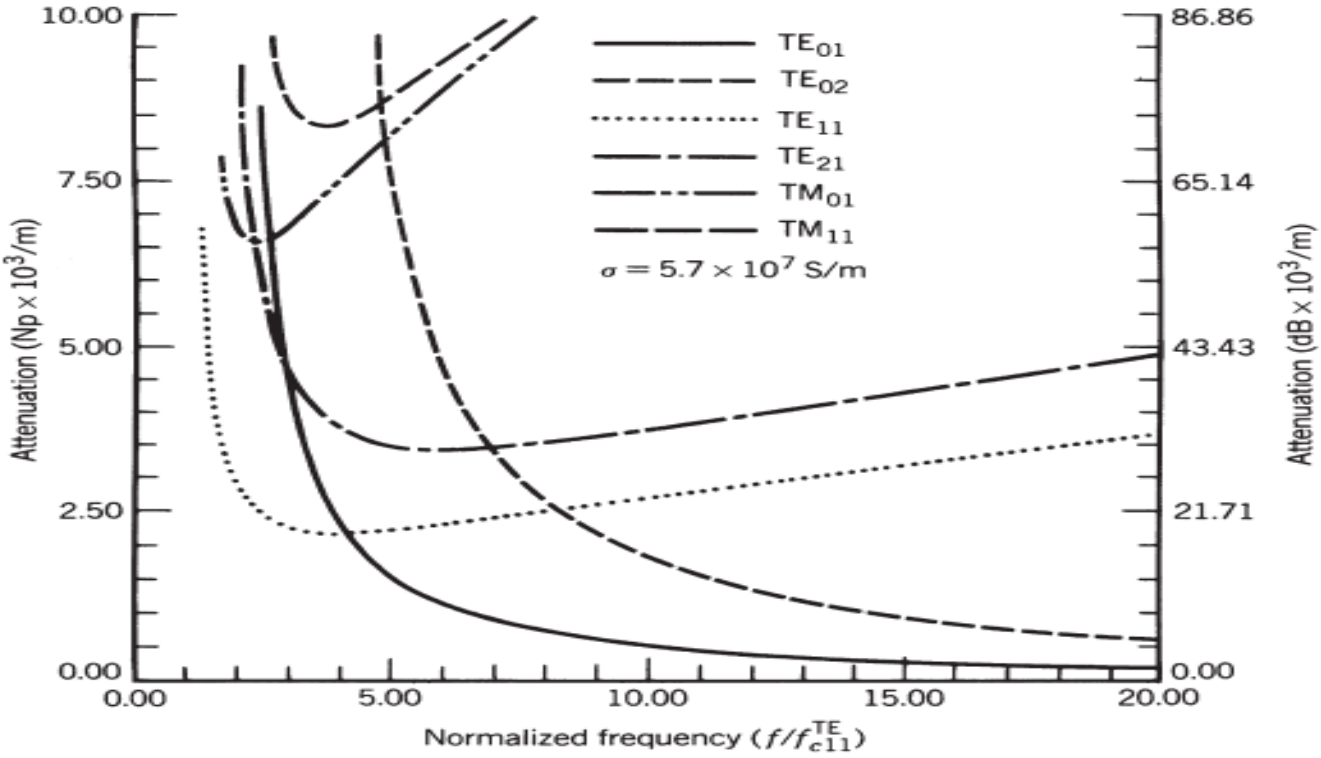

Figure 4.8 Attenuation for TE_{mn} and TM_{mn} modes in a circular waveguide of radius a=1.5 cm.

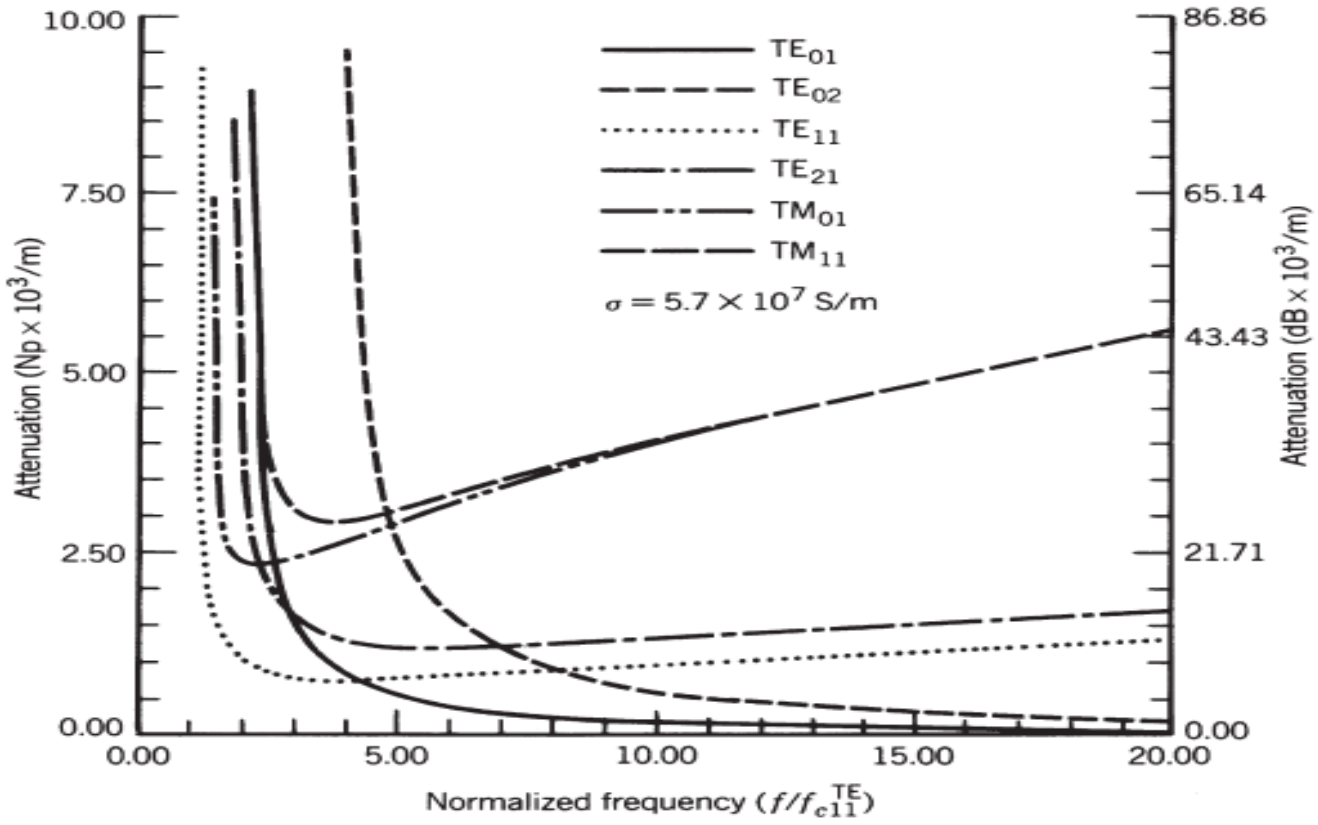

Figure 4.9 Attenuation for TE_{mn} and TM_{mn} modes in a circular waveguide of radius a= 3 cm.

Another issue that requires more attention is the excitation method. The dominant mode of the circular waveguide is less easily excited with respect to the dominant mode of the rectangular waveguide. The rectangular waveguide has a relatively higher attenuation with respect to the circular waveguide, but it is more frequently used due to the ease of the excitation method by means of a suitable metal probe. An appropriate design of the metal probe diameter and length as well as position is necessary in order to maximize the energy exchange or transfer so that the field pattern matches that of the desired mode. Usually the probe is placed near the maximum of the field pattern of the desired mode; however, that position may be varied somewhat especially in the T-junction of the waveguide. In order to achieve some preferred matching in the excitation and detection systems it is better to tune the probe in the waveguide for maximum electric field intensity detecting the maximum peak signal on an oscilloscope.

Although the TE_{0n} (n=1, 2, 3…) modes are very attractive from the attenuation point of view, there are a number of problems associated with their excitation and retention. One of the problems is that the TE_{01} mode is not the dominant mode as shown in figure 4.4. Therefore, in order for the TE_{01} mode to be above its cut off frequency and propagate in the waveguide, a number of other modes like TE_{11}, TM_{01}, TE_{21}, and TM_{11} with lower cutoff frequencies can also exist. If the operating frequency in waveguide is chosen well above the cutoff frequency i.e. 4.06282 GHz of the TE_{01} mode then additional modes having cut off frequency lower than 4.06282 GHz can also be present and such a waveguide is called over mode. In order to provide a margin of safety it is better to be not too close to its cut off frequency. One of the problems faced with such a waveguide is how to excite the desired TE_{01} mode with sufficient purity and suppress the others. Another problem is how to prevent coupling between the TE_{01} mode and undesired modes. The presence of the undesired modes causes not only higher losses but also dispersion and attenuation distortion to the signal since each mode exhibits different phase velocity and attenuation. Irregularities in the inner geometry, surface, and direction (bends, non-uniform cross sections, etc.) of the waveguide are the main contributors to the coupling to the undesired modes. A method used to discriminate undesired modes and avoid coupling to them is to introduce filters inside the guide that cause negligible attenuation to the desired TE_{0n} (n=1, 2, 3…) mode. These filters introduce cuts that are perpendicular to the current paths of the undesired modes and parallel to the current direction of the desired modes. Since the current path of the undesired modes is along the axis (z direction) of the guide and the path of the desired TE_{0n} (n=1, 2, 3…) modes is along the circumference (ϕ direction), a helical wound wire placed on the inside surface of the guide can serve as a filter that

attenuates any mode that requires an axial component of current flow but propagates the desired TE_{0n} (n=1, 2, 3…) modes [26, 39, 41, 91].

4.4 RF power transmission in the waveguide

The power that can be transmitted through a waveguide depends upon the electric field strength that can exist without breakdown. If this maximum allowable field strength is specified, the maximum power carrying capacity of the waveguide can be calculated when the wavelength and the size of the guide are known. The maximum power that can be carried by a rectangular waveguide at 3 GHz for the dominant TE_{10} mode is:

$$\frac{P}{E_{\max}^2} = 6.63\times 10^{-4} ab\left(\frac{\lambda}{\lambda_g}\right) = 0.01229 watts \qquad 4.21$$

where a=7.18cm, b=3.71 cm and E_{max} is the potential gradient expressed in volts per centimeter. Taking into account the maximum power 20 dBm = 0.1 W of the available RF signal generator $E_{\max} = 2.8525 volts/cm$. This maximum field intensity is parallel to the b dimension of the guide, midway between the side walls of the rectangular waveguide.

Similarly the maximum power that can be carried out by a circular waveguide at 3 GHz for the TE_{11} mode is:

$$P_{11}^{TE} = 1.99\times 10^{-3} a^2\left(\frac{\lambda}{\lambda_g}\right) E_{\max}^2 watts = 0.026223 E_{\max}^2 \text{ watts} \qquad 4.22$$

$$where\ \mathrm{a} = 4.5\,\mathrm{cm}, \lambda_g = \frac{2\pi(4.5)}{1.8412} = 15.356471 cm \text{ and } \lambda = 9.993\mathrm{cm}$$

Taking into account that the maximum power of the available RF signal generator is 0.1 W = 20dBm, the maximum filed in the circular waveguide is $E_{\max} = 1.9528 volts/cm$.

For the magnetic TM_{01} mode there are two separate cases:

$$P(watts)=\begin{Bmatrix} 7.69\times10^{-3}\,\dfrac{a^4}{\lambda^2}\left(\dfrac{\lambda}{\lambda_g}\right)E_{max}^2,\ if\ \dfrac{a}{\lambda}<0.761(Maximum\ \text{field intensity is at the center of the guide}) \\ 3.33\times10^{-3}\,a^2\left(\dfrac{\lambda_g}{\lambda}\right)E_{max}^2,\ if\ \dfrac{a}{\lambda}>0.761(Maximum\ \text{field intensity is at r} = 0.765a) \end{Bmatrix}$$

$$P_{01}^{TM}=0.0268402E_{max}^2\,watts \qquad 4.23$$

In this case $E_{max}=1.93022\,volts/cm$ [39, 40, 41].

4.5 Power flow measurement devices

In order to measure the return loss in the prototype circular waveguide, a directional coupler, a data display (oscilloscope) and RF detectors that accurately detect and measure the RF power are needed.

4.5.1 Directional coupler

A directional coupler model ZABDC20-322H has been used. This is a four-port network that is designed to divide and distribute the RF power and also used to sample the propagating microwave energy for the purpose of monitoring or measuring as shown in figure 4.10. In the directional coupler portions of the forward and backward traveling waves (two transmission lines) on an auxiliary line are coupled at port 2 and port 3 through a power and the data displayed on an oscilloscope are stored for a subsequent analysis.

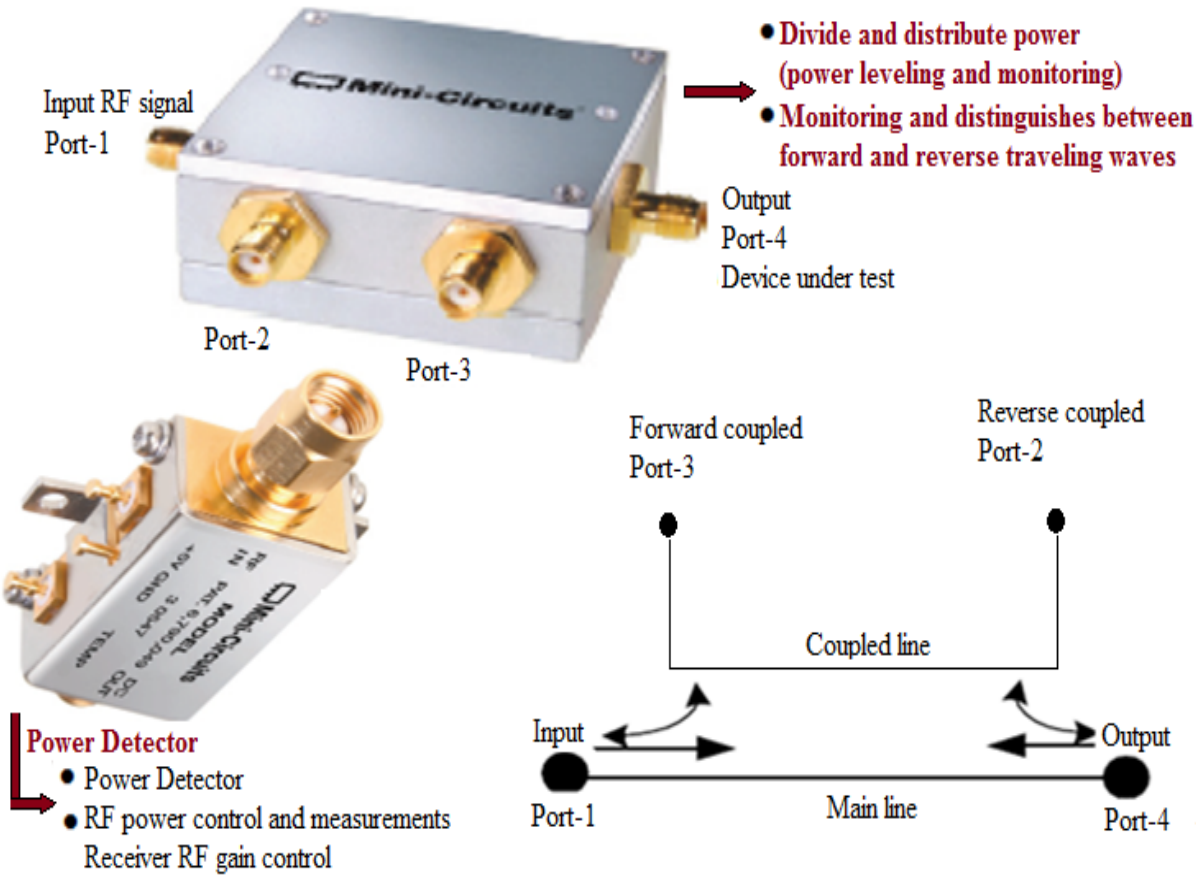

Figure 4.10 Schematic diagram of directional coupler

The performance of a directional coupler is usually described in terms of its coupling and directivity. The coupling factor or coupling (C) is defined as the ratio of the transmitted power (incident) at the input of the main line to the power at the output in the auxiliary line. Thus, the coupling is a measure of how much of the incident power is being sampled,

$$Coupling \quad (dB) = 10\log\frac{P_{inc}}{P_{cp}} \rightarrow \begin{Bmatrix} \text{-20dB} \ (99\% \text{ transmitted}) \\ \text{-10dB} \ (90\% \text{ transmitted}) \\ \text{-6dB} \ (75\% \text{ transmitted}) \\ \text{-3dB} \ (50\% \text{ transmitted}) \end{Bmatrix} \qquad 4.24$$

where P_{inc} is the incident power (transmitted power) at the input port 1 and P_{cp} is the power coupled at port-3 i.e. transmitted power on the auxiliary line. Note that the larger the coupling value, the smaller the coupled power. For example a 6 dB coupler couples out 25% of the input

power, similarly a 10 dB coupler couples out 10% of the input power, a 20 dB coupler couples out 1.0% of the input power and a 30 dB coupler couples out 0.1% of the input power.

The frequency dependent directivity is a measure of how well the coupler distinguishes between transmitted wave and reflected wave. The directivity is the ratio of the power out of the coupling Port-3 i.e. $P_3(dB)$ to the power out of the isolation port-4 i.e. $P_4(dB)$ expressed as:

$$Directivity(dB) = 10\log\frac{P_3(dB)}{P_4(dB)}$$

This value indicates how effective the device is in "directing" the coupled energy into the correct port (i.e., into the coupled port, not the isolation port). For an ideal directional coupler, $P_{dir} = P_4 = 0$ and therefore the directivity is infinite [106].

4.5.2 Power detector calibration

For the RF power measurements and control we used a power detector model ZX47-40LN. It has a high dynamic range from -40 dBm to +20 dBm from 10 MHz to 8 GHz. For the calibration, its input terminal is connected to the output of the RF generator through a RF cable and its exit terminal to an oscilloscope to record the data as shown in figure 4.11. A 3 GHz RF signal with a power level between –40 to 0 dBm was injected into the detector with a sweep time of 10 seconds. The recorded data have been fitted as $Y = -0.0246X + 0.9876$, where X is the detected power in dBm and Y the output voltage of the power detector connected to ports 3 and 2 of the directional coupler.

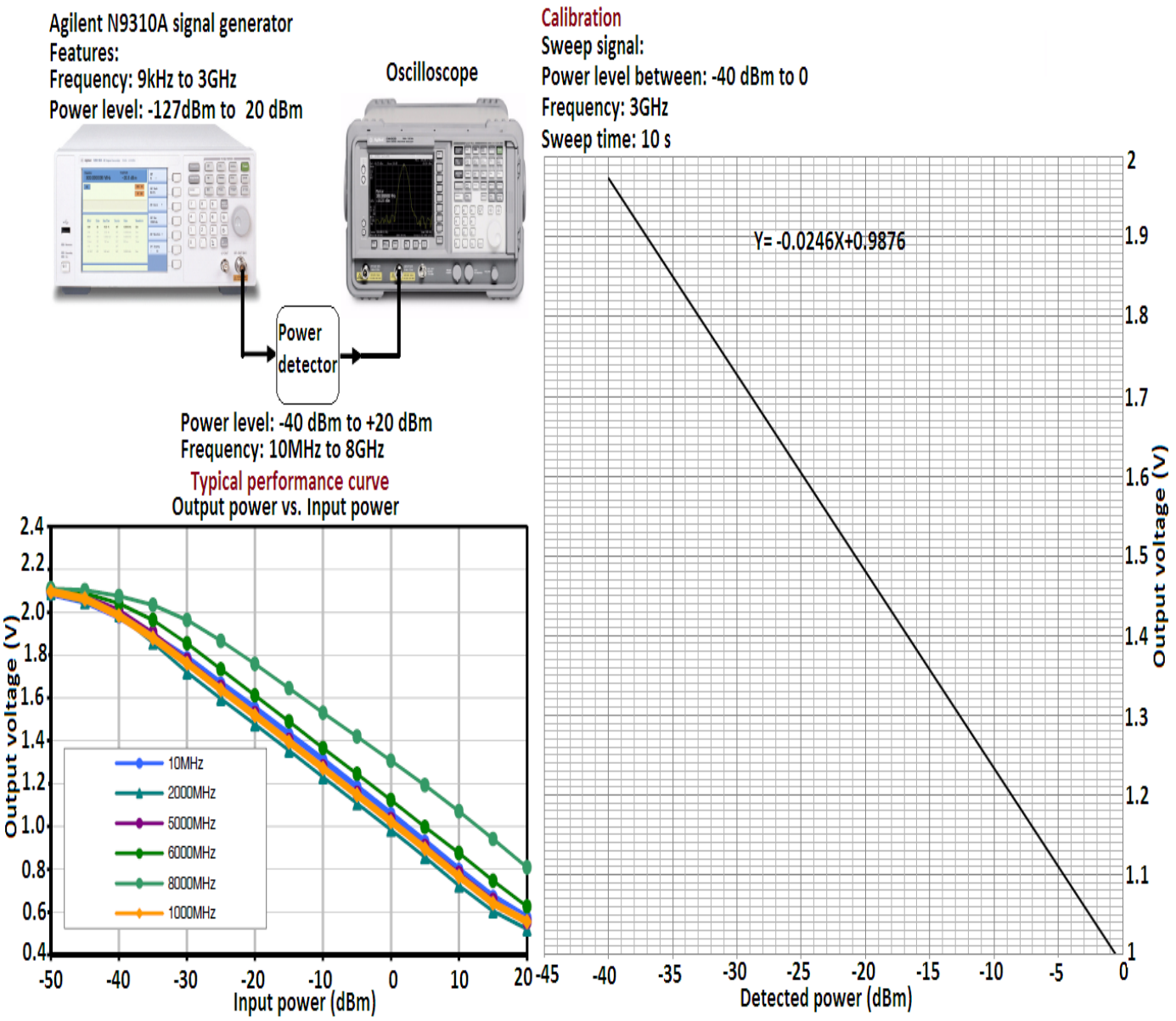

Figure 4.11 Schematic diagram of the detector calibration

4.6 Power flow measurements in a prototype circular waveguide

The microwave transmission design is discussed in section 4.2. A length of 7 cm of the rectangular waveguide was selected due to the geometric constraints of the vacuum chamber of ELTRAP. The electrode stack of diameter 9 cm is lodged inside a cylindrical UHV chamber of diameter 25 cm, so that the rectangular waveguide length must be < 8 cm to be plugged perpendicularly to the cylindrical electrode stack as indicated in figure 4.2.

Initially the transmission efficiency of a rectangular waveguide of dimensions a = 7.18 cm, b = 3.71 and length = 31 cm ≈ 2 λg = 30.708 cm, which is the optimum dimension for a 3 GHz frequency,

has been analyzed. The return loss measurements have been performed according to scheme shown in figure 4.12.

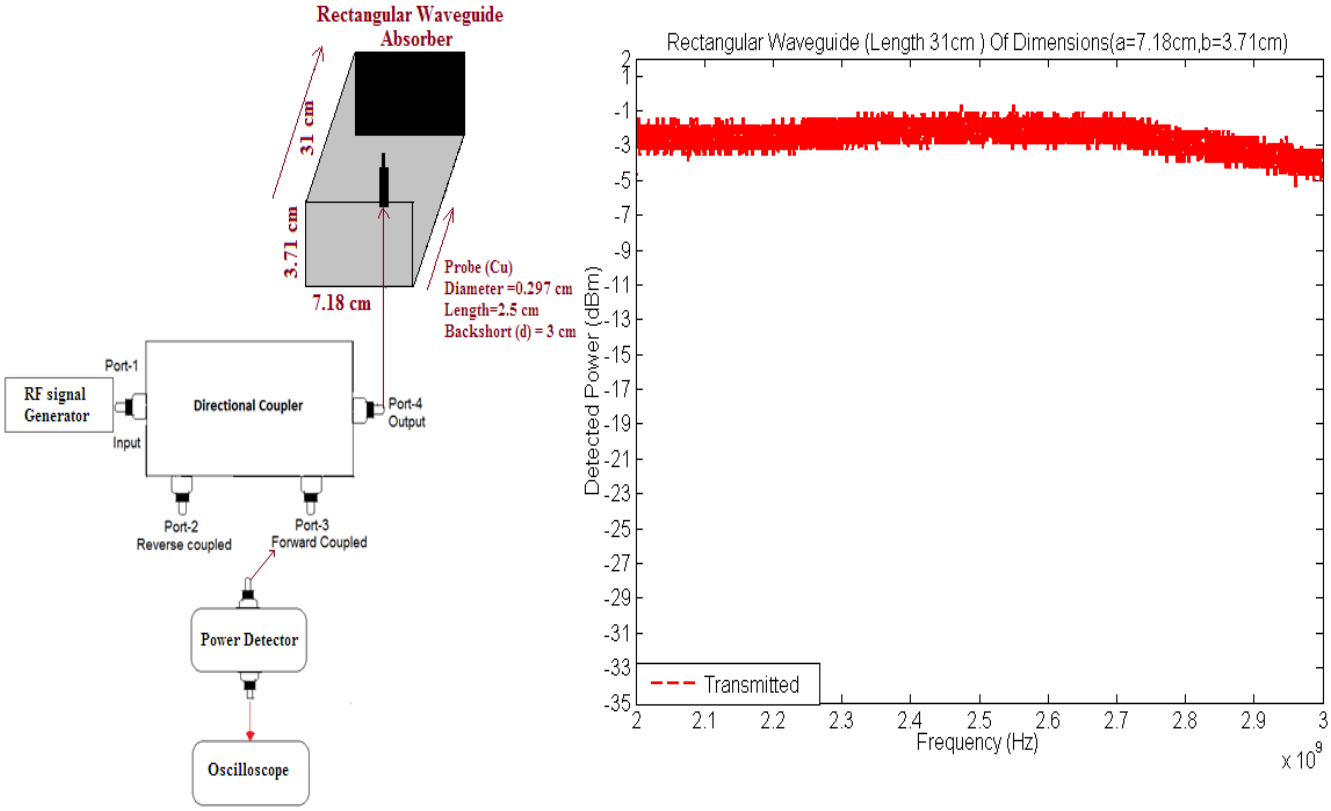

Figure 4.12 Schematic diagram of experimental set up and transmitted power from RF generator to output of directional coupler

The RF signal of the generator has been swept between 2 GHz to 3 GHz using a power level of 20.0 dBm and injected into port 1 of directional coupler. The signal exits from the output terminal, i.e. port-4, and enters into the rectangular waveguide through a copper probe. The power detector connected at port 3 receives a portion of the transmitted power and the data is recorded on the oscilloscope. Using the calibration shown in figure 4.11 the transmitted power is computed as

$$P_{trans}(output) = -\frac{V_{trans} - 0.9876}{0.02446} dBm \qquad 4.25$$

and the result is shown in figure 4.12 and for other schemes in 4.18 and 4.21. Similarly, if the power detector is connected at port 2 on the auxiliary line of the directional coupler then the power injected into the rectangular waveguide comes back into the directional coupler through

port-4 with a certain attenuation and a portion of the reflected power is detected through port-1. The reflected power is computed as

$$P_{refl}(output) = -\frac{V_{refl} - 0.9876}{0.02446}\, dBm \qquad 4.26$$

and the result is shown in figures 4.19 and 4.22. The return loss is the ratio of the reflected to incident power,

$$\text{Return Loss(dB)} = 10\log_{10}\left(\frac{P_{transmitted}}{P_{reflected}}\right) \qquad 4.27$$

At a detected power level of -3 dBm a fraction of 50 % of the power is reflected and 50 % transmitted in the circular waveguide, while at -6 dBm 25 % is reflected and 75 % transmitted. Similarly at -10 dBm 10 % is reflected and 90 % transmitted and at -20 dBm 1 % reflected and 99 % transmitted. The return loss in dB can then be calculated as the difference between the transmitted (incident) power $P_{trans}(in\ dBm)$ and the reflected power $P_{refl}(in\ dBm)$and the result is shown in figure 4.13. Similarly for other schemes adopted for the return loss measurements as shown in figures 4.14 and 4.17, the results are indicated in figures 4.15, 4.16 and 4.20, 4.23 respectively.

The probe dimension plays a major role to maximize the power exchange from the RF generator into the rectangular waveguide. The dimensions of the copper probe (length 7 cm and diameter 0.297 cm) have been chosen on the basis of the Smith chart impedance plot and taking into account the dimensions of commercially available probes compatible with an RF of 3 GHz. The probe has been plugged at the center of the main dimension of the rectangular waveguide on a movable slide along the other dimension to find the electric field intensity (3 cm from the end close to the circular waveguide).

As mentioned in section 4.3 the impedance of the desires TE_{11} mode (equation 4.9) and TM_{01} modes (equation 4.12) propagating in the circular waveguide are 565.09 Ω and 132.901 Ω, respectively, and they do not match the impedance of free space i.e. 377 Ω. This change in

impedance produces standing waves causing a decrease of the efficiency of the waveguide. To overcome this problem the end of a waveguide was closed with a suitable absorber.

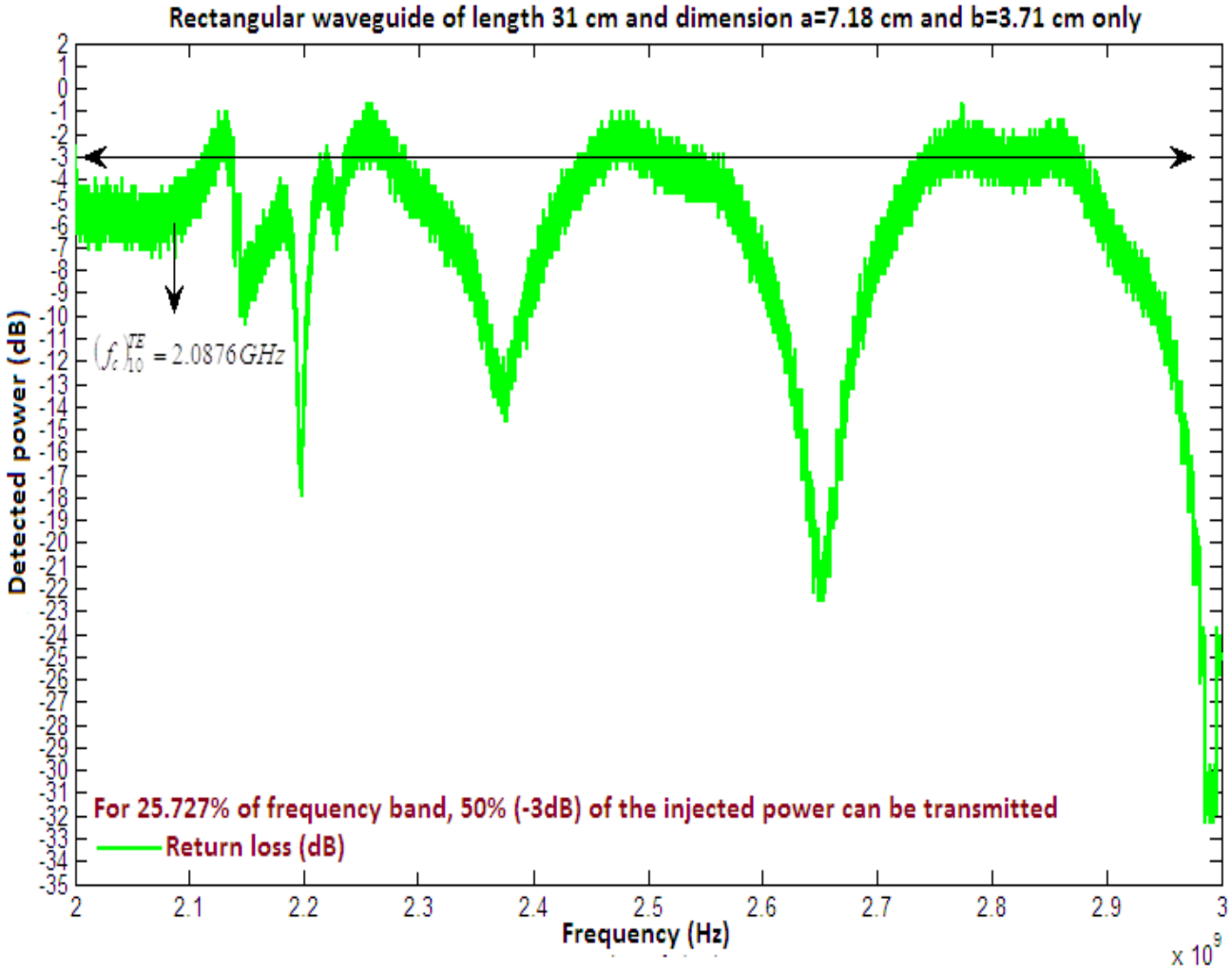

Figure 4.13 Return loss measurements of rectangular waveguide only

The result in figure 4.13 shows that the rectangular waveguide of dimensions a = 7.18 cm, b = 3.71 and length = 31 cm satisfies the desired specifications for reflection and bandwidth. It is shown in particular that 25.727 % of the working frequency band from 2 GHz to 3 GHz has a transmission of 50 % (-3 dBm) and the maximum value of transmission occur at ≈ -33 dB at a frequency of ≈ 3 GHz.

The effect on transmission efficiency and return loss of the rectangular waveguide (length 31 cm) coupled orthogonally (T-junction) with the prototype circular waveguide as well as with additional cylinder of length 7 cm has been investigated as shown in figure 4.14 (a) and (b). A RF signal swept between 2 GHz and 3 GHz at a power level of ±20.0 dBm is used and the return loss measurements are reported in figures 4.15 and figure 4.16, respectively.

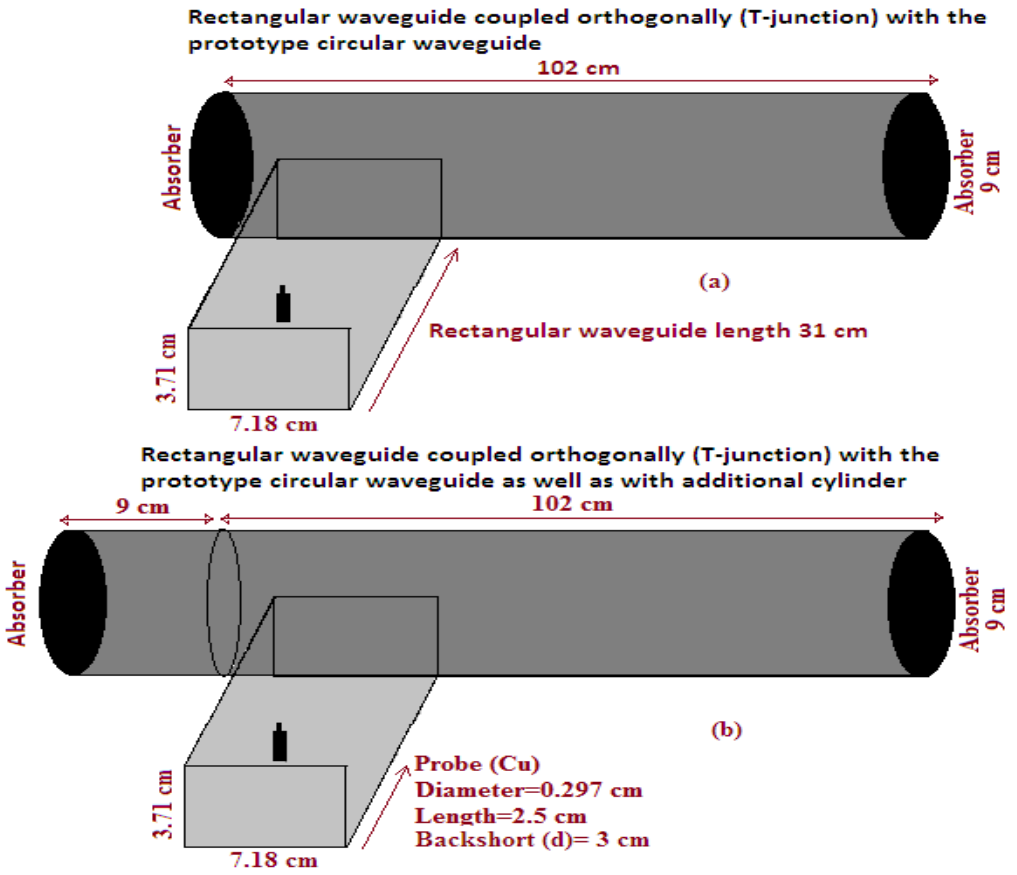

Figure 4.14 Arrangement of power flow measurements with a 31 cm rectangular waveguide

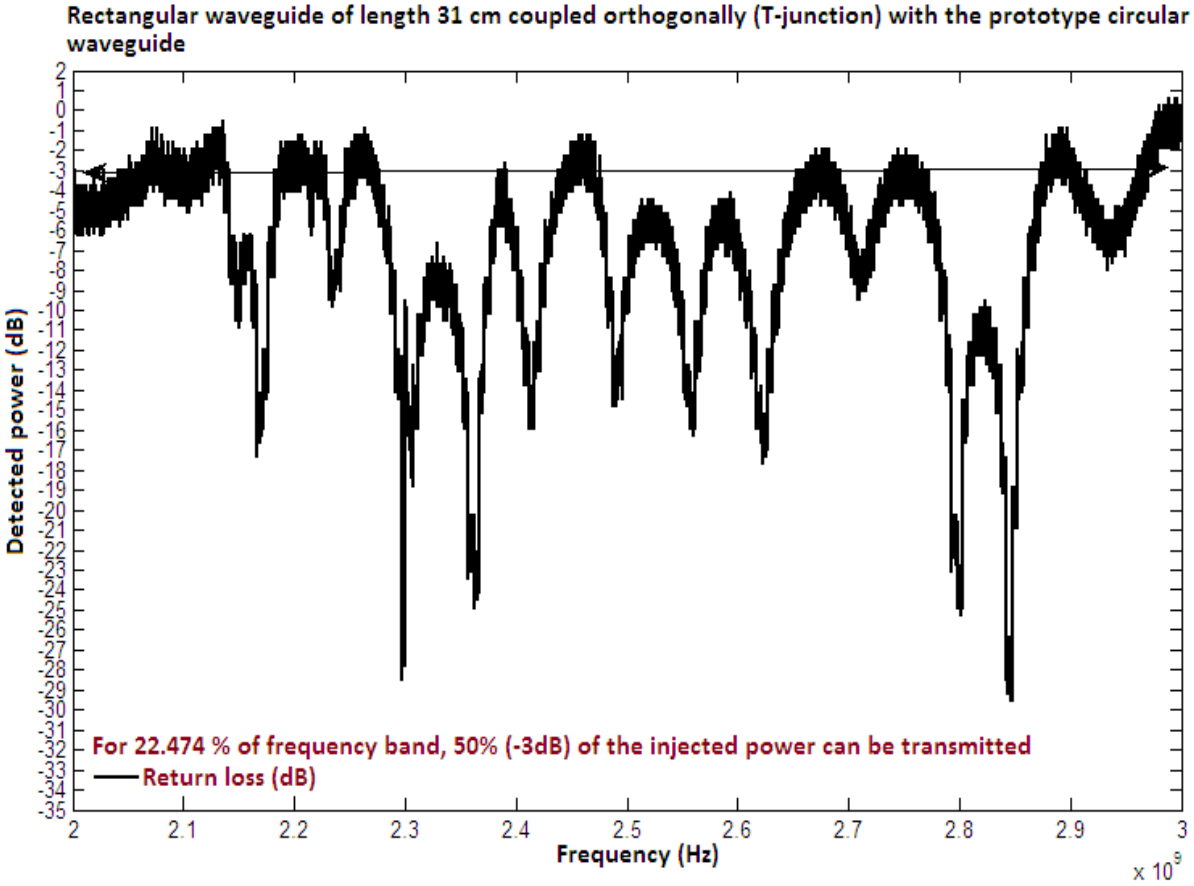

Figure 4.15 Return loss measurements of rectangular waveguide coupled with the circular waveguide

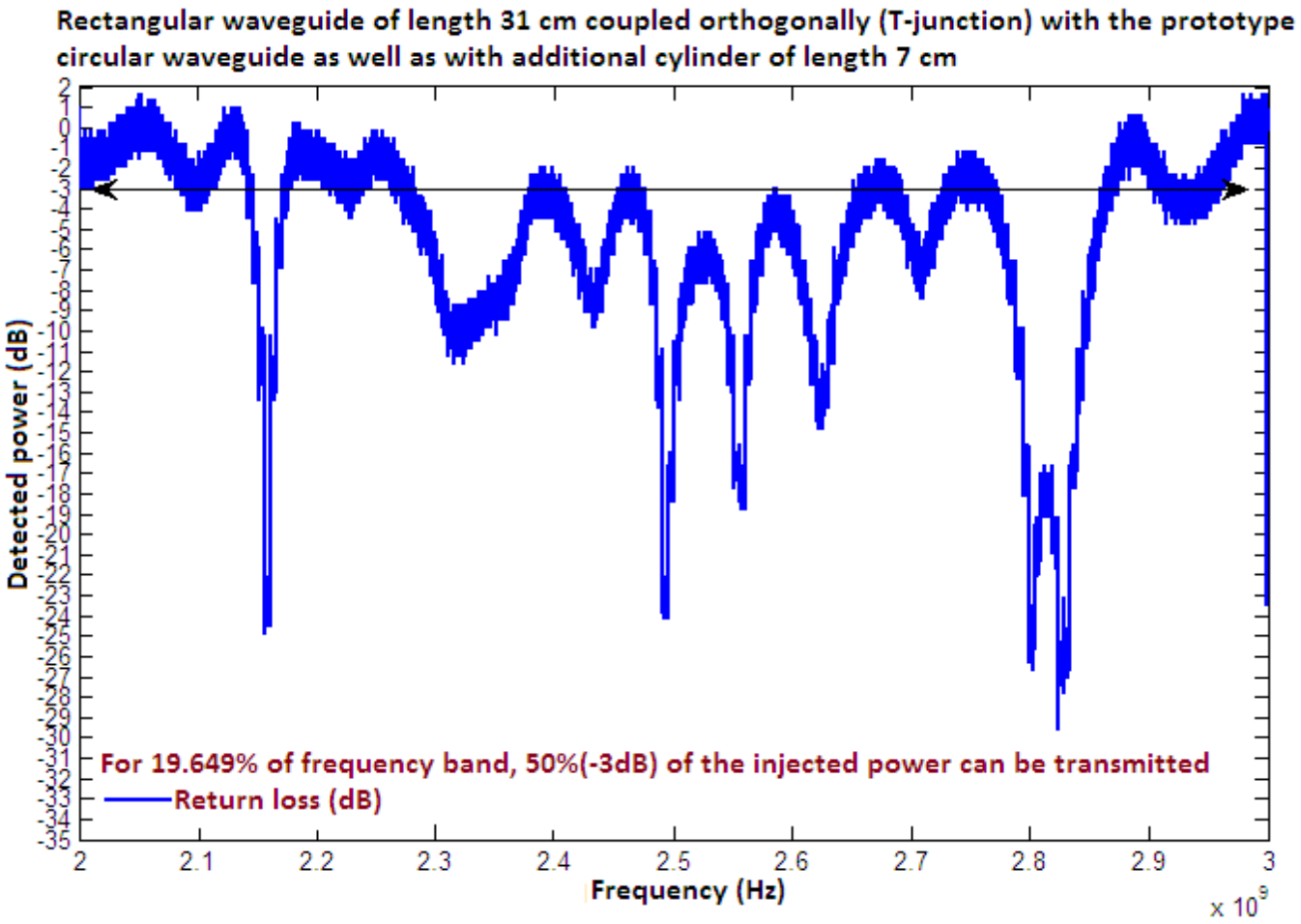

Figure 4.16 Return loss measurements of rectangular waveguide coupled with the circular waveguide and an additional cylinder

The additional cylinder reduces the efficiency of transmission and also complicates the return loss spectrum. When the rectangular waveguide is coupled with the circular waveguide, 22.474 % of the frequency band from 2 GHz to 3 GHz has a transmission of at least 50 %, and the maximum value of the transmission occurs at ≈-28 dB at a frequency of ≈ (2.8-2.9) GHz. When the additional cylinder is inserted, 19.649 % of the frequency band has a transmission of 50 % of the injected power and the maximum value of transmission occur at ≈ -27 dB at frequency of ≈ (2.8-2.9) GHz.
In the final configuration shown in figure 4.17 (a) and (b), the length of the rectangular waveguide is reduced from the optimum one (31 cm) to 7 cm, adjusted taking into account the geometrical constraints of the vacuum chamber of the ELTRAP apparatus. The position of the probe is tuned for a maximum field intensity at a distance of 2.28 cm from the end of the rectangular waveguide ("back-short").

The effect on transmission efficiency and return loss of the axial position of the T-junction between the rectangular (7 cm long) and the circular waveguide has been investigated inserting an additional cylinder of length 7 cm as shown in figure 4.17 (a) and (b). A RF signal swept between 2

GHz and 3 GHz at a power level of ±20.0 dBm is used like in the previous case. The transmitted (dBm) and reflected power (dBm) are reported in figures 4.18, 4.19 (scheme figure 4.17 (a)) and figure 4.21, 4.22 (scheme figure 4.17 (b)), respectively.

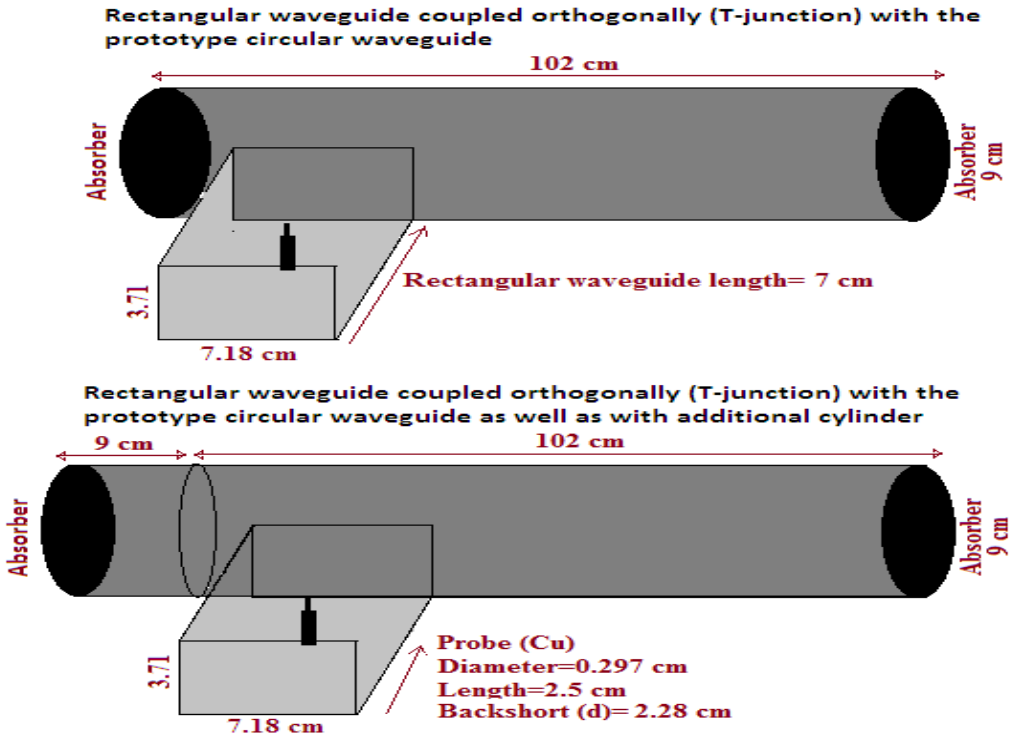

Figure 4.17 Arrangement of power flow measurements compatible with geometrical constraints of ELTRAP.

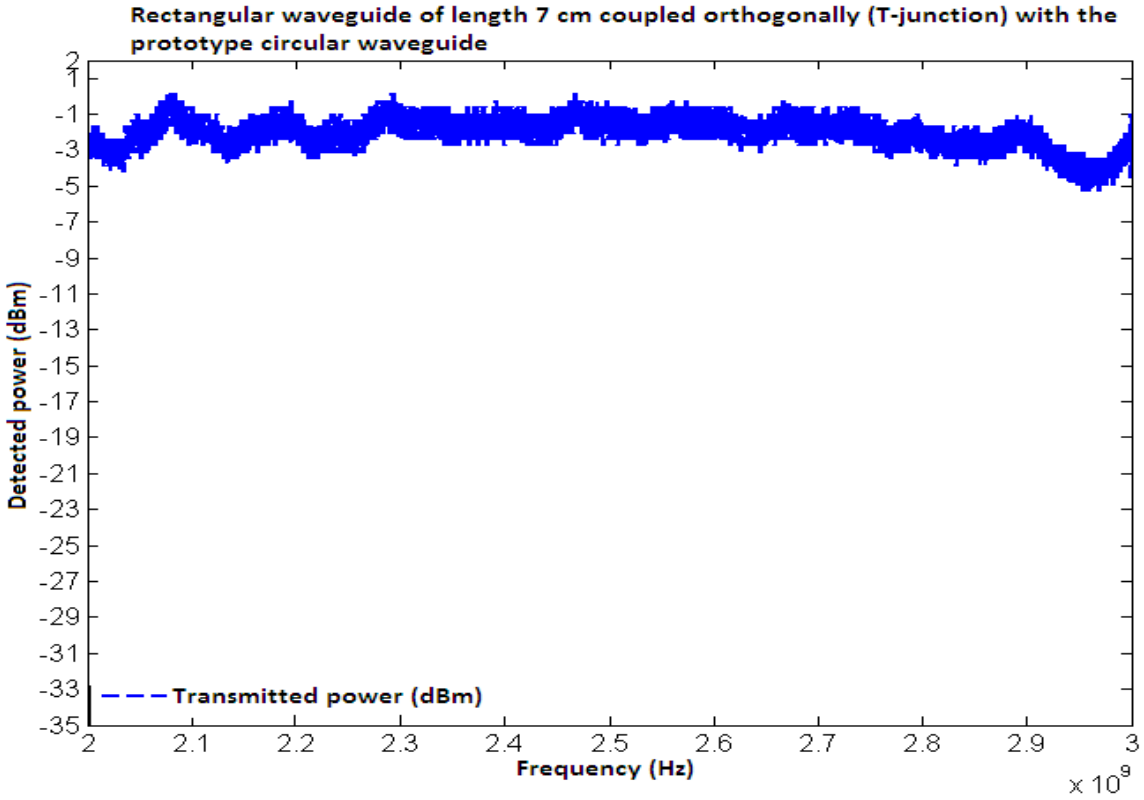

Figure 4.18 Transmitted power of rectangular waveguide compatible with geometrical constraints of ELTRAP coupled with the prototype circular waveguide.

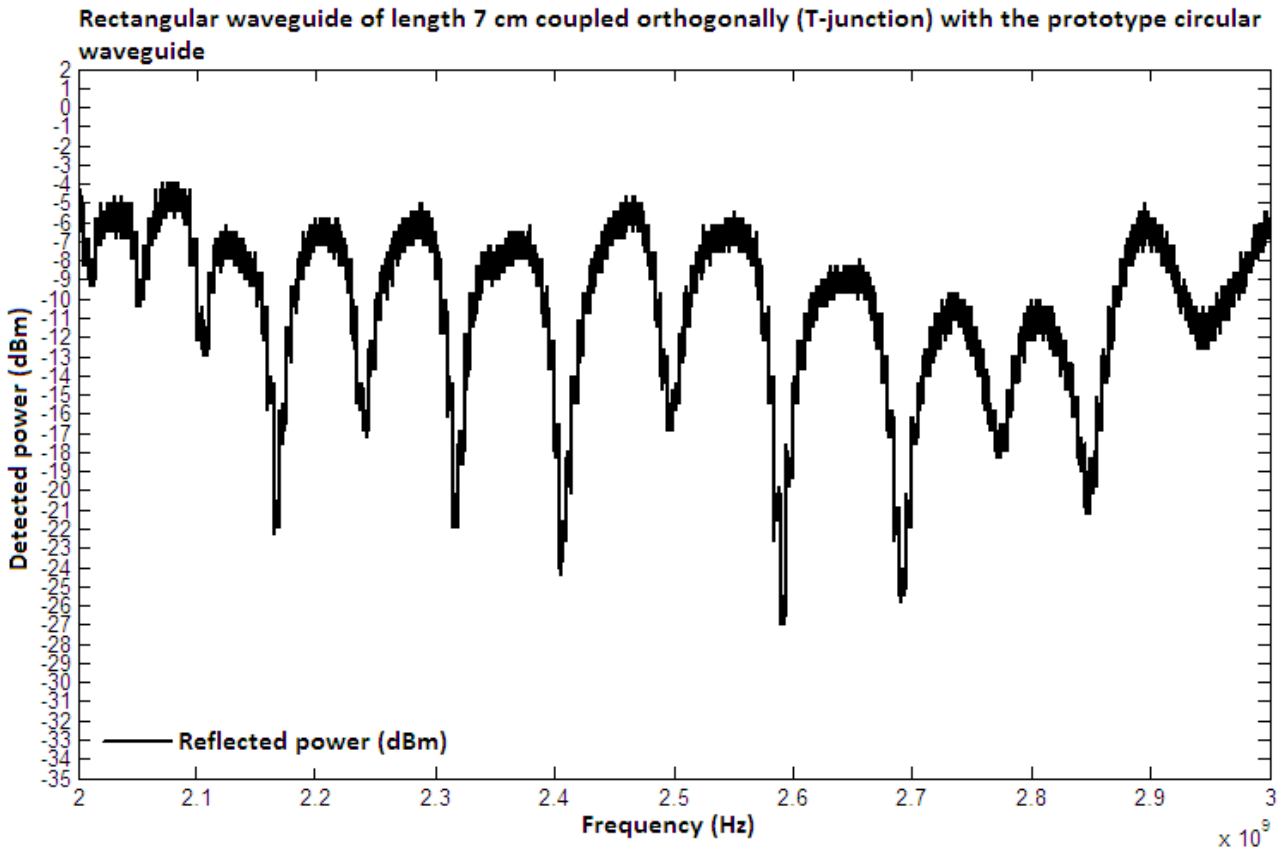

Figure 4.19 Reflected power of rectangular waveguide compatible with geometrical constraints of ELTRAP coupled with the prototype circular waveguide.

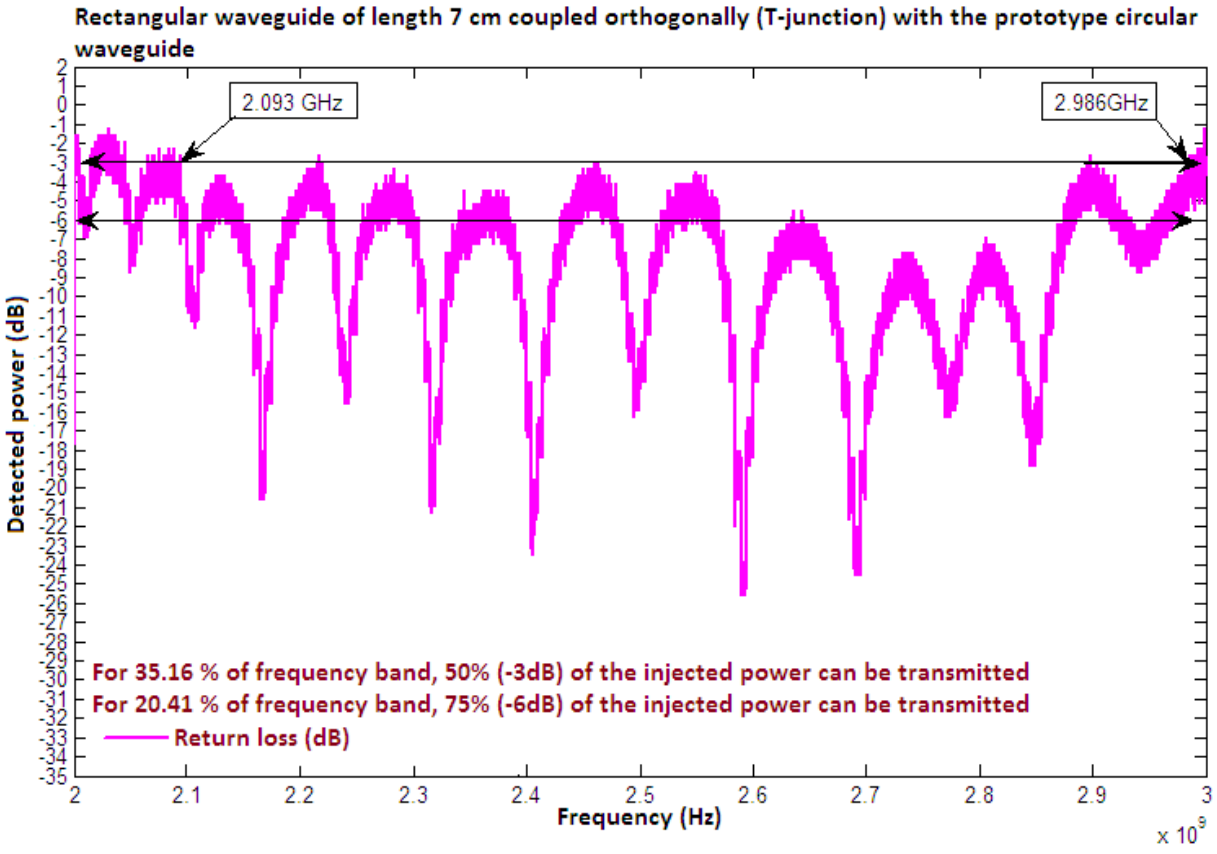

Figure 4.20 Return loss measurements of rectangular waveguide compatible with geometrical constraints of ELTRAP coupled with the prototype circular waveguide.

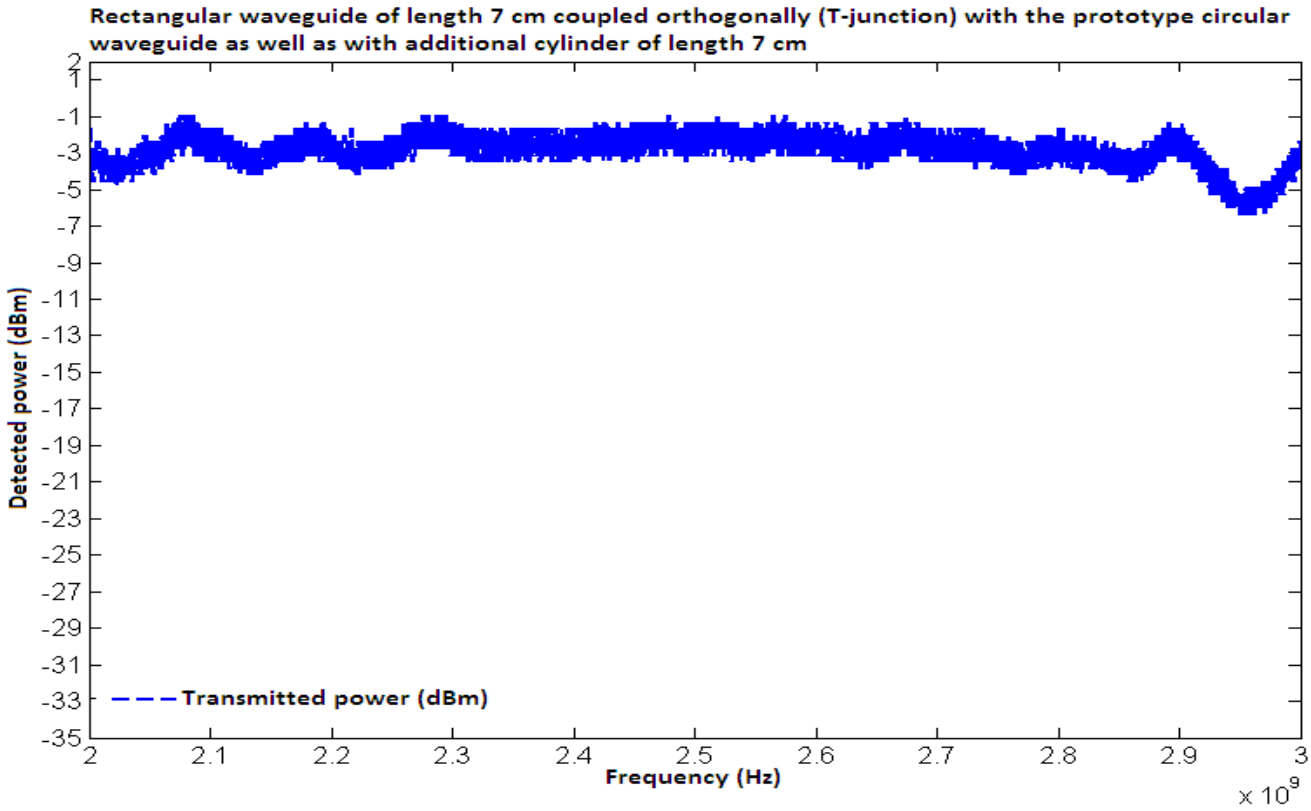

Figure 4.21 Transmitted power of rectangular waveguide compatible with geometrical constraints of ELTRAP coupled with the prototype circular waveguide and an additional cylinder.

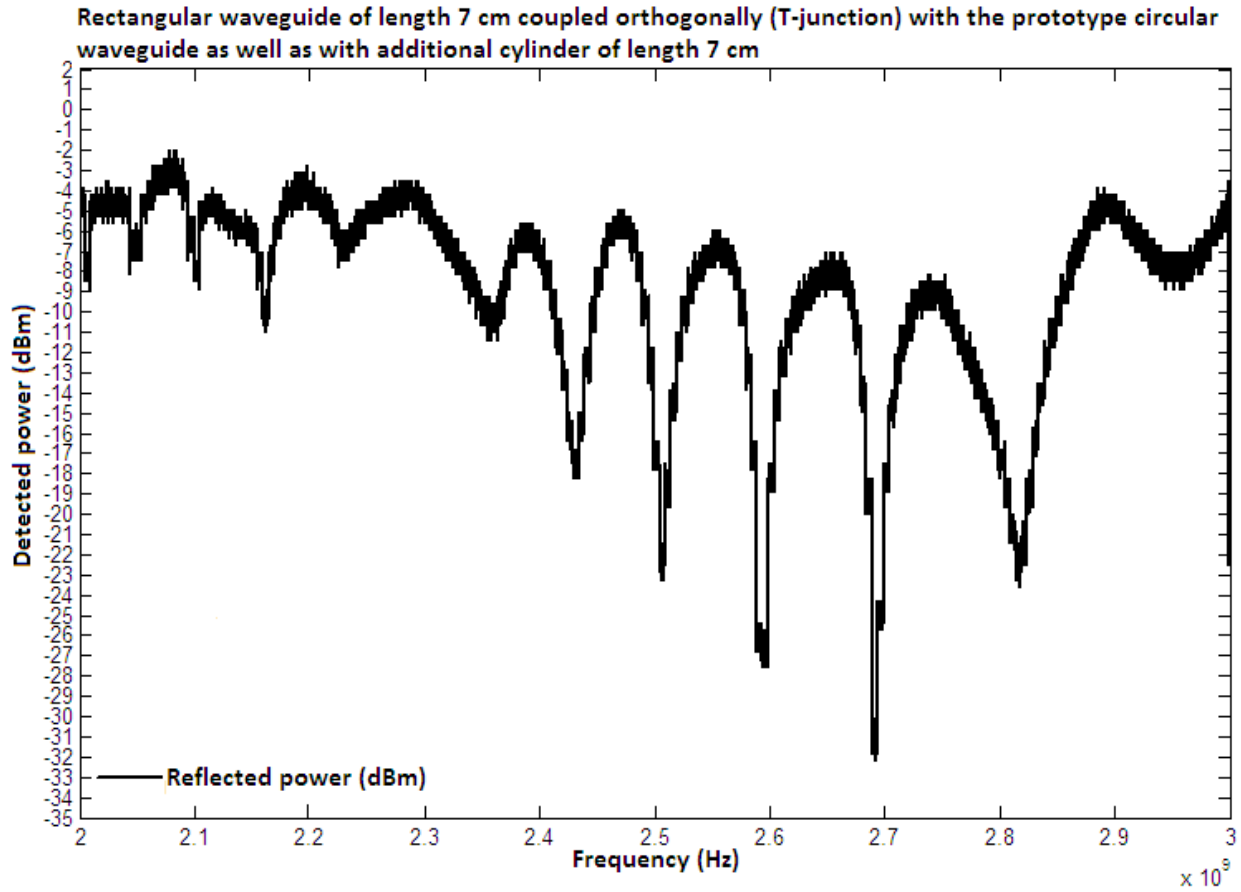

Figure 4.22 Reflected power of rectangular waveguide compatible with geometrical constraints of ELTRAP coupled with the prototype circular waveguide and an additional cylinder.

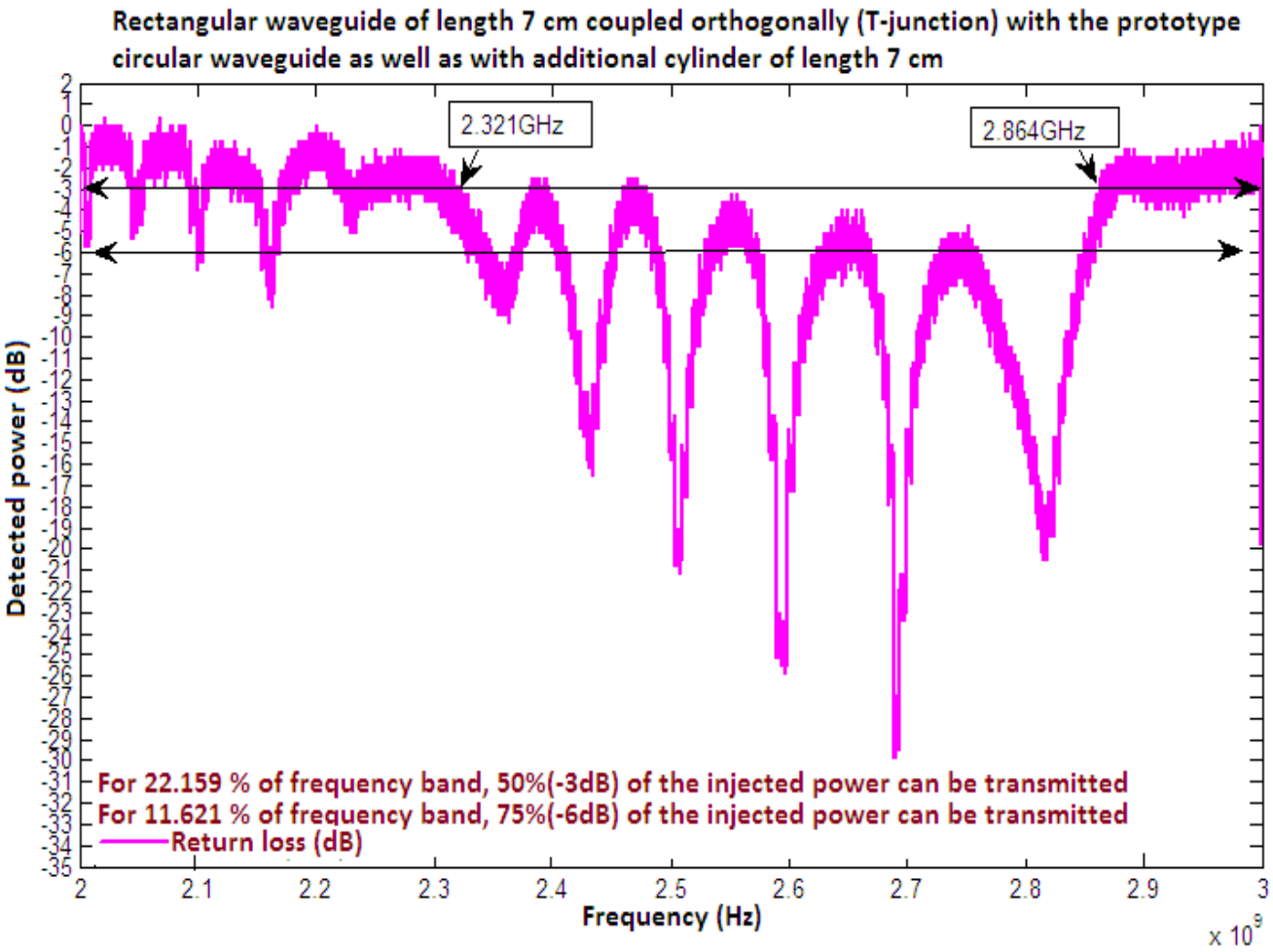

Figure 4.23 Return loss measurements of rectangular waveguide compatible with geometrical constraints of ELTRAP coupled with the prototype circular waveguide and an additional cylinder.

The return loss measurements of the final configuration presented in figures 4.20 and 4.23 (combined in figure 4.24) indicate that a frequency band of 35% is obtained at -3 dB at about 2.6 GHz and a frequency band of 20.4 % at -6dB at about 2.7GHz. By introducing an additional length (cylinder of length 9 cm) to the prototype circular waveguide, the frequency band reduces to 22.16% at -3dB at about 2.5 GHz and to 11.62% at -6dB at about 2.6GHz as shown in figure 4.24.

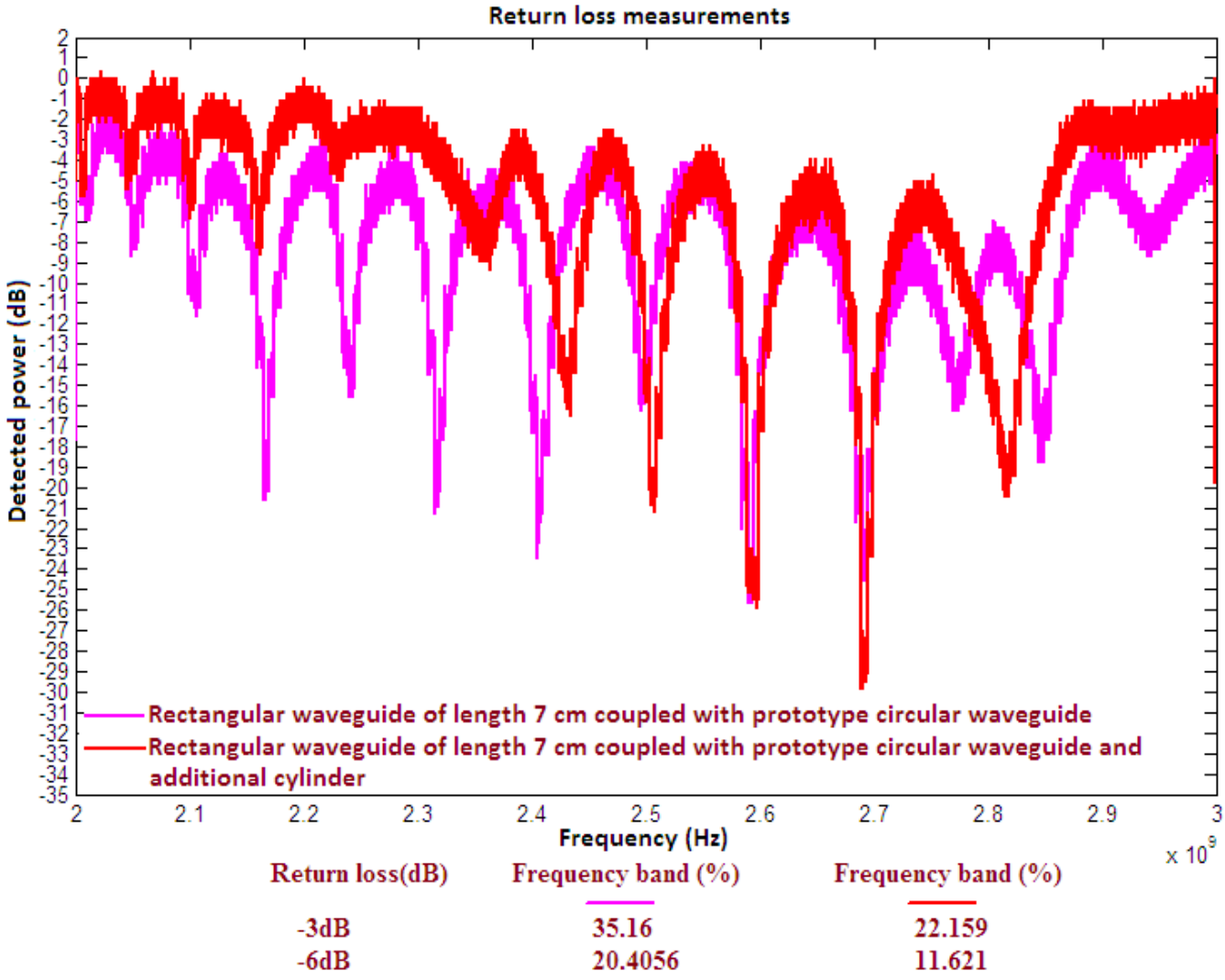

Figure 4.24 Return loss measurements of rectangular waveguide compatible with geometrical constraints of ELTRAP coupled with 1). Prototype circular waveguide, 2). Prototype circular waveguide and additional cylinder (combine plot of figure 4.20 and 4.23).

In summary, with the optimum design of the rectangular waveguide (>2λg=31 cm) the maximum value of the transmission occurs close to 3 GHz. When the rectangular waveguide (both with the optimum length and with a length of 7 cm) is coupled with the prototype circular waveguide, the maximum transmission efficiency reduces and shifts away from the maximum operating frequency of the available RF generator. When an additional length of the circular waveguide is inserted, the useful frequency band is also reduced.

Chapter FIVE

Numerical simulations of the RF heating of a non-neutral plasma in a Penning-Malmberg trap

5.1 Introduction

The Particle-In-Cell (PIC) method is one of the most popular scheme to describe numerically the dynamics of a plasma. PIC methods have been in use since 1955 [20], even before the first FORTRAN compilers were available. The technique was initially proposed by Dawson [21] (at Princeton) and Oscar Buneman [22-25] (at Cambridge) and later developed by Birdsall and Langdon [26-27] at Berkeley.

The PIC simulations presented here have been performed using the object-oriented code "OOPIC Pro". The code is built on the "OOPIC" code physics kernel, which was originally developed at the University of California at Berkeley in 1995 by members of the plasma theory and simulation group (PTSG). The OOPIC physics kernel has been used by researchers around the world since 1995 to simulate a wide range of challenging problems. These include plasma display panels, ion implantation, high-power microwave devices, and next-generation particle accelerator concepts. The code is open source and well documented, and user corrections and improvements are incorporated regularly (see https://ice.txcorp.com/mailman/listinfo/oopic-users).

The OOPIC code was chosen among the various PIC codes in use because of its reliability and freely availability and the possibility to run it on even low cost desktop computers. The code is two dimensional in configuration space and three dimensional in velocity space. The code includes electrostatic and electromagnetic field solvers, and supports both cylindrical (z, r) and Cartesian (x, y) geometry. The charge and current densities as well as the fields are calculated on an orthogonal, potentially non-uniform grid. The dynamics of the particles may be either relativistic or non-relativistic. Furthermore, the code may take into account RF heating phenomena, ionization, excitation and Monte Carlo collisions (MCC) with a variety of background gases (H, He, Ar, Ne, N, Xe, and Li).

The RF electron heating in ELTRAP under conditions of ultra-high vacuum has been simulated with OOPIC Pro, using the cylindrical geometry (z, r). The results obtained from the simulations show very good agreement with the experiments conducted in ELTRAP at low drive frequencies (1-20 MHz). In the simulations, a realistic geometry of the apparatus is used, with a length of the electrode stack of 102 cm, and an internal radius of the conducting cylinders of 4.5 cm. The electrostatic simulations of the electron heating have been performed for different RF drive excitation frequencies (1-15 MHz) with an amplitude of 5 and 10 V and for different electron densities, $5\times10^{7}\,m^{-3}$ and $10^{12}\,m^{-3}$ respectively. The RF signal is directly imposed on a trap electrode at two different axial positions, i.e. to cylinder C5 in the interval (0.408-0.51) m and cylinder C7 in the interval (0.612-0.714) m on the electrode stack.

It is observed that with a continuous RF excitation the electron heating is initially higher near the wall of the cylinder and then it is extended to the whole space. It is also noticed that the temperature of the confined electrons is higher when the RF is applied at one end of the electrode stack, e.g. on cylinder C7, of the confinement cylinder as compared to the middle part, e.g. on cylinder C5, as observed also experimentally.

Simulations with a residual hydrogen gas have been also performed (at pressures 10^{-8} torr, 10^{-7} torr and 10^{-6} torr). In addition, electromagnetic simulations of the electron cyclotron resonance heating (ECRH) have also been considered, using an RF drive of 2.8 GHz, to describe the electron heating with the microwave system which is going to be installed in ELTRAP (see previous chapter).

5.2 OOPIC simulation set-up

The simulation parameters have been chosen according to the geometry of the ELTRAP device and the other data used in the RF electron plasma generation experiments described earlier. These parameters correspond to trap size, external homogeneous magnetic field for the radial confinement, static electrostatic potentials for axial confinement, RF drive parameters, initial electron density and temperature, etc.

The simulation parameters are incorporated inside the input file of the code, which is written as a series of text blocks (grid block, control block, load block, etc.), see figure 5.1. The grid block is

used to specify the size, shape, geometry and other characteristics of the numerical grid. When the flag Geometry is set to 0, the code uses a cylindrical coordinate system where x1 corresponds to z, x2 corresponds to r, and x3 corresponds to the ignorable azimuthal ϕ coordinate. The lower and upper z (axial) coordinates x1s = 0.00 and x1f = 1.02 m correspond to the total length of the ELTRAP electrode stack, and the lower and upper radial coordinates x2s = 0.00 and x2f = 0.045 m correspond to the internal radial range of the electrodes (wall radius = 4.5 cm). The number of grid points in the axial and radial direction has been chosen as J=180 and K=45, respectively.

The control block also contains the value of the external homogenous static magnetic (B01 = 0.1 T), and the simulation time step in seconds. The ElectrostaticFlag parameter in control block allows the user to select either electrostatic or electromagnetic simulation.

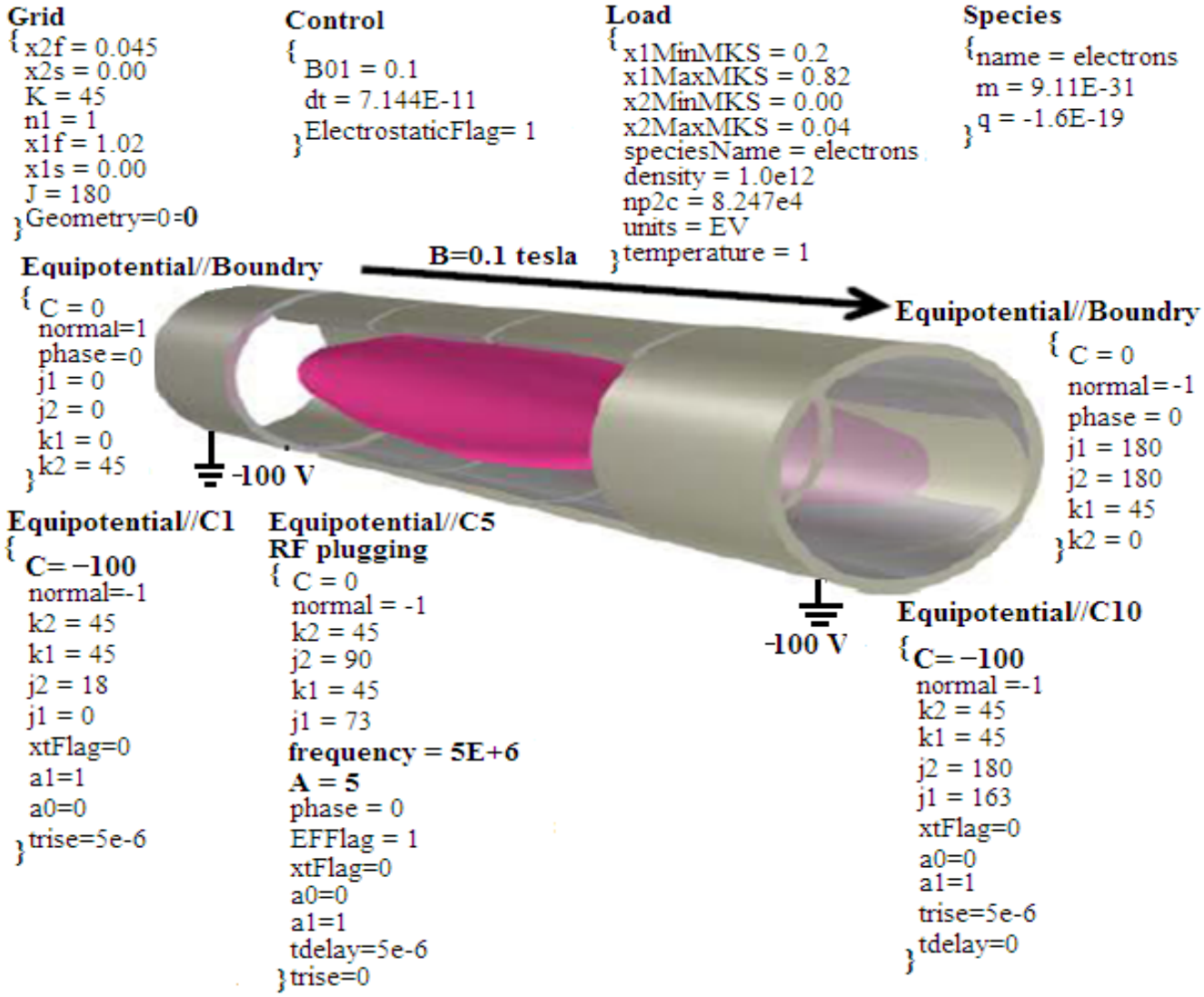

Figure 5.1 Simulation setup and input file structure of the PIC code.

In the load block, the region where the plasma is initially located, the species (e.g. electrons), the density and the temperature are defined. A Maxwellian velocity distributions for each particle

species is considered. The number (np2c) of real particles per simulated particle (so-called "super-particle" or "macro-particle") is also defined in this block. In simulations that model multiple types of particles (for example, electrons and ions), there will be more than one species block within the input file.

The potentials on each of the 10 cylindrical electrodes is also specified in the input file. Typically, on the end cylinders (C1 and C10) a potential of -100 V has been considered, while all other cylinders are kept at ground, except the one on which the RF drive is applied (see figure 5.1). The number of cells (grid points) distributions along axial (z-axis) and radial (r-axis) direction of the electrode stack is indicated in figure 5.2. In each of the 10 cylinders there are 45 cells in the radial direction and 18 cells along the z-axis.

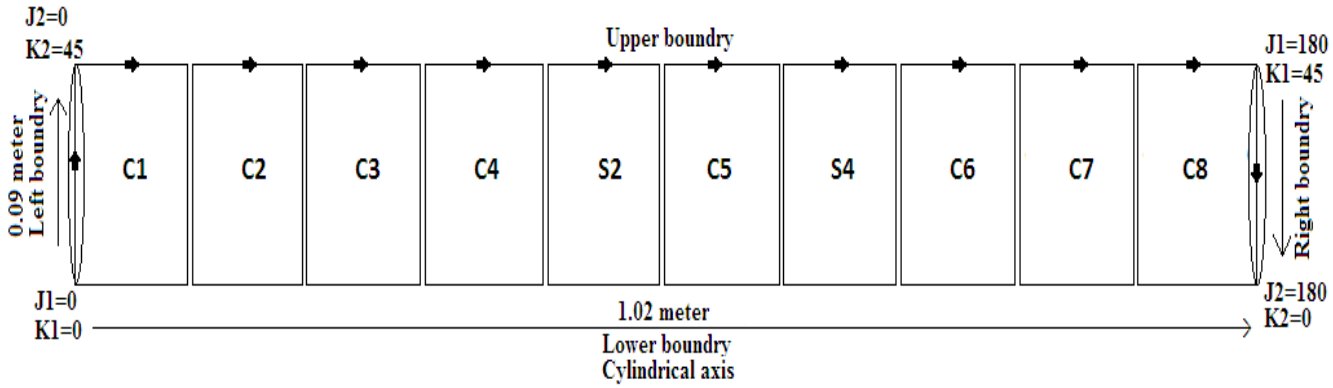

Figure 5.2 Cell distributions of the electrode stack (10 cylinders) in the simulation domain of the PIC code.

5.3 Electrostatic vs electromagnetic simulations

In the PIC simulations the fields (E, B) are defined on the discrete grid. The position and velocity of each (macro-particle) vary according to the equation of motion

$$m\frac{dv}{dt} = (qE)_{electric} + q(v \times B)_{magnetic} \qquad 5.1$$

The dynamics of the charged particles is determined by the applied and the self-consistent fields. The fields are calculated from Maxwell's equations by knowing the positions and velocities of all the particles. The sequence of operations described in figure 5.3 is repeated for several time steps. In the electrostatic simulations, the electric field is computed as $E = -\nabla\phi$, where the electrostatic potential 'ϕ' is obtained from the Poisson equation,

$$\nabla^2 \phi = -\frac{\rho}{\varepsilon_0} \qquad 5.2$$

where 'ρ' is the charge density, computed on the grid by splitting the charge of the particles to the nearest grid points e.g. by linear interpolation. In the electrostatic approximation, the magnetic field is externally applied and is not re-calculated at each time step.

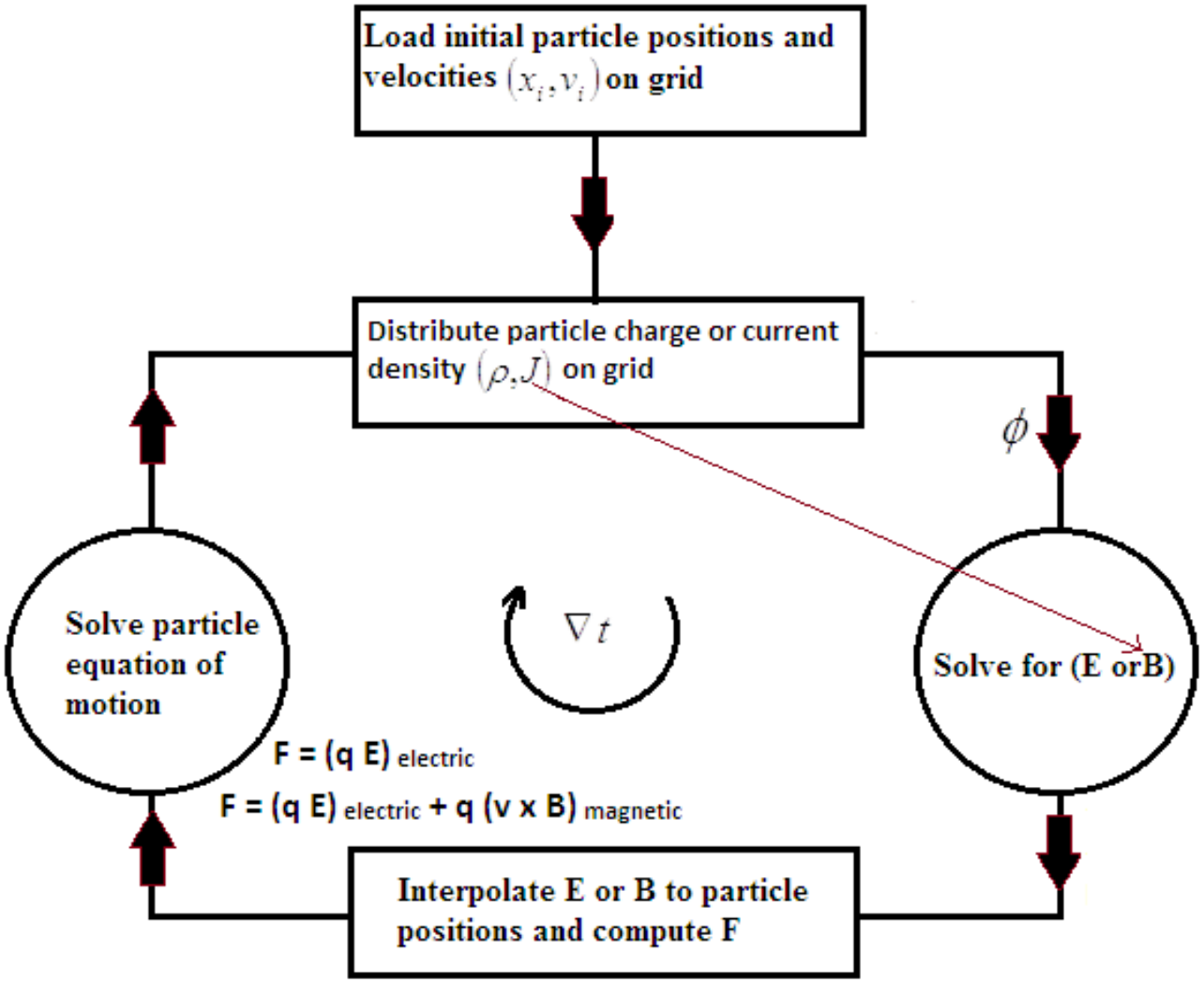

Figure 5.3 PIC scheme for electrostatic and electromagnetic simulations

In the electromagnetic simulations, the complete set of Maxwell's equations is solved to obtain both the electric and magnetic field

$$\nabla \cdot E = \frac{\rho}{\varepsilon_0}, \qquad \nabla.\mathrm{B} = 0 \tag{5.3}$$

$$\nabla \times E = -\frac{\partial B}{\partial t}, \quad \nabla \times \mathrm{B} = \mu_0 j + \frac{1}{c^2}\frac{\partial E}{\partial t} \tag{5.4}$$

where the current density is used to compute the self-consistent contribution to the magnetic field. The positions and velocities of the particles are used to calculate the source terms (ρ, J), which are interpolated to the grid. From the fields, the Lorentz force is calculated and interpolated back to the positions of the particles. The forces due to the electric and magnetic fields (self-consistent fields) are used to advance the velocities of the particles, and subsequently the velocity is used to advance the position.

5.3.1 Time step and cell size

The appropriate values for grid size, time step, etc. depend on the scenario being simulated and the computational power available. As the cells increase in size, the error in the simulation becomes greater because the fields are calculated at a greater distances from the affected particles and small-scale variations are lost. Similarly, the larger the time step, the further the particles move without interaction before the field effect is recalculated, thus also increasing the error. In addition, the number of particles used in the simulation affects the accuracy of the simulation. The reduction of the number of particles in the simulation decreases the simulation time approximately linearly, but with too few particles the individual starting locations determined by the initial random distributions become too significant to the outcome of the simulation. Hence, the selection of these parameters is done with great care to obtain a balance between accuracy and performance.

The time step needs to be small enough so that the fastest particles do not cross more that one cell per time step. It should be smaller than the smallest time scale, i.e. the cyclotron period or the plasma period. The time step to be used in the simulation must be within the limits set by the Courant condition, which states that the time sampling, dt, must be sufficiently small so that the

longest wavelength, propagating at the highest velocity, does not outrun the spatial grid sampling dx.

Table 5.1 Particle in cell (PIC) simulation parameters

Parameters	$5x10^7$ m^{-3} Temperature 0.01 eV	10^{12} m^{-3} Temperature 1 eV	Unit
Debye length	0.1051	0.00743	meter
Electron Larmor radius	3.372×10^{-6}	3.372×10^{-5}	meter
Bouncing time	3.888×10^{-5}	3.888×10^{-6}	second
Plasma frequency	6.3498×10^{4}	8.98×10^{6}	Hertz
J	180	180	cell
K	45	45	cell
np2c	8	8.247×10^{4}	particle
Time step (dt)	7.144×10^{-11}	7.144×10^{-11}	second
Cell size (dx1, dx2)	0.00566, 0.001	0.00566, 0.001	meter
duration	10^{-4}	10^{-4}	second
Simulation Domain	0.2 to 0.82	0.2 to 0.82	meter

5.4 Electrostatic PIC simulations

Experimentally, plasma generation has been detected in a cylindrical Penning–Malmberg trap in the ultra-high vacuum pressure regime for a large bandwidth of low-power radio frequency (RF) excitations (0.1–20MHz) as discussed in chapter 3. For the PIC simulations, electron plasmas of about $\approx 6.5 \times 10^9$ electrons, with trapped density ranging from 5 x 10^7 m^{-3} to 10^{12} m^{-3}, temperature from 0.01 eV to 1 eV have been considered. The parameters in table 5.1 have been selected for the reasons discussed above, and are appropriate for most of the simulations done for

an applied magnetic field of 0.1 T, corresponding to a cyclotron period of 3.57239×10^{-10} sec (2.799 GHz).

The simulation time step has been selected as $dt = \frac{cyclotron \quad \text{period}}{5} = 7.144 \times 10^{-11} s$. The number of real particles per simulation particles (np2c) is calculated by $n_e V / p_{pc} \times k \times J$, where $n_e, V, p_{pc}, \text{k, and J}$ are trapped electron density, simulation volume (domain), particles per cell $\approx 4-9$, number of z-cells and number of k-cells respectively.

5.5 Simulations of RF heating at low electron plasma density

The RF electron heating has been evaluated using three different simulation schemes (see schematic diagram 5.4). Here no background gas is considered and in each simulation scheme, the confinement length between electrodes C1 and C10 is kept constant. The time step has been set at 7.144×10^{-11} second and the simulation is run up to 100 μs and the data saved into 22 dump files (each dump 5 μs).

The frequencies of 1 MHz, 5 MHz, 6 MHz, 8 MHz, 10 MHz and 15 MHz and amplitude 5 volts and 10 volts have been considered at low electron density $n_e = 5\times10^7 m^{-3}$ but two different electrodes C5 in the interval (0.408-0.51) m and cylinder C7 in the interval (0.612-0.714) m are used as antenna for the RF excitation. The numerical weight of the macro-particles is $np2c = 8$. The confined electrons population can be separated into a 'fast' and a 'slow' component on the basis of the ratio between the electron kinetic energy and the first ionization energy of the residual neutral components, i.e. mainly H_2. The ionization threshold is between 10 and 20 eV and the peak of the ionization cross section approximately lies in the 70–100 eV range. Therefore, the electrons must reach an energy of some tens of electron volts ($V = 1.327\times10^6 m/s$) to build up and sustain a plasma. This is the reason the energy (eV) range of the confined electrons have been categorized as (0-20) eV, (20-70) eV, (70-100) eV and ≥ 100 eV in table 5.2, table 5.3, table 5.4 and table 5.5.

The confined electrons experience a change of energy after each interaction with the RF barrier. A net energy gain is seen in figures 5.5-5.8. The legend in each plot specifies the RF excitations

frequency. The axial kinetic energy is in general increasing for all considered cases, and tends to saturate after 50 μs approximately. Of course, higher temperature increments are obtained by increasing the amplitude of the RF excitation.

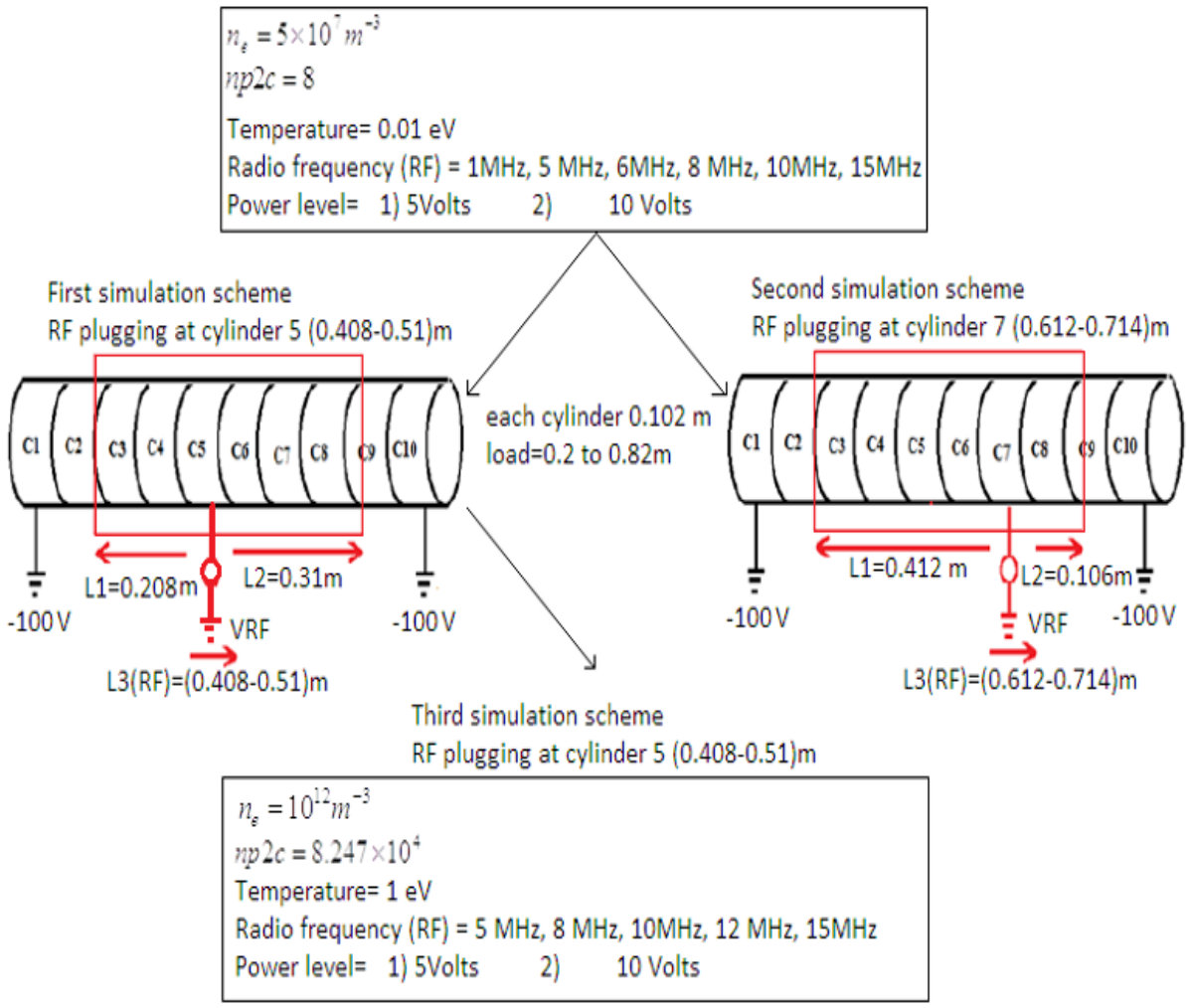

Figure 5.4 Schematic diagram of electrostatic PIC simulations of an electron plasma formed and confined between C1 and C10 biased at a negative voltage -100 V and RF drive of amplitude A=5 V and 10 V applied on 1) C5 and C7 at $5\times10^7 m^{-3}$ 2) and C5 at $10^{12} m^{-3}$.

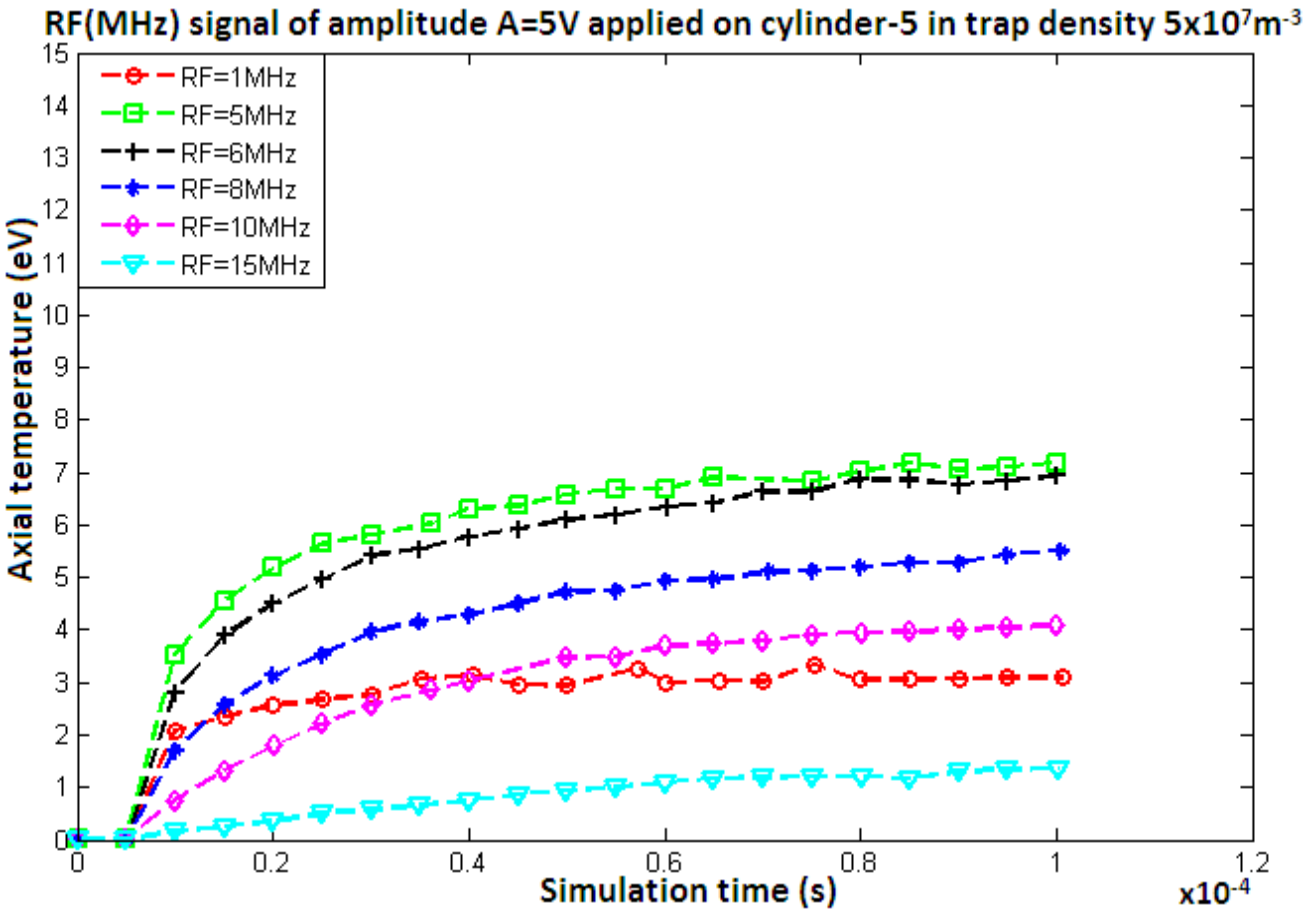

Figure 5.5 Axial temperature vs time for an electron plasma density $5\times10^{7}\,m^{-3}$ and an RF drive of amplitude A=5 V applied on Cylinder-5 (First simulation scheme mentioned in figure 4.4).

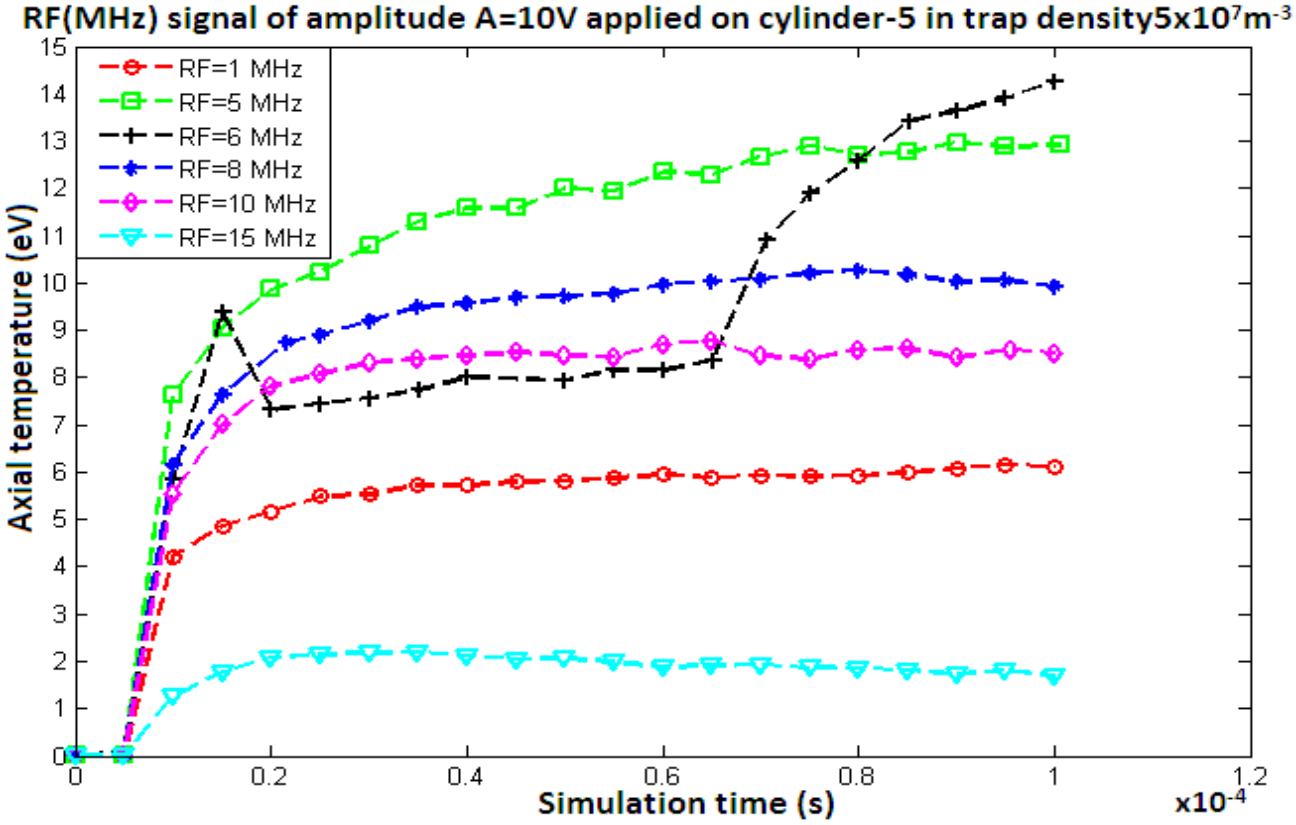

Figure 5.6 Axial temperature vs time for an electron plasma density $5\times10^{7}\,m^{-3}$ and an RF drive of amplitude A=10 V applied on Cylinder-5 (First simulation scheme mentioned in figure 4.4).

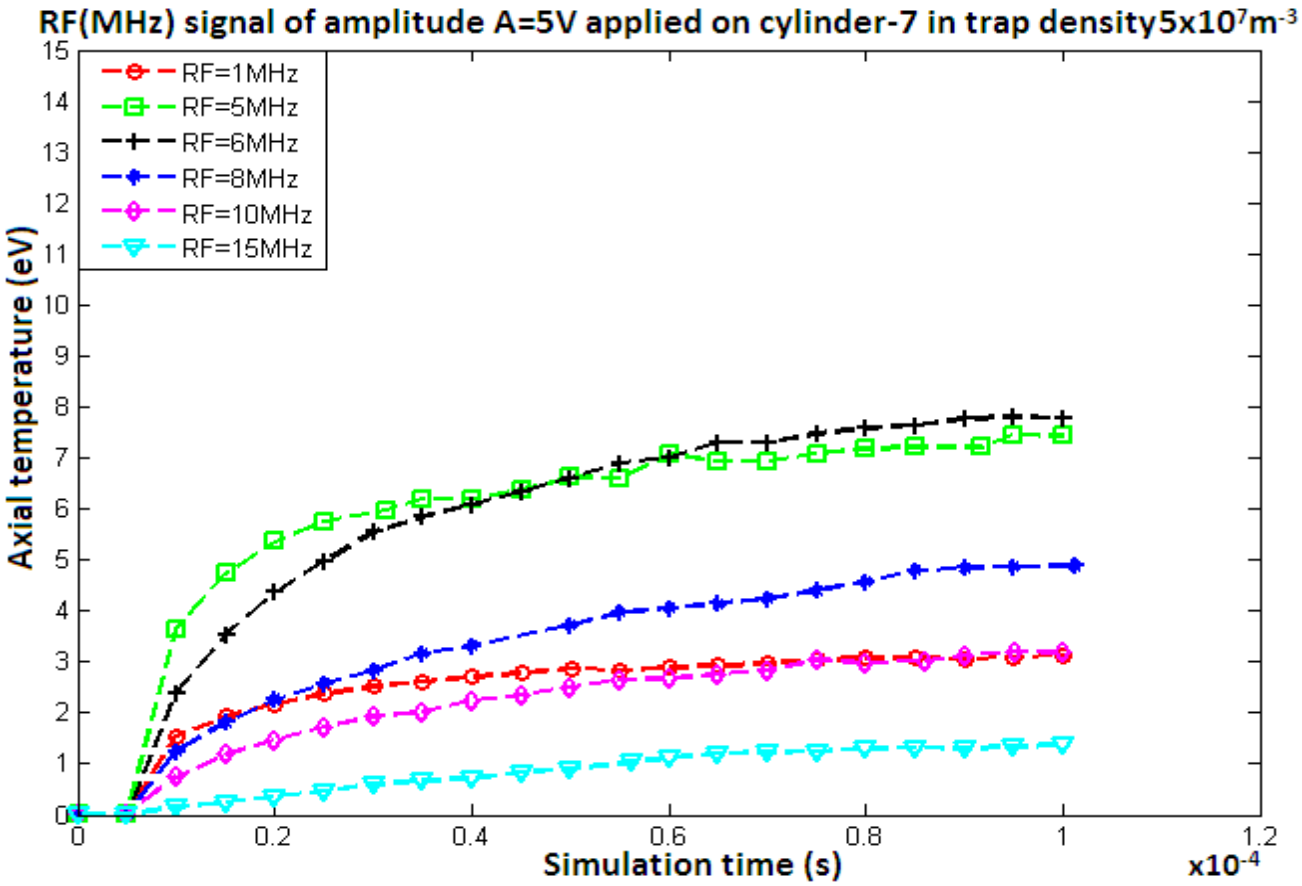

Figure 5.7 Axial temperature vs time for an electron plasma density $5\times10^{7}\,m^{-3}$ and an RF drive of amplitude A = 5 V applied on C7 (2nd simulation scheme mentioned in figure 4.4).

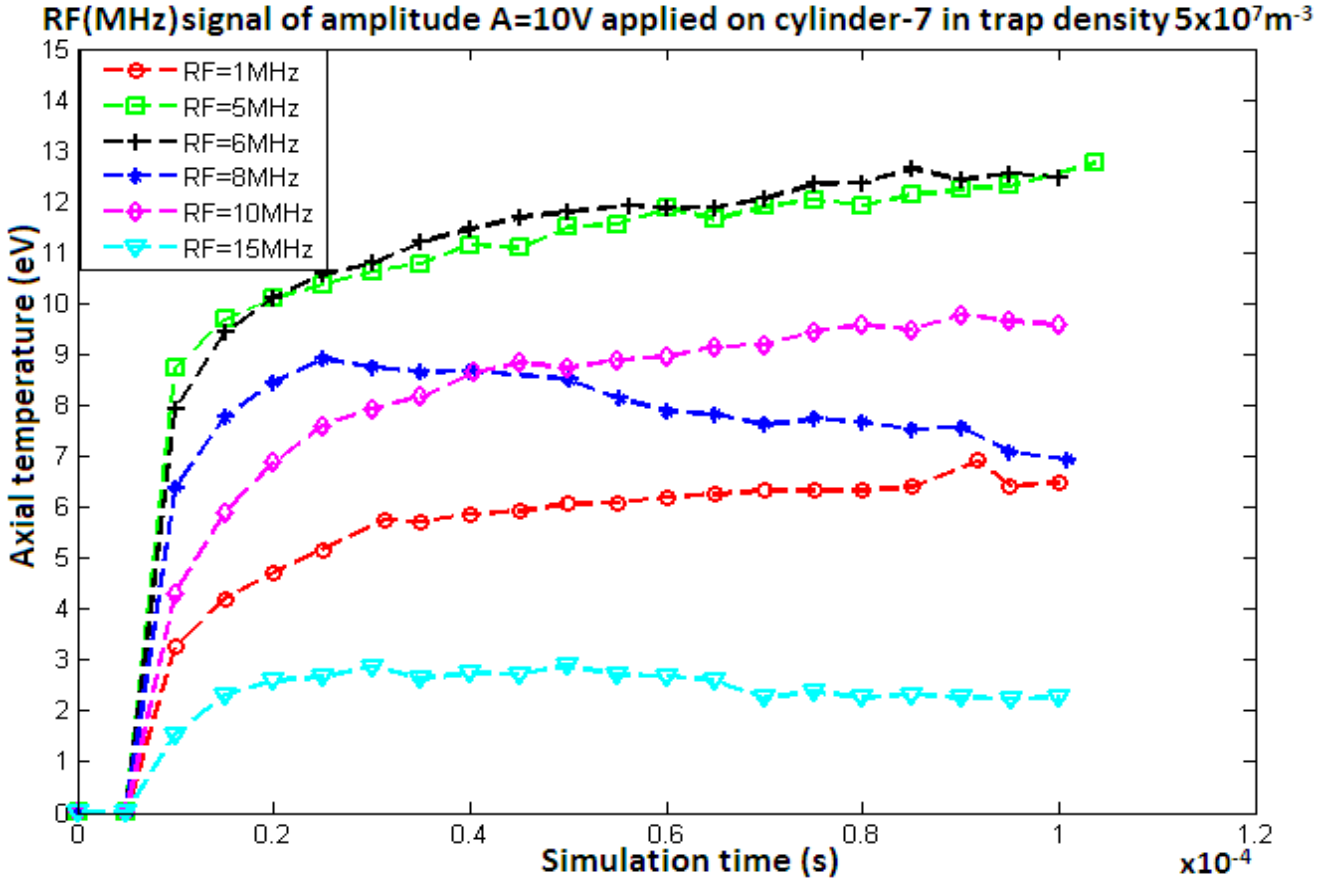

Figure 5.8 Axial temperature vs time for an electron plasma density $5\times10^{7}\,m^{-3}$ and an RF drive of amplitude A = 10 V applied on C7 (2nd simulation scheme mentioned in figure 4.4).

At the end of the simulation time of $100\mu s$, the axial temperature of the confined electrons is found to increase with an increase of the applied excitation frequency from 1 MHz to 5 or 6 MHz, while it decreases with a further increase of excitation frequency (8 MHz, 10 MHz and 15 MHz). Second, it is also observed that the final temperature is higher for the choice of the C7 electrode as RF antenna as compared to electrode C5, which is closer to the center of the trap.

It is confirmed the experimental finding that the RF heating is more effective in the outer radial part of the trap cylinder (see also tables 5.2-5.5).

The simulation results of the axial energy profile of RF heating indicates that the heating is higher near to the wall of cylinder up to $50\mu s$, then the effect is extended toward the central region of the trap (see figures 5.9-5.12). The axial and radial losses the electrons for a 5V excitation amplitude is negligibly small for all the considered frequencies (1-15 MHz): the loss percentage is only 0.082 % for 8 MHz on C7 and 0.072 % for 15 MHz on C5. However, for a 10 V amplitude the losses increase above 6 MHz excitation frequency. The maximum loss percentages are 14.909 % for 8 MHz (C7 used as antenna), 2.92 % losses for 8 MHz (C5 used as antenna), 5.252 % for 10 MHz (C5 used as antenna), 0.832 % for 10 MHz (C7 used as antenna), 4.025 % for 15 MHz (C5 used as antenna) and 3.322 % for 15 MHz (C7 used as antenna). These losses of electrons at higher frequencies (≥ 8MHz) tens to reduce the temperature of confined electron plasma. However, at higher excitation frequency (5 to 15MHz) and amplitude (5-10 V) only 1.263 % to 15.3 % of confined electrons have an energy range between 20 and 70 eV and only 0.005 % to 0.64 % between 70 and 100 eV (see tables 5.2-5.5).

Table 5.2. Energy (eV) range of the electrons at simulation time 100 µs, for a density $5\times10^{7}\,m^{-3}$ and an amplitude A = 5 V of the RF drive applied on electrode C5.

Energy range (eV)	Number of electrons(%) of $KE(u_z)$	Number of electrons(%) of $KE(u_r)$	Number of electrons(%) of $KE(u_{phi})$	Number of electrons(%) of $KE(u_z)$	Number of electrons(%) of $KE(u_r)$	Number of electrons(%) of $KE(u_{phi})$
	RF 1MHz of amplitude A=5 V			**RF 5MHz of amplitude A=5 V**		
0-20 eV	19478 (100%)	19478 (100%)	19478 (100%)	18399 (94.46%)	19478 (100%)	19478 (100%)
20-70 eV	0 (0%)	0 (0%)	0 (0%)	1079 (5.54%)	0 (0%)	0 (0%)
70-100 eV	0 (0%)	0 (0%)	0 (0%)	0 (0%)	0 (0%)	0 (0%)
≥100 eV	0 (0%)	0 (0%)	0 (0%)	0 (0%)	0 (0%)	0 (0%)
Total (No,%)	19478 (100%)	19478 (100%)	19478 (100%)	19478 (100%)	19478 (100%)	19478 (100%)
E (eV)	**RF 6MHz of amplitude A=5 V**			**RF 8MHz of amplitude A=5 V**		
0-20 eV	18194 (93.41%)	19478 (100%)	19478 (100%)	18378 (94.353%)	19478 (100%)	19478 (100%)
20-70 eV	1284 (6.59%)	0 (0%)	0 (0%)	1100 (5.65%)	0 (0%)	0 (0%)
70-100 eV	0 (0%)	0 (0%)	0 (0%)	0 (0%)	0 (0%)	0 (0%)
≥100 eV	0 (0%)	0 (0%)	0 (0%)	0 (0%)	0 (0%)	0 (0%)
Total (No,%)	19478 (100%)	19478 (100%)	19478 (100%)	19478 (100%)	19478 (100%)	19478 (100%)
E(eV)	**RF 10MHz of amplitude A=5 V**			**RF 15MHz of amplitude A=5 V**		
0-20 eV	18661 (95.81%)	19478 (100%)	19478 (100%)	19228 (98.72%)	19464 (99.92%)	19464 (99.92%)
20-70 eV	816 (4.19%)	0 (0%)	0 (0%)	221 (1.13%)	0 (0%)	0 (0%)
70-100 eV	01 (0.005%)	0 (0%)	0 (0%)	15 (0.077%)	0 (0%)	0 (0%)
≥100 eV	0 (0%)	0 (0%)	0 (0%)	0 (0%)	0 (0%)	0 (0%)
Total (No,%)	19478 (100%)	19478 (100%)	19478 (100%)	19464 (99.928%)	19464 (99.928%)	19464 (99.928%)

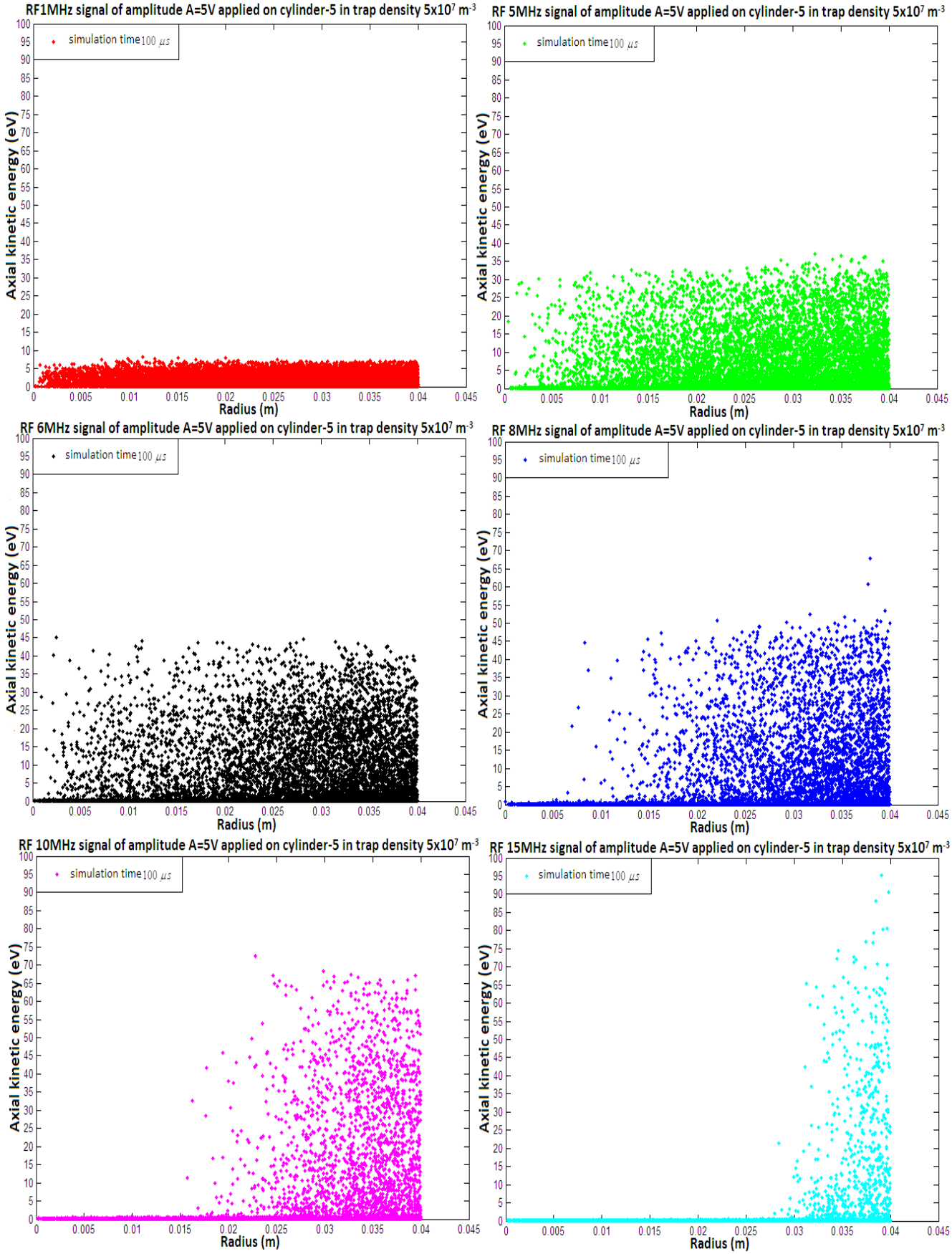

Figure 5.9 The electrostatic PIC simulation of axial kinetic energy (eV) (electrons velocities in the axial (z) direction) of electron plasma $5\times10^{7}m^{-3}$ as a function of radial position. The confined electrons is between C1 and C8 biased at a negative voltage -100 V and RF (MHz) drive of amplitude A=5 V applied on Cylinder-5 (1st simulation scheme mentioned in figure 4.4).

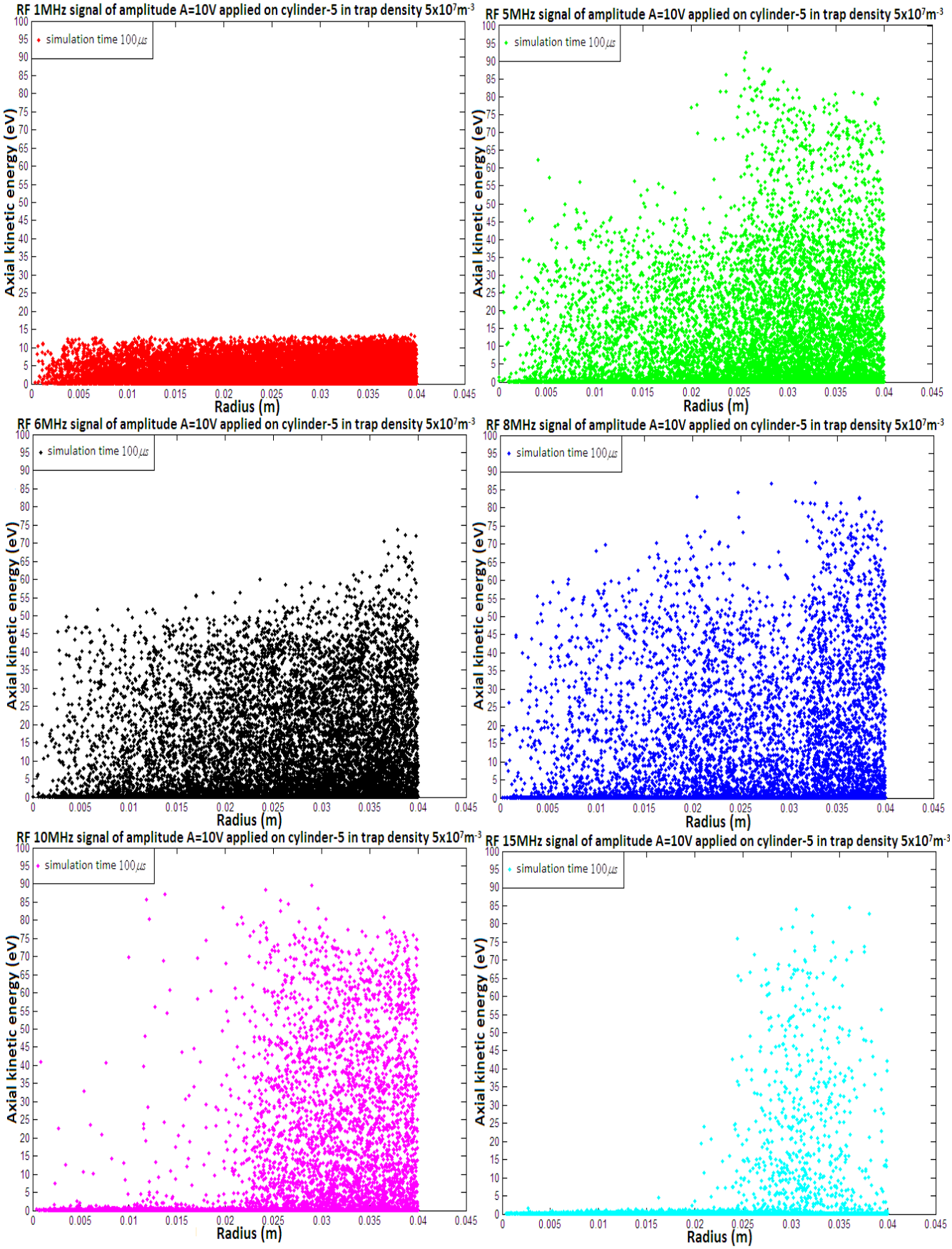

Figure 5.10 Axial kinetic energy (eV) as a function of the radius. The electron density is $5\times10^{7}\,m^{-3}$ and the RF applied on C5 has an amplitude of A = 10 V (1st simulation scheme mentioned in figure 4.4).

Table 5.3. Energy (eV) range of the electrons at simulation time 100 μs, for a density $5\times10^{7}\,m^{-3}$ and an amplitude A = 10 V of the RF drive applied on electrode C5.

Energy range (eV)	Number of electrons(%) of $KE(u_z)$	Number of electrons(%) of $KE(u_r)$	Number of electrons(%) of $KE(u_{phi})$	Number of electrons (%) of $KE(u_z)$	Number of electrons (%) of $KE(u_r)$	Number of electrons(%) of $KE(u_{phi})$
	RF 1MHz of amplitude A=10 V			**RF 5MHz of amplitude A=10 V**		
0-20 eV	19478 (100%)	19478 (100%)	19478 (100%)	16429 (84.346%)	18852 (96.786%)	18852 (96.786%)
20-70 eV	0 (0%)	0 (0%)	0 (0%)	2299 (11.8%)	0 (0%)	0 (0%)
70-100 eV	0 (0%)	0 (0%)	0 (0%)	124 (0.6366%)	0 (0%)	0 (0%)
≥100 eV	0 (0%)	0 (0%)	0 (0%)	0 (0%)	0 (0%)	0 (0%)
Total (No,%)	19478 (100%)	19478 (100%)	19478 (100%)	18852 (96.786%)	18852 (96.786%)	18852 (96.786%)
E (eV)	**RF 6MHz of amplitude A=10 V**			**RF 8MHz of amplitude A=10 V**		
0-20 eV	16488 (84.649%)	19478 (100%)	19478 (100%)	17015 (87.355%)	18909 (97.08%)	18909 (97.08%)
20-70 eV	2986 (15.33%)	0 (0%)	0 (0%)	1818 (9.33%)	0 (0%)	0 (0%)
70-100 eV	04 (0.021%)	0 (0%)	0 (0%)	76 (0.39%)	0 (0%)	0 (0%)
≥100 eV	0 (0%)	0 (0%)	0 (0%)	0 (0%)	0 (0%)	0 (0%)
Total (No,%)	19478 (100%)	19478 (100%)	19478 (100%)	18909 (97.08%)	18909 (97.08%)	18909 (97.08%)
E(eV)	**RF 10MHz of amplitude A=10 V**			**RF 15MHz of amplitude A=10 V**		
0-20 eV	16943 (86.98%)	18455 (94.748%)	18455 (94.748%)	18407 (94.5%)	18694 (95.975%)	18694 (95.975%)
20-70 eV	1408 (7.229%)	0 (0%)	0 (0%)	268 (1.376%)	0 (0%)	0 (0%)
70-100 eV	104 (0.534%)	0 (0%)	0 (0%)	18 (0.092%)	0 (0%)	0 (0%)
≥100 eV	0 (0%)	0 (0%)	0 (0%)	01 (0%)	0 (0%)	0 (0%)
Total (No,%)	18455 (94.748%)	18455 (94.748%)	18455 (94.748%)	18694 (95.975%)	18694 (95.975%)	18694 (95.975%)

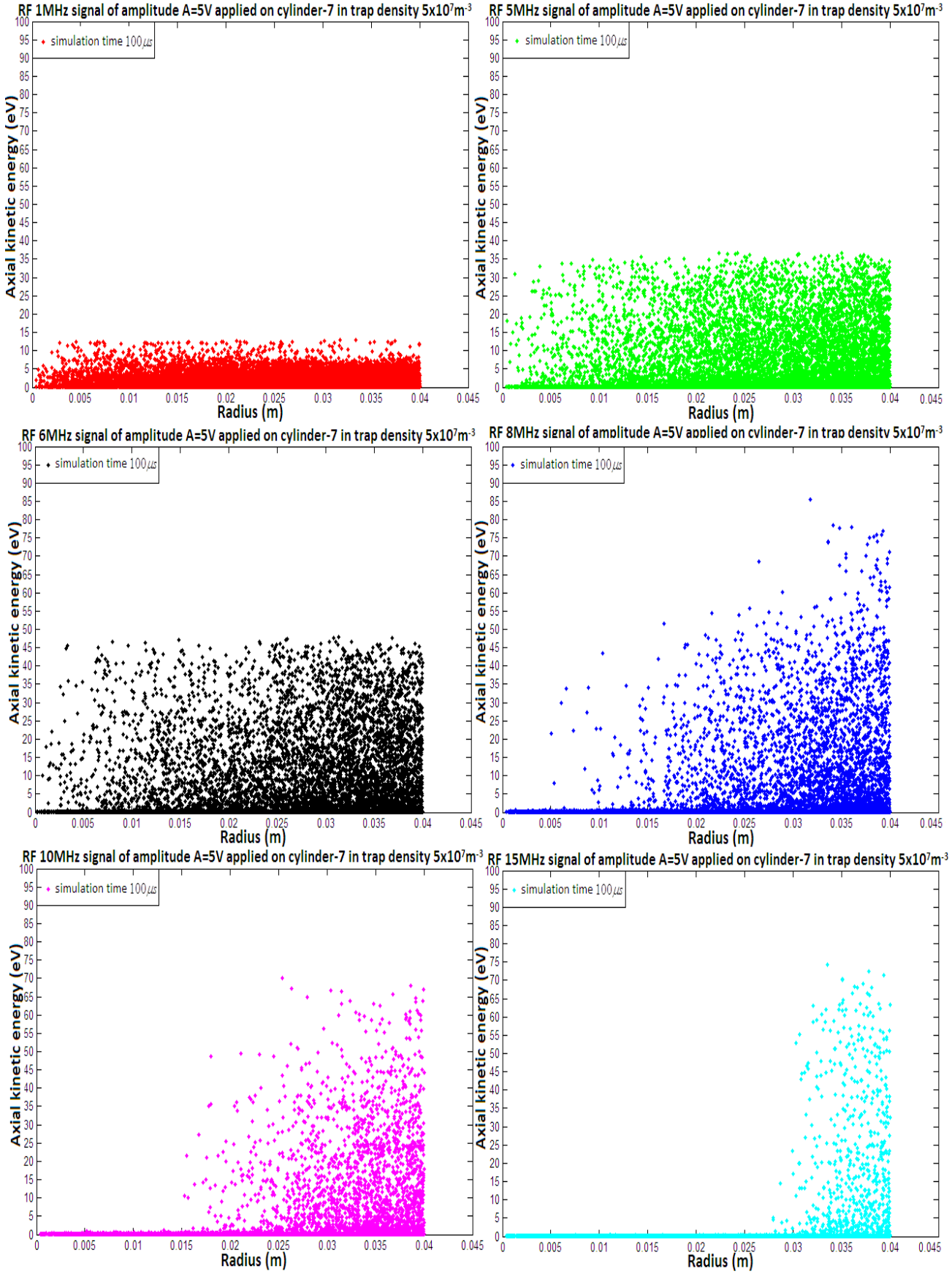

Figure 5.11 Axial kinetic energy (eV) as a function of the radius. The electron density is $5\times10^{7}\,m^{-3}$ and the RF applied on C7 has an amplitude of A = 5 V (2nd simulation scheme mentioned in figure 4.4).

Table 5.4. Energy (eV) range of the electrons at simulation time 100 μs, for a density $5\times10^{7}\,m^{-3}$ and an amplitude A = 5 V of the RF drive applied on electrode C7.

Energy range (eV)	Number of electrons(%) of $KE(u_z)$	Number of electrons(%) of $KE(u_r)$	Number of electrons(%) of $KE(u_{phi})$	Number of electrons(%) of $KE(u_z)$	Number of electrons(%) of $KE(u_r)$	Number of electrons(%) of $KE(u_{phi})$
	RF 1MHz of amplitude A=5 V			**RF 5MHz of amplitude A=5 V**		
0-20 eV	19478 (100%)	19478 (100%)	19478 (100%)	18187 (93.37%)	19478 (100%)	19478 (100%)
20-70 eV	0 (0%)	0 (0%)	0 (0%)	1291 (6.628%)	0 (0%)	0 (0%)
70-100 eV	0 (0%)	0 (0%)	0 (0%)	0 (0%)	0 (0%)	0 (0%)
$\geq$100 eV	0 (0%)	0 (0%)	0 (0%)	0 (0%)	0 (0%)	0 (0%)
Total (No,%)	19478 (100%)	19478 (100%)	19478 (100%)	19478 (100%)	19478 (100%)	19478 (100%)
E (eV)	**RF 6MHz of amplitude A=5 V**			**RF 8MHz of amplitude A=5 V**		
0-20 eV	17933 (92.07%)	19478 (100%)	19478 (100%)	18515 (95.056%)	19462 (99.918%)	19462 (99.918%)
20-70 eV	1545 (7.93%)	0 (0%)	0 (0%)	931 (4.779%)	0 (0%)	0 (0%)
70-100 eV	0 (0%)	0 (0%)	0 (0%)	16 (0%)	0 (0%)	0 (0%)
$\geq$100 eV	0 (0%)	0 (0%)	0 (0%)	0 (0%)	0 (0%)	0 (0%)
Total (No,%)	19478 (100%)	19478 (100%)	19478 (100%)	19462 (99.918%)	19462 (99.918%)	19462 (99.918%)
E(eV)	**RF 10MHz of amplitude A=5 V**			**RF 15MHz of amplitude A=5 V**		
0-20 eV	18862 (96.837%)	19478 (100%)	19478 (100%)	19227 (98.711%)	19478 (100%)	19478 (100%)
20-70 eV	615 (3.1574%)	0 (0%)	0 (0%)	246 (1.263%)	0 (0%)	0 (0%)
70-100 eV	01 (0.005%)	0 (0%)	0 (0%)	05 (0.026%)	0 (0%)	0 (0%)
$\geq$100 eV	0 (0%)	0 (0%)	0 (0%)	0 (0%)	0 (0%)	0 (0%)
Total (No,%)	19478 (100%)	19478 (100%)	19478 (100%)	19478 (100%)	19478 (100%)	19478 (100%)

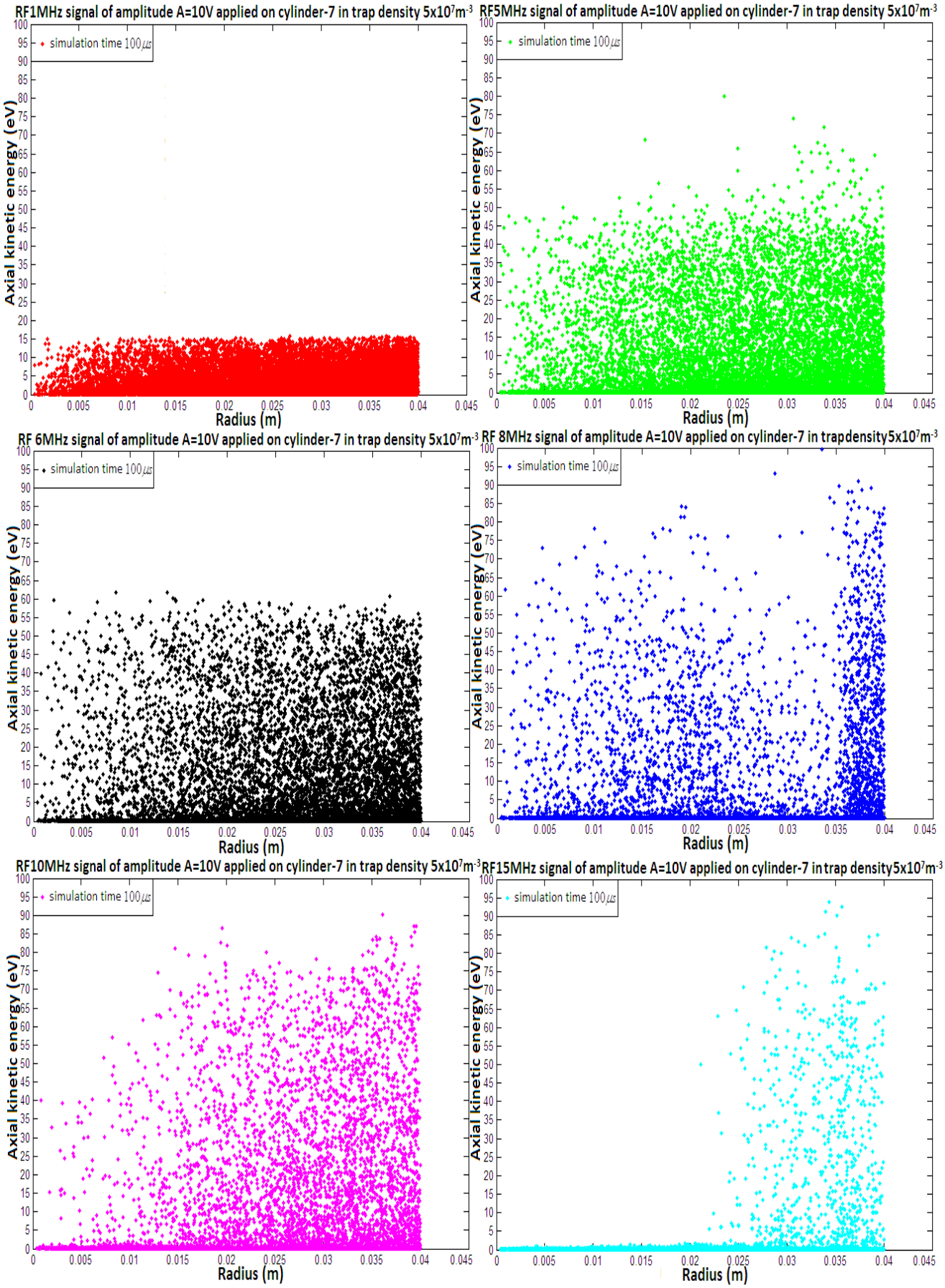

Figure 5.12 Axial kinetic energy (eV) as a function of the radius. The electron density is $5\times10^{7}\,m^{-3}$ and the RF applied on C7 has an amplitude of A = 10 V (2nd simulation scheme mentioned in figure 4.4).

Table 5.5. Energy (eV) range of the electrons at simulation time 100 µs, for a density $5\times10^{7}\,m^{-3}$ and an amplitude A = 10 V of the RF drive applied on electrode C7.

Energy range (eV)	Number of electrons(%) of $KE(u_z)$	Number of electrons(%) of $KE(u_r)$	Number of electrons(%) of $KE(u_{phi})$	Number of electrons(%) of $KE(u_z)$	Number of electrons(%) of $KE(u_r)$	Number of electrons(%) of $KE(u_{phi})$
	RF 1MHz of amplitude A=10 V			**RF 5MHz of amplitude A=10 V**		
0-20 eV	19478 (100%)	19478 (100%)	19478 (100%)	16799 (86.246%)	19477 (99.995%)	19477 (99.995%)
20-70 eV	0 (0%)	0 (0%)	0 (0%)	2675 (13.733%)	0 (0%)	0 (0%)
70-100 eV	0 (0%)	0 (0%)	0 (0%)	03 (0.0154%)	0 (0%)	0 (0%)
≥ 100 eV	0 (0%)	0 (0%)	0 (0%)	0 (0%)	0 (0%)	0 (0%)
Total (No,%)	19478 (100%)	19478 (100%)	19478 (100%)	19477 (99.995%)	19477 (99.995%)	19477 (99.995%)
E (eV)	**RF 6MHz of amplitude A=10 V**			**RF 8MHz of amplitude A=10 V**		
0-20 eV	16885 (86.687%)	19478 (100%)	19478 (100%)	15442 (79.279%)	16574 (85.091%)	16574 (85.091%)
20-70 eV	2593 (13.312%)	0 (0%)	0 (0%)	1048 (5.38%)	0 (0%)	0 (0%)
70-100 eV	0 (0%)	0 (0%)	0 (0%)	84 (0.431%)	0 (0%)	0 (0%)
≥ 100 eV	0 (0%)	0 (0%)	0 (0%)	0 (0%)	0 (0%)	0 (0%)
Total (No,%)	19478 (100%)	19478 (100%)	19478 (100%)	16574 (85.091%)	16574 (85.091%)	16574 (85.091%)
E(eV)	**RF 10MHz of amplitude A=10 V**			**RF 15MHz of amplitude A=10 V**		
0-20 eV	17538 (90.04%)	19316 (99.168%)	19316 (99.168%)	18444 (94.691%)	18831 (96.678%)	18831 (96.678%)
20-70 eV	1659 (8.517%)	0 (0%)	0 (0%)	347 (1.7815%)	0 (0%)	0 (0%)
70-100 eV	119 (0.611%)	0 (0%)	0 (0%)	40 (0.2054%)	0 (0%)	0 (0%)
≥ 100 eV	0 (0%)	0 (0%)	0 (0%)	0 (0%)	0 (0%)	0 (0%)
Total (No,%)	19316 (99.168%)	19316 (99.168%)	19316 (99.168%)	18831 (96.678%)	18831 (96.678%)	18831 (96.678%)

5.6 Simulations of RF heating at high electron plasma density

The results of the electrostatic PIC simulations for an electron plasma density $10^{12}\,m^{-3}$ up to simulation time of $100\,\mu s$ is presented in figures 5.13 and 5.14 (axial temperature vs time) and in figures 5.15-5.16 (axial kinetic energy vs radius). The number of real particles per simulation particles is in this case $np2c = 8.247\times10^{4}$. The temperature of the confined electrons increases with the excitation frequency from 5 MHz to 10MHz and then decreases from 10 to 15 MHz. The maximum final temperatures of 30.03 eV and 40.32 eV are observed at 10 MHz for an RF drive amplitude of 5 V and 10 V, respectively. It is observed that for a simulation time of $100\,\mu s$ the particle losses are 12.776 %, 12.594 %, 15.531%, 13.47% and 14.05% (of a total of 37789 initial macro-particles) for the frequencies 5MHz, 8MHz, 10MHz, 12MHz and 15 MHz at an amplitude of 5 V, and 24.01%, 27.736%, 36.317%, 46.561% and 46.948% for an amplitude of 10 V.

In general, it is confirmed that the RF heating is more effective in the outer radial part of the trap, so that the electrons localized near to wall having higher energy (≥ 20 eV) are able to ionize the residual gas better than the electrons located close to the central part of the trap.

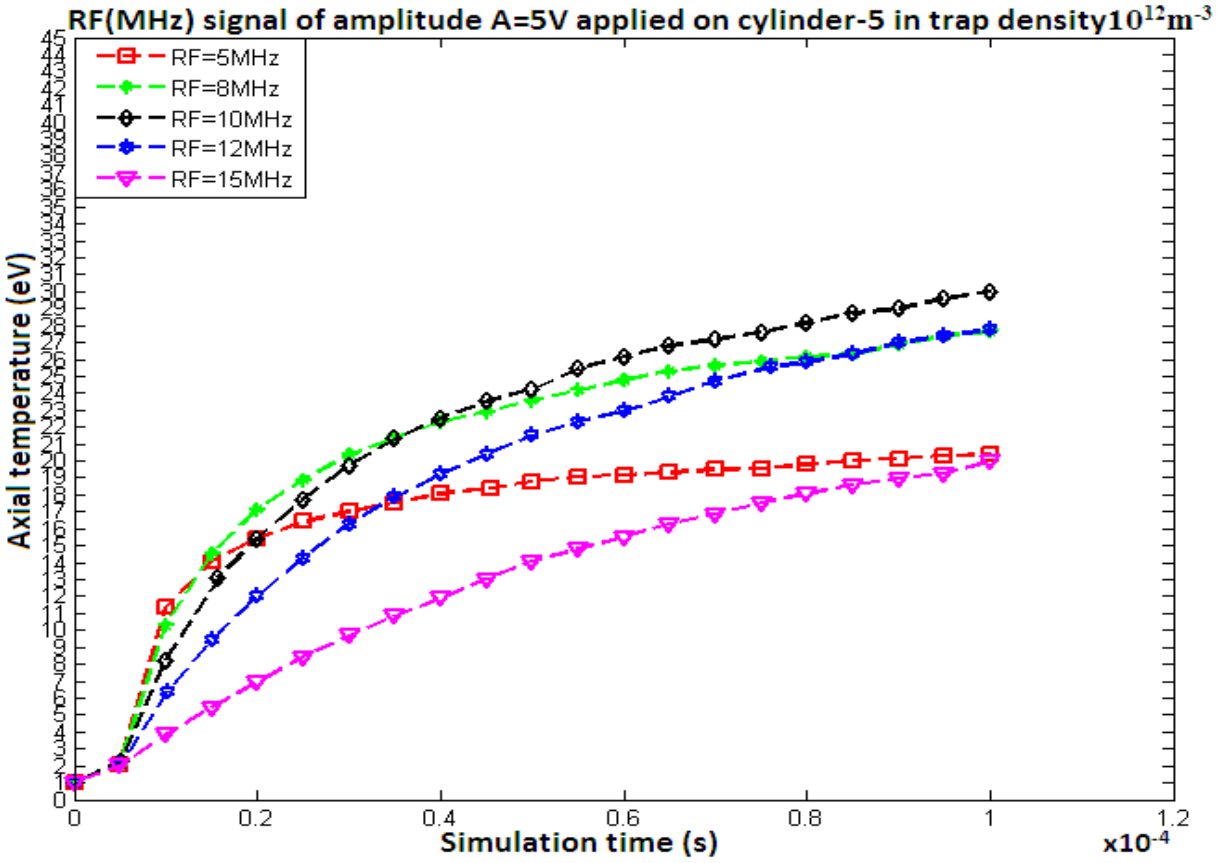

Figure 5.13 Axial temperature vs time for an electron plasma density $5\times10^{7}\,m^{-3}$ and an RF drive of amplitude A = 5 V applied on C5 (3rd simulation scheme mentioned in figure 4.4).

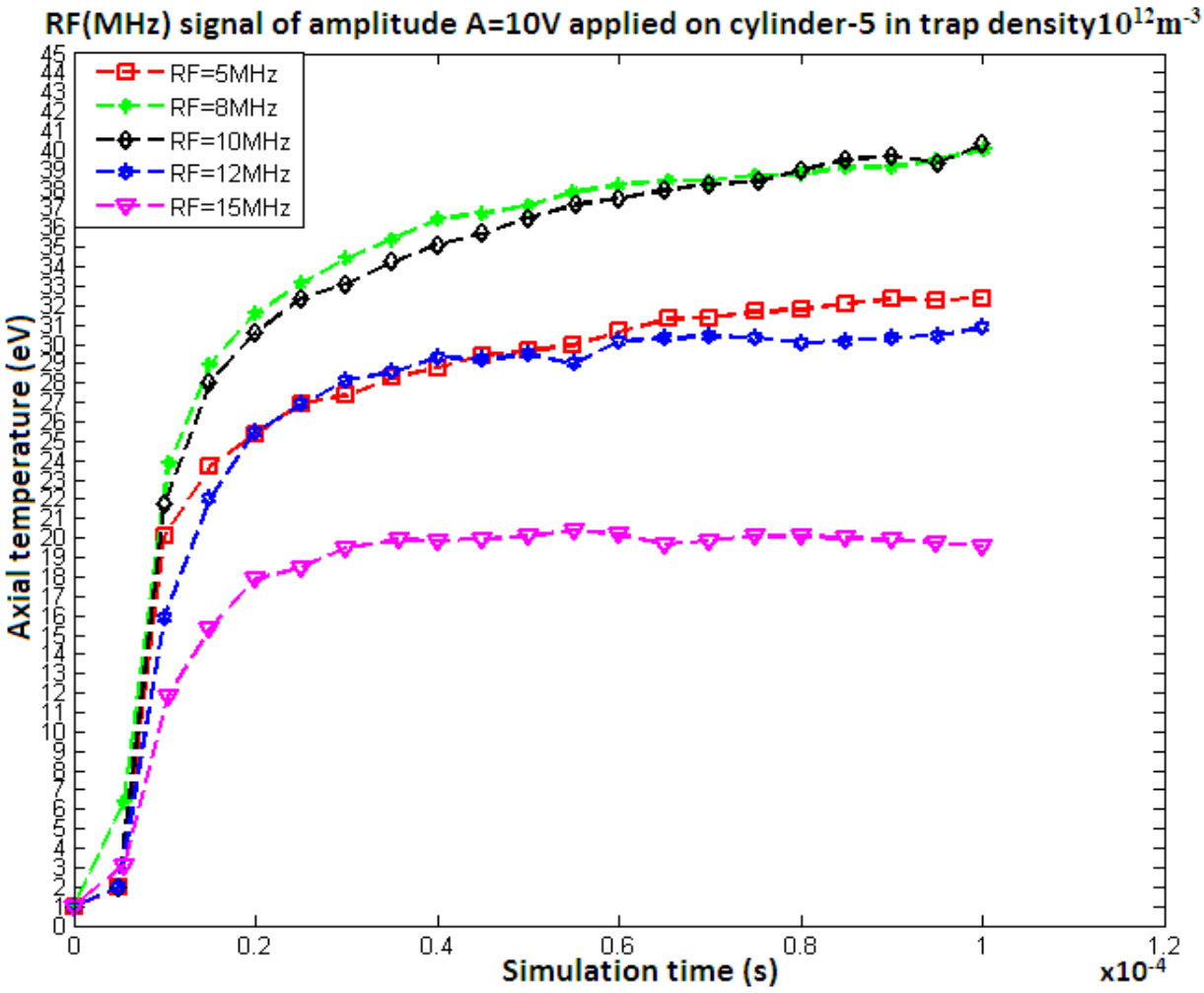

Figure 5.14 Axial temperature vs time for an electron plasma density $5\times10^{7}\,m^{-3}$ and an RF drive of amplitude A = 10 V applied on C5 (3rd simulation scheme mentioned in figure 4.4).

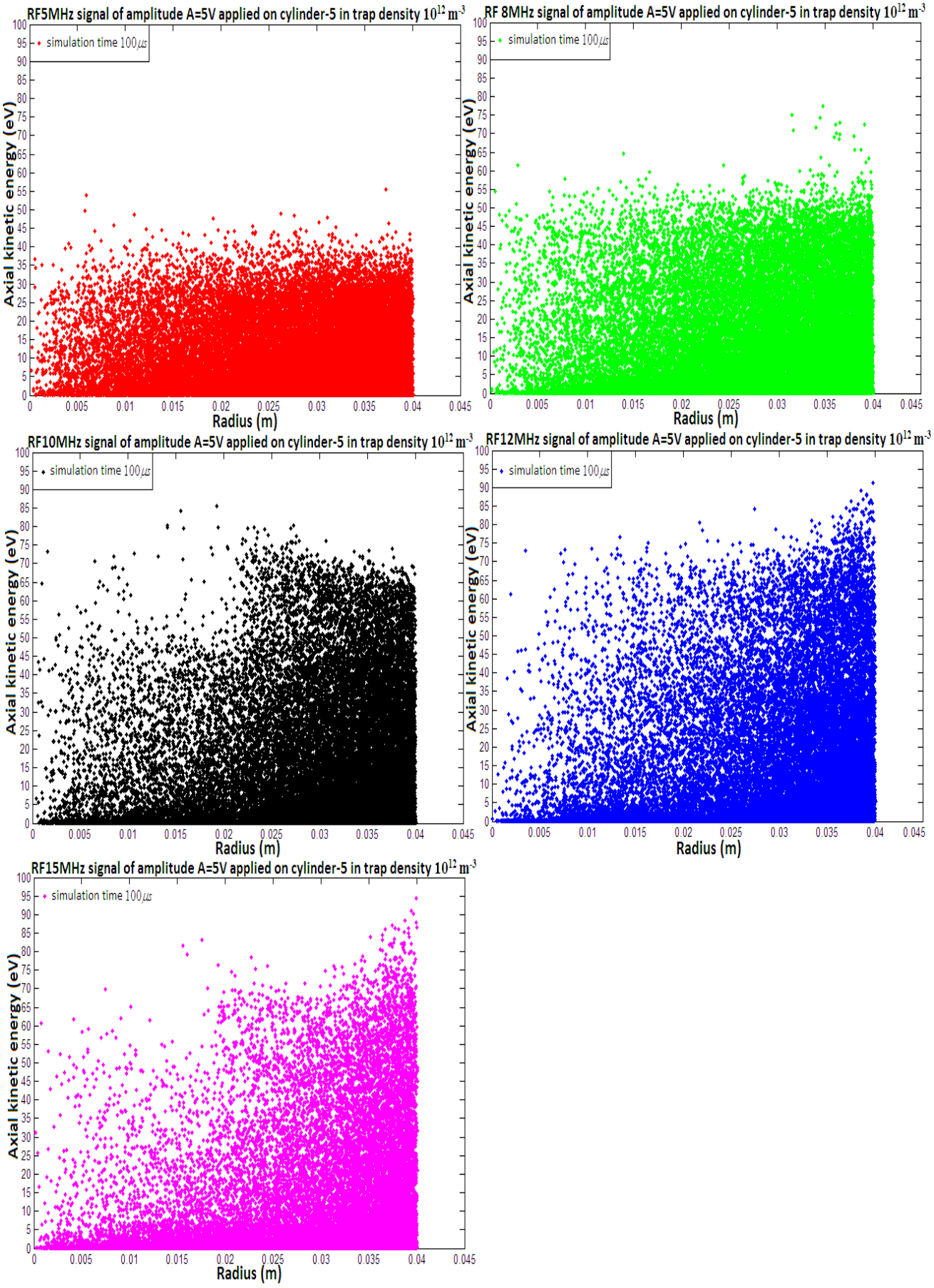

Figure 5.15 Axial kinetic energy (eV) as a function of the radius. The electron density is $10^{12}\,m^{-3}$ and the RF applied on C5 has an amplitude of A = 5 V.

Table 5.6. Energy (eV) range of the electrons at simulation time 100 µs, for a density $10^{12}\,m^{-3}$ and an amplitude A = 5 V of the RF drive applied on electrode C5.

Energy range (eV)	Number of electrons(%) of $KE(u_z)$	Number of electrons(%) of $KE(u_r)$	Number of electrons(%) of $KE(u_{phi})$	Number of electrons(%) of $KE(u_z)$	Number of electrons(%) of $KE(u_r)$	Number of electrons(%) of $KE(u_{phi})$
	RF 5MHz of amplitude A=5 V			**RF 8MHz of amplitude A=5 V**		
0-20 eV	26894 (71.169%)	32961 (87.224%)	32961 (87.224%)	23264 (61.563%)	33030 (87.406%)	33030 (87.406%)
20-70 eV	6067 (16.055%)	0 (0%)	0 (0%)	9758 (25.822%)	0 (0%)	0 (0%)
70-100 eV	0 (0%)	0 (0%)	0 (0%)	08 (0.0211%)	0 (0%)	0 (0%)
≥100 eV	0 (0%)	0 (0%)	0 (0%)	0 (0%)	0 (0%)	0 (0%)
Total (No, %)	32961 (87.224%)	32961 (87.224%)	32961 (87.224%)	33030 (87.406%)	33030 (87.406%)	33030 (87.406%)
E (eV)	**RF 10MHz of amplitude A=5 V**			**RF 12MHz of amplitude A=5 V**		
0-20 eV	22144 (58.599%)	31920 (84.469%)	31920 (84.469%)	23661 (62.613%)	32699 (86.53%)	32699 (86.53%)
20-70 eV	9654 (25.547%)	0 (0%)	0 (0%)	8753 (23.163%)	0 (0%)	0 (0%)
70-100 eV	122 (0.323%)	0 (0%)	0 (0%)	285	0 (0%)	0 (0%)
≥100 eV	0 (0%)	0 (0%)	0 (0%)	0 (0%)	0 (0%)	0 (0%)
Total (No, %)	31920 (84.469%)	31920 (84.469%)	31920 (84.469%)	32699 (86.53%)	32699 (86.53%)	32699 (86.53%)
E(eV)	**RF 15MHz of amplitude A=5 V**					
0-20 eV	26212 (69.364%)	32479 (85.95%)	32479 (85.95%)			
20-70 eV	6082 (16.095%)	0 (0%)	0 (0%)			
70-100 eV	184 (0.487%)	0 (0%)	0 (0%)			
≥100 eV	01 (0.0026%)	0 (0%)	0 (0%)			
Total (No, %)	32479 (85.95%)	32479 (85.95%)	32479 (85.95%)			

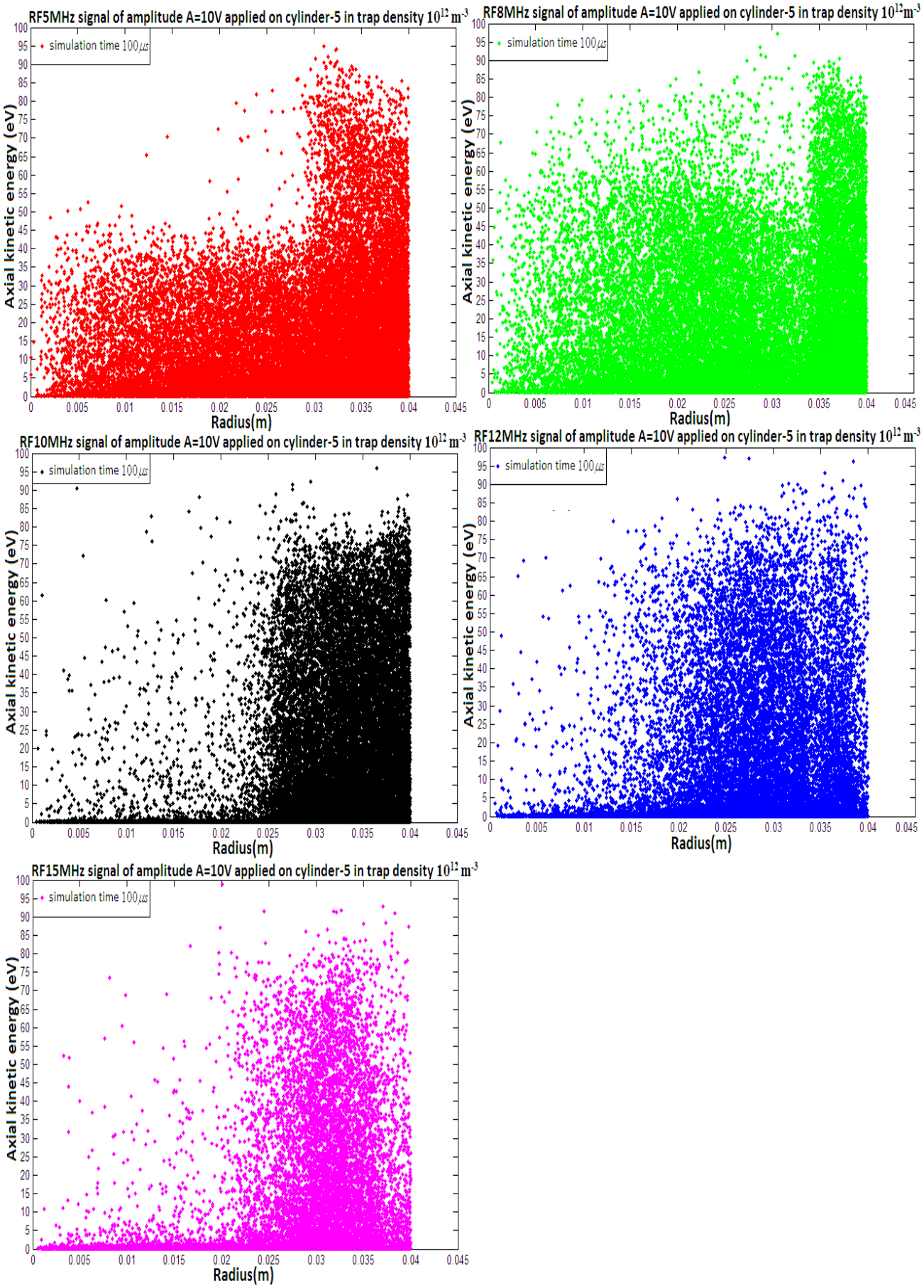

Figure 5.16 Axial kinetic energy (eV) as a function of the radius. The electron density is $10^{12}\,m^{-3}$ and the RF applied on C5 has an amplitude of A = 10 V.

Table 5.7. Energy (eV) range of the electrons at simulation time 100 µs, for a density $10^{12}\,m^{-3}$ and an amplitude A = 10 V of the RF drive applied on electrode C5.

Energy range (eV)	**RF 5MHz of amplitude A=10 V**			**RF 8MHz of amplitude A=10 V**		
	Number of electrons(%) of $KE(u_z)$	Number of electrons(%) of $KE(u_r)$	Number of electrons(%) of $KE(u_{phi})$	Number of electrons(%) of $KE(u_z)$	Number of electrons(%) of $KE(u_r)$	Number of electrons(%) of $KE(u_{phi})$
0-20 eV	19412 (51.369%)	28717 (75.99%)	28717 (75.99%)	16273 (43.063%)	27308 (72.264%)	27308 (72.264%)
20-70 eV	8880 (23.499%)	0 (0%)	0 (0%)	10447 (27.646%)	0 (0%)	0 (0%)
70-100 eV	425 (1.125%)	0 (0%)	0 (0%)	588 (1.556%)	0 (0%)	0 (0%)
≥ 100 eV	0 (0%)	0 (0%)	0 (0%)	0 (0%)	0 (0%)	0 (0%)
Total (No,%)	28717 (75.99%)	28717 (75.99%)	28717 (75.99%)	27308 (72.264%)	27308 (72.264%)	27308 (72.264%)
E (eV)	**RF 10MHz of amplitude A=10 V**			**RF 12MHz of amplitude A=10 V**		
0-20 eV	14539 (38.4742%)	24065 (63.683%)	24065 (63.683%)	14111 (37.342%)	20194 (53.439%)	20194 (53.439%)
20-70 eV	9002 (23.822%)	0 (0%)	0 (0%)	5737 (15.182%)	0 (0%)	0 (0%)
70-100 eV	523 (1.384%)	0 (0%)	0 (0%)	344 (0.91%)	0 (0%)	0 (0%)
≥ 100	01 (0.00265%)	0 (0%)	0 (0%)	02 (0.0053%)	0 (0%)	0 (0%)
Total (No,%)	24065 (63.683%)	24065 (63.683%)	24065 (63.683%)	20194 (53.439%)	20194 (53.439%)	20194 (53.439%)
E(eV)	**RF 15MHz of amplitude A=10 V**					
0-20 eV	16272 (43.06%)	20048 (53.052%)	20048 (53.052%)			
20-70 eV	3559 (9.418%)	0 (0%)	0 (0%)			
70-100 eV	216 (0.572%)	0 (0%)	0 (0%)			
≥ 100 eV	01 0.00262	0 (0%)	0 (0%)			
Total (No,%)	20048 (53.052%)	20048 (53.052%)	20048 (53.052%)			

5.7 RF heating with a background gas

In a real plasma many reactions play a role, ranging from elastic collisions, such as collisions between charged and neutral particles, to inelastic collisions, such as electron-neutral ionization collisions and even chemical reactions. However the complexity of these processes cannot be fully integrated into numerical codes. The OOPIC Pro code is able to treat the most fundamental processes such as elastic collisions, excitation and ionization of the background gas (inelastic interaction). In the present case, the process of ionization of the background gas due to electron-neutral impacts has been taken into account. The incident electron loses part of its energy (equivalent to the ionization threshold energy), creates an ion and a secondary electron, and gets scattered after the collision. Hydrogen pressures of $P = 10^{-8} torr, P = 10^{-7} torr$ and $\mathrm{P} = 10^{-6} torr$ have been considered in the simulations. As it was discussed about the results of the simulations with no background gas, the maximum RF heating is achieved for an excitation frequency of approximately 5 MHz. This case has therefore been selected for the electrostatic Monte-Carlo PIC simulations of electron neutral collisions (H_2) to investigate the importance of the ionization process.

The electron-neutral collision frequency can be estimated as

$$\upsilon_e = n_H \sigma_s^{e/H} \left(\frac{kT_e}{m_e} \right)^{\frac{1}{2}} \qquad 5.8$$

where n_H is the neutral density, $\sigma_s^{e/H} = 5 \times 10^{-15} cm^2$ is the typically cross section and kT_e is temperature in eV. As it seen in figures 5.17 and 5.18, at the end of the simulation, the electron neutral (H_2) collision times are 5.215 10^{-5} s, 5.563 10^{-4} s, and 5.682 10^{-3} s at a background pressure of 10^{-6} torr, 10^{-7} torr and 10^{-8} torr, respectively, for the case of $5 \times 10^7 m^{-3}$ electron density and 5 V amplitude of the applied RF. Similarly, for the same pressures at a density of $10^{12} m^{-3}$, figures 5.19 and 5.20 show that the electron neutral collision times are correspondingly $3.302 \times 10^{-5} s$, $3.272 \times 10^{-4} s$ and $3.277 \times 10^{-3} s$. Similar results for a 10 V amplitude of the RF drive are shown in figures 5.21-5.24. These result show that an increased collision frequency is obtained at higher RF drive amplitudes since the electron temperature is also higher, so that more ionization and secondary electrons are generated as mentioned in table 5.8 (a, b). Note also that at increasing pressures, electron–neutral collisions will become the dominant factor causing plasma expansion (the expansion rate is expected to increase linearly with the background gas pressure).

As discussed in chapter 3, in the experiments RF plasma formation is obtained initially in the outer radial part of the trap. The created positive ions may then interact with the cylindrical wall of the trap and get lost because for the provided static homogenous magnetic field of magnitude ≤ 0.2 T their Larmor radius is large. The ions are not confined also axially, since negative electrostatic potentials are applied at the end cylinders for the confinement of the electron plasma.

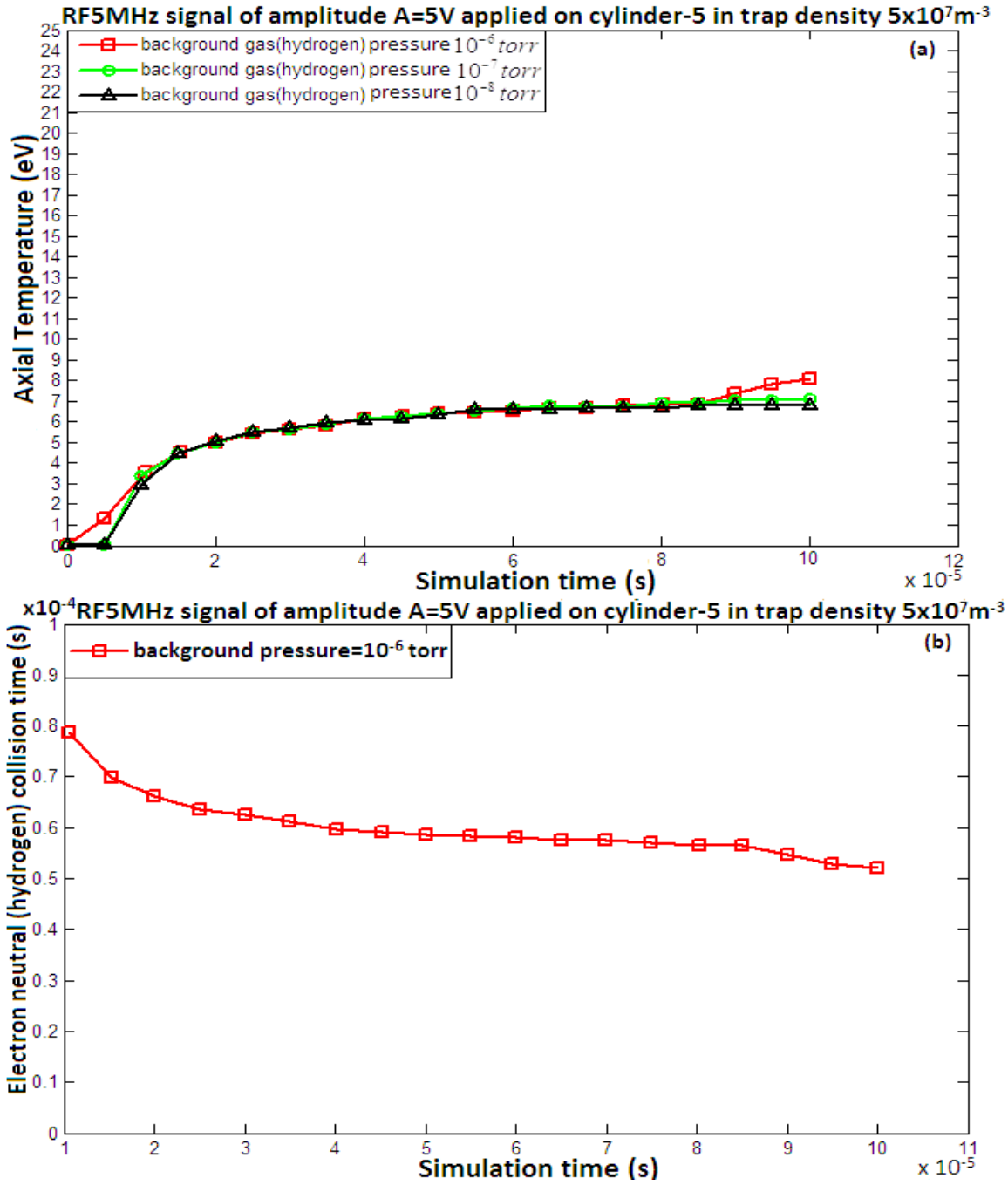

Figure 5.17 (a) Electron axial temperature (eV) vs time for a 5 MHz excitation frequency of amplitude A = 5V and electron density $5\times10^{7}\,m^{-3}$ where hydrogen used as background gas at pressures of $10^{-6}torr$,$10^{-7}torr$ and $10^{-8}torr$ (b) electron neutral collision time vs. simulation time (s) at a pressure of $10^{-6}torr$.

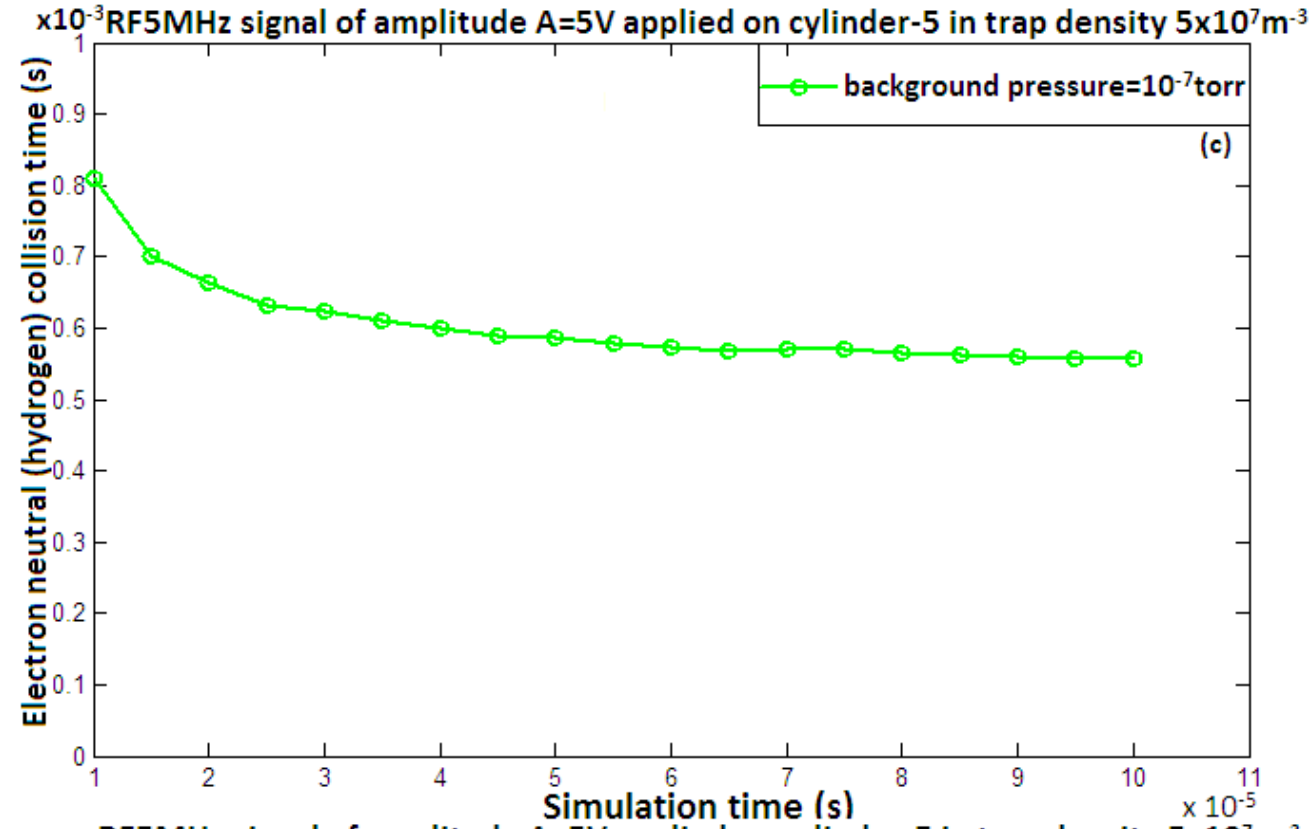

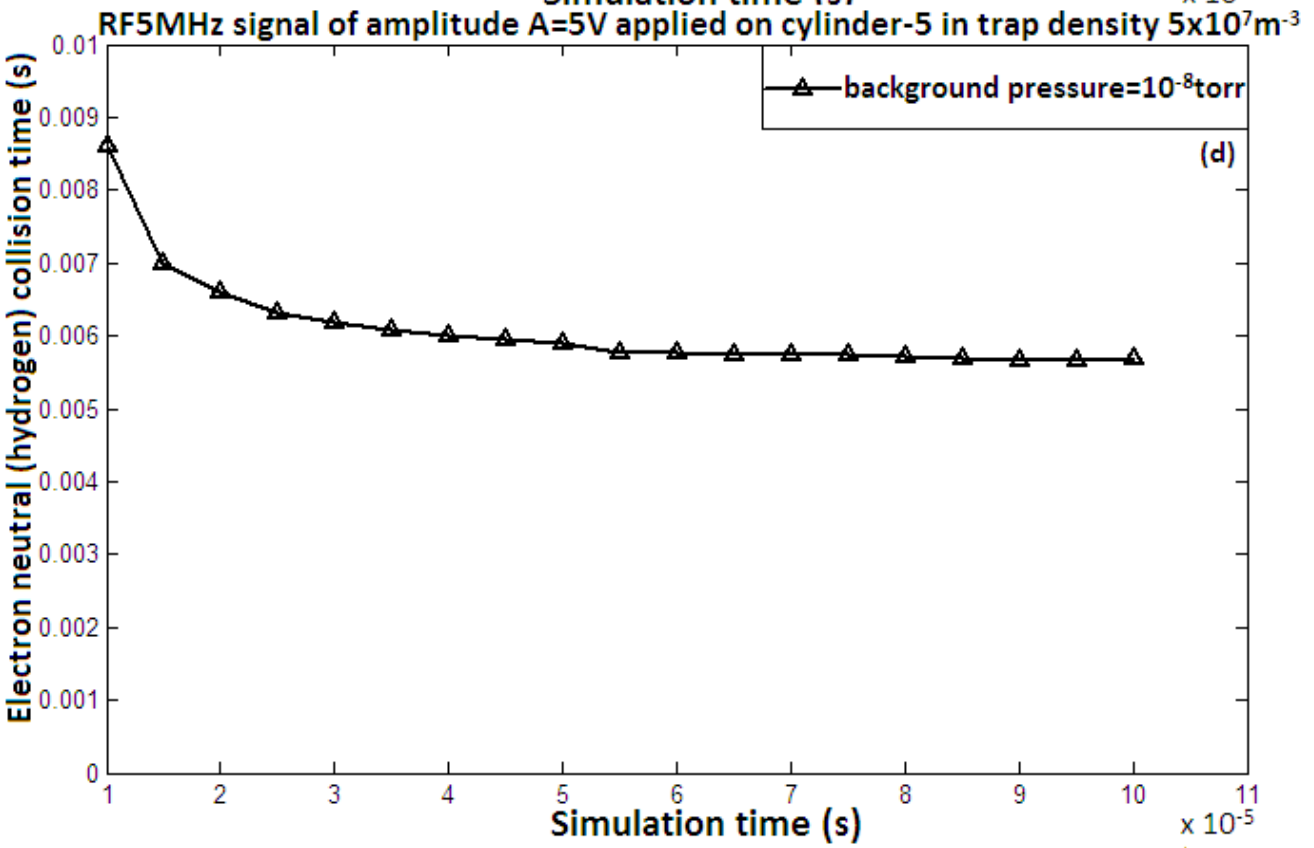

Figure 5.18 For the same data as in figure 5.17, electron neutral collision time vs. simulation time (s) at a pressure of (c) $10^{-7}\,torr$ **and (d)** $10^{-8}\,torr$ **.**

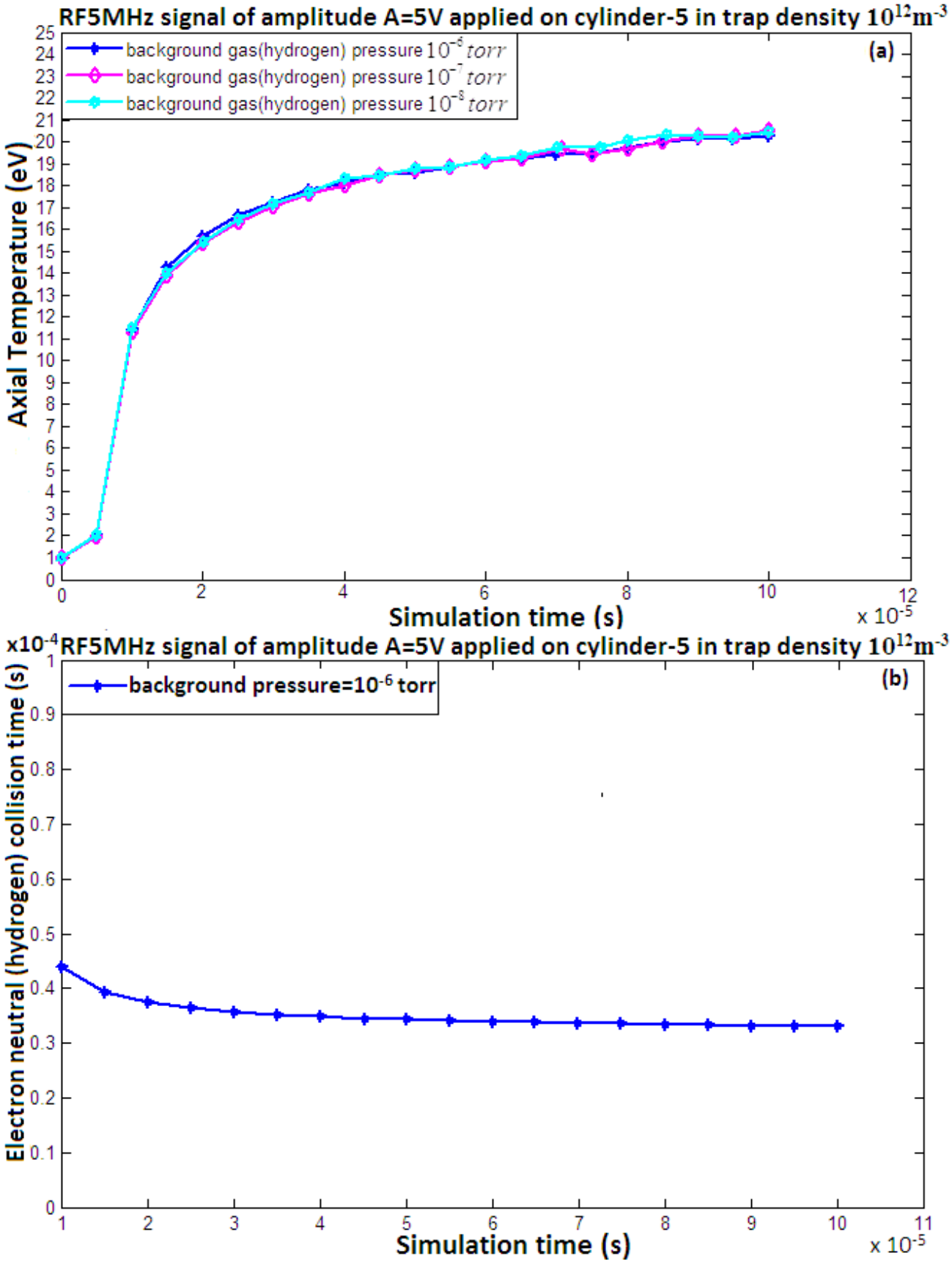

Figure 5.19 (a) Electron axial temperature (eV) vs time for a 5 MHz excitation frequency of amplitude A = 5V and electron density 10^{12} m^{-3} where hydrogen used as background gas at pressures of $10^{-6}torr$,$10^{-7}torr$ and $10^{-8}torr$ (b) electron neutral collision time vs. simulation time (s) at a pressure of $10^{-6}torr$.

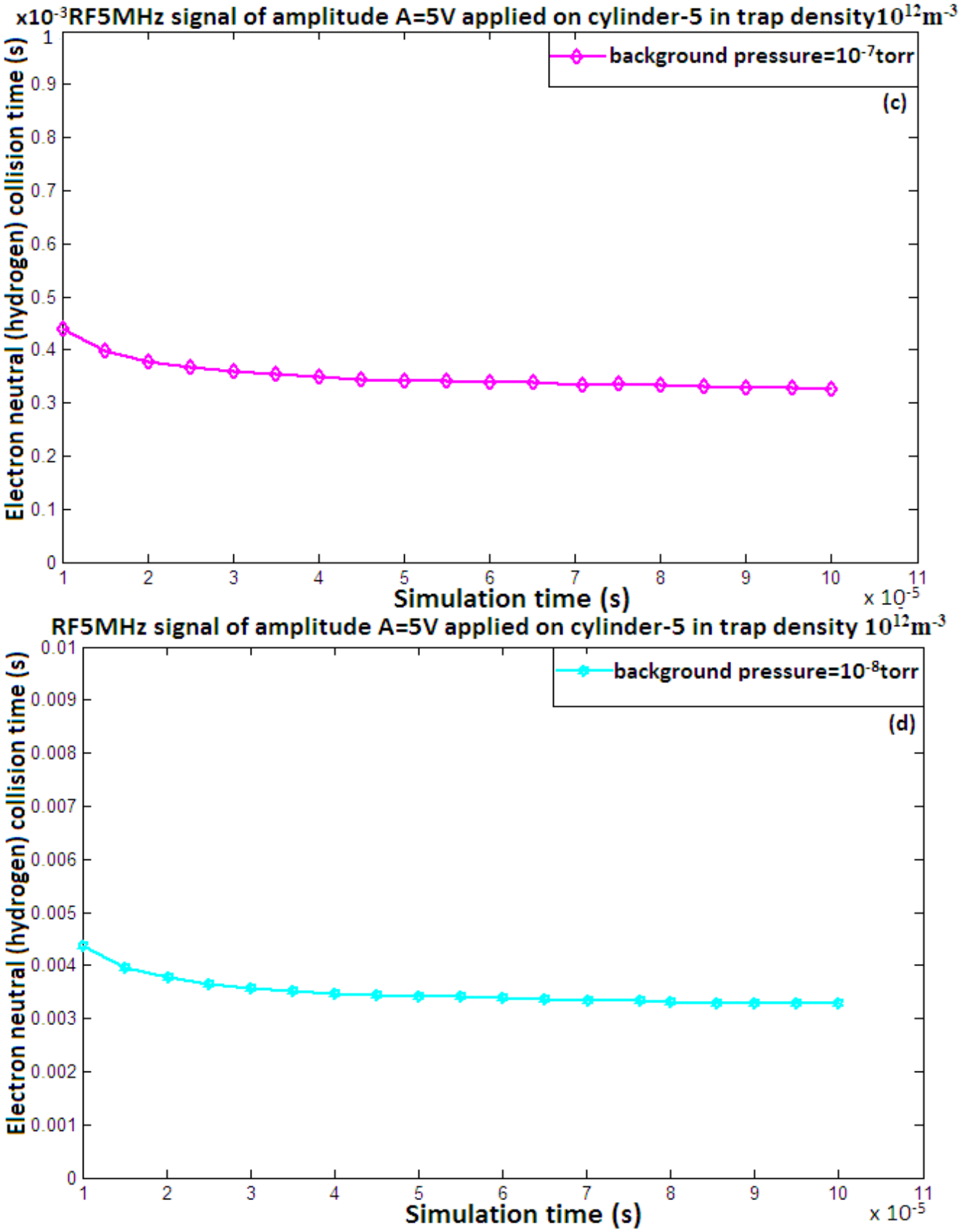

Figure 5.20 For the same data as in figure 5.19, electron neutral collision time vs. simulation time (s) at a pressure of (c) $10^{-7}\,torr$ **and (d)** $10^{-8}\,torr$ **.**

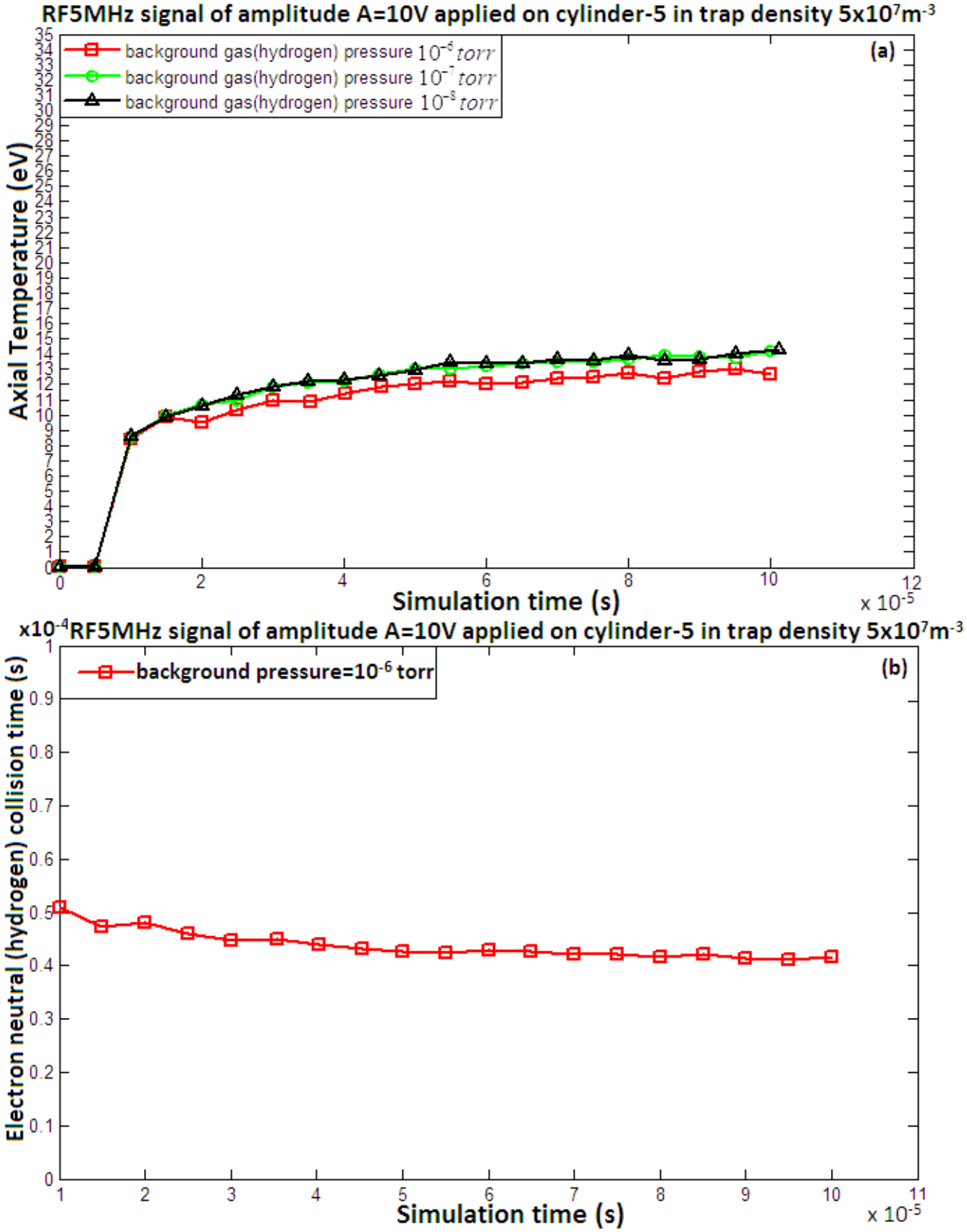

Figure 5.21 (a) Electron axial temperature (eV) vs time for a 5 MHz excitation frequency of amplitude A = 10V and electron density 5 10^7 m^{-3} where hydrogen used as background gas at pressures of $10^{-6} torr, 10^{-7} torr$ and $10^{-8} torr$ (b) electron neutral collision time vs. simulation time (s) at a pressure of $10^{-6} torr$.

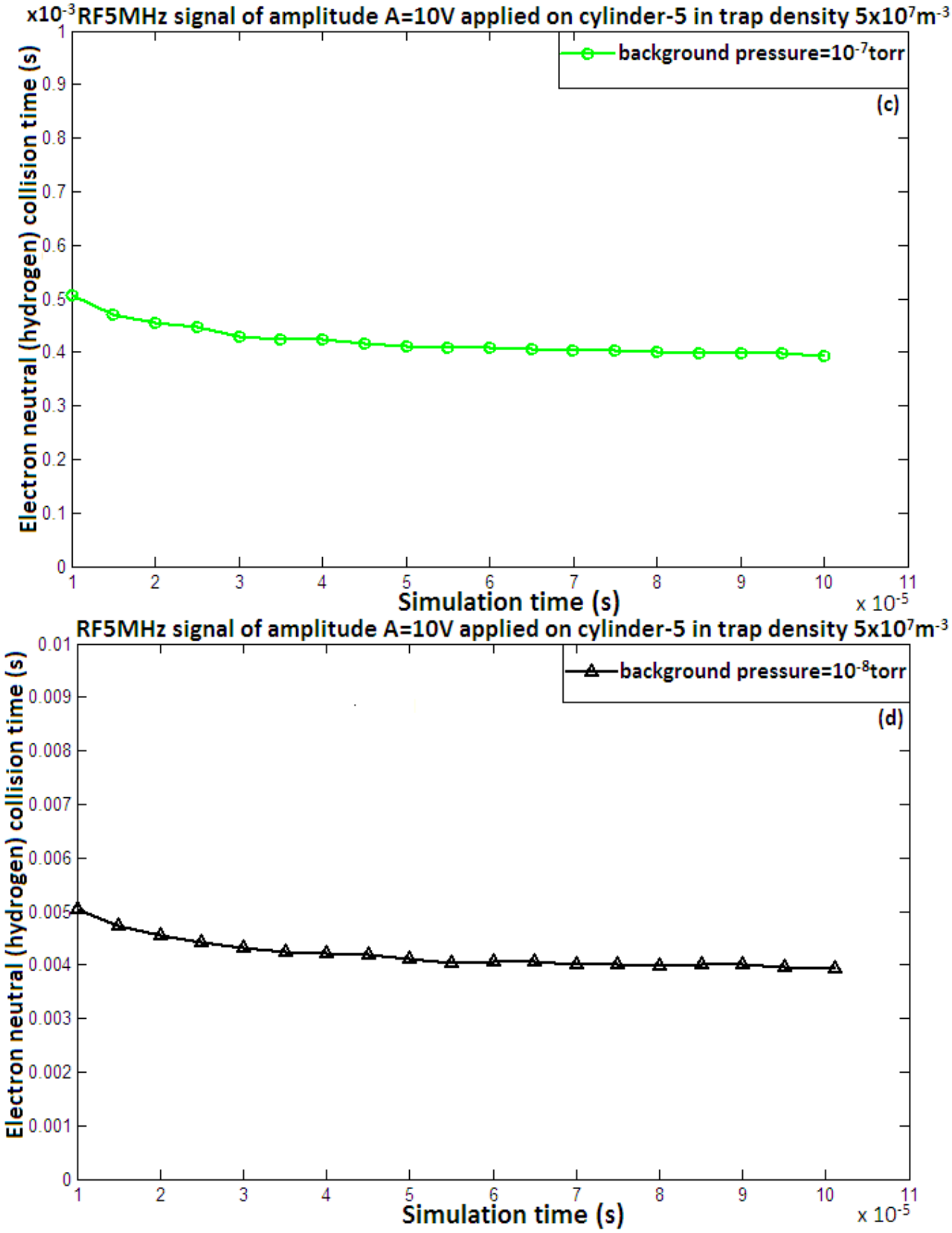

Figure 5.22 For the same data as in figure 5.21, electron neutral collision time vs. simulation time (s) at a pressure of (c) $10^{-7}\,torr$ **and (d)** $10^{-8}\,torr$ **.**

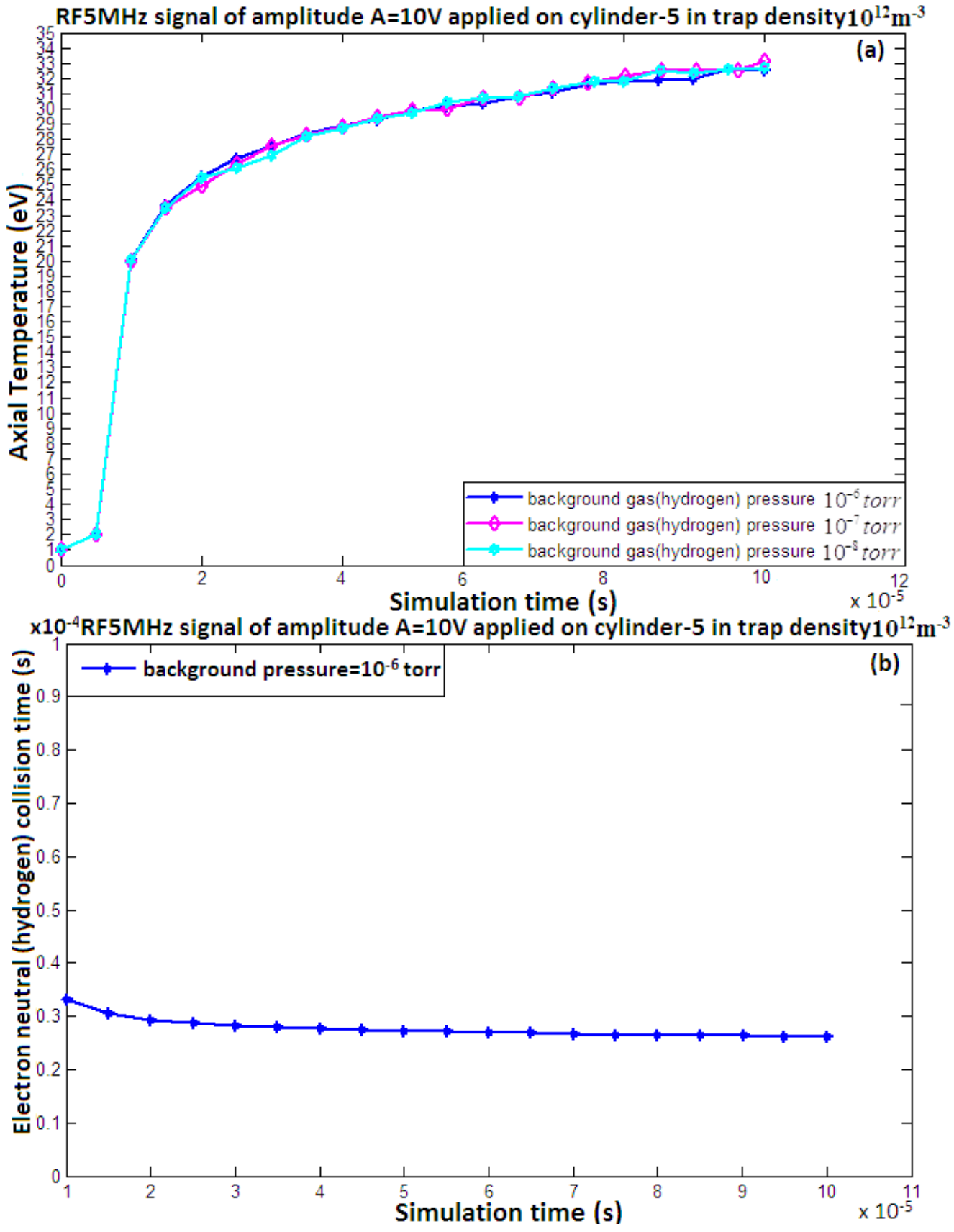

Figure 5.23 (a) Electron axial temperature (eV) vs time for a 5 MHz excitation frequency of amplitude A = 10 V and electron density 10^{12} m^{-3} where hydrogen used as background gas at pressures of $10^{-6}torr$,$10^{-7}torr$ and $10^{-8}torr$ (b) electron neutral collision time vs. simulation time (s) at a pressure of $10^{-6}torr$.

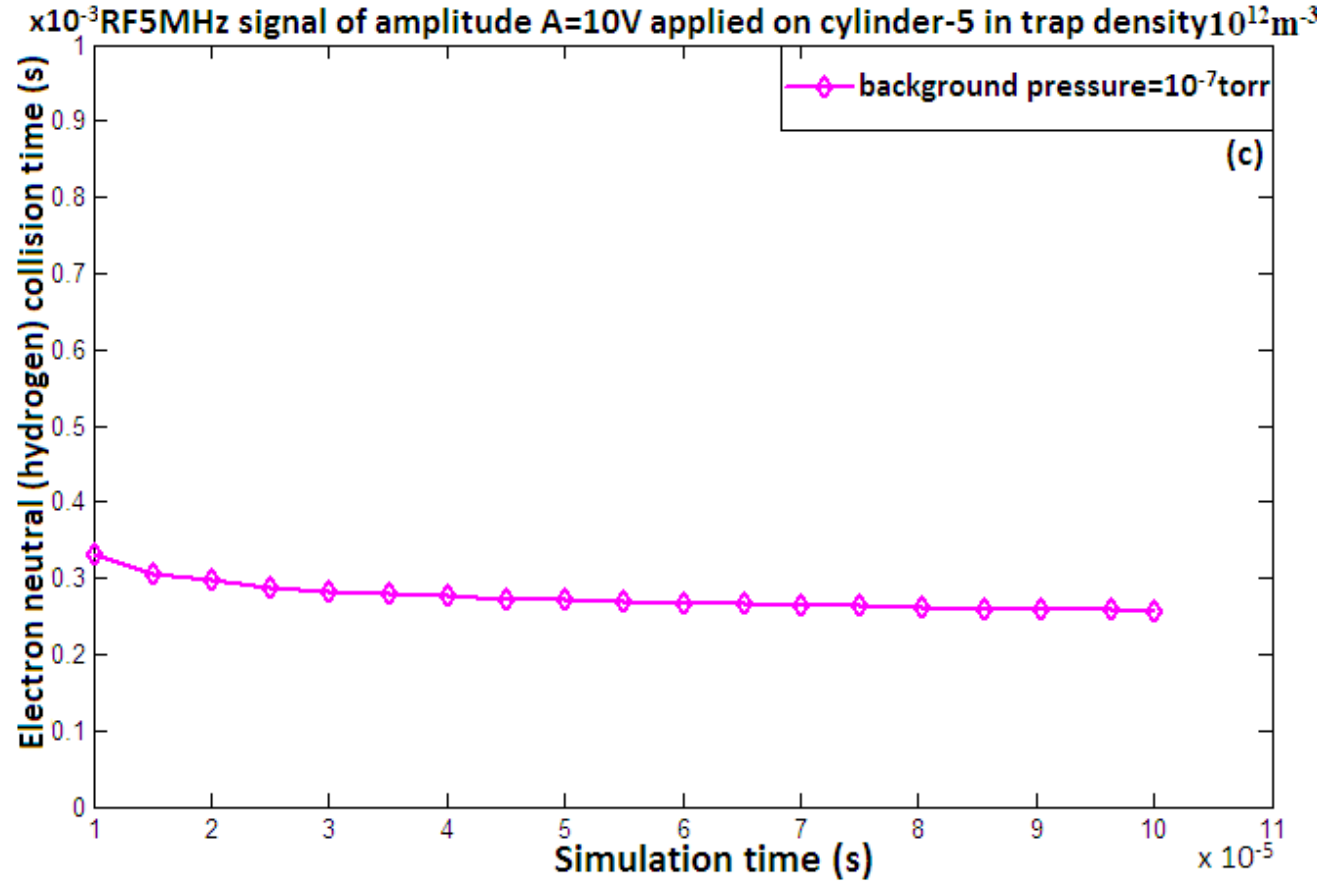

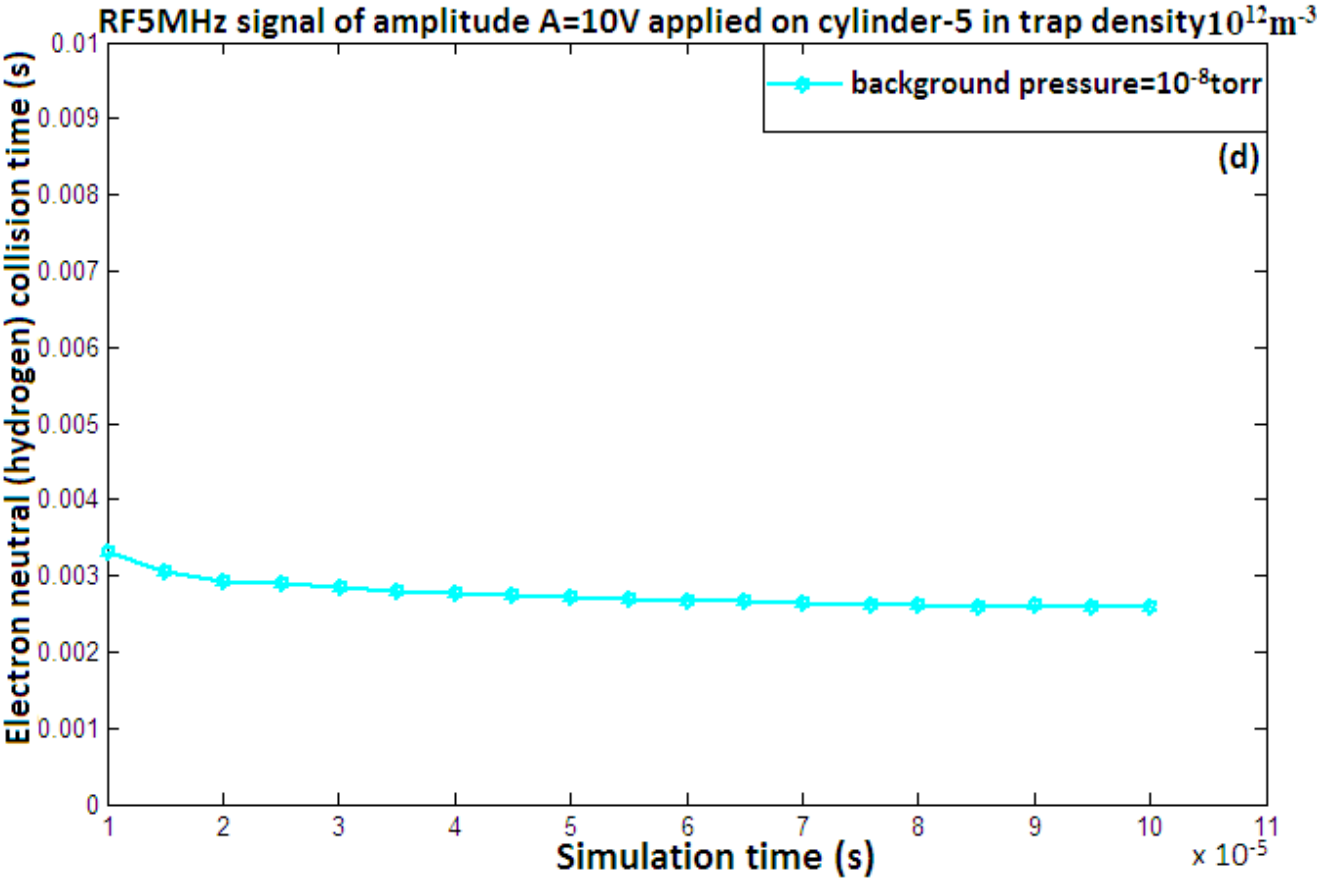

Figure 5.24 For the same data as in figure 5.23, electron neutral collision time vs. simulation time (s) at a pressure of (c) $10^{-7}\,torr$ **and (d)** $10^{-8}\,torr$ **.**

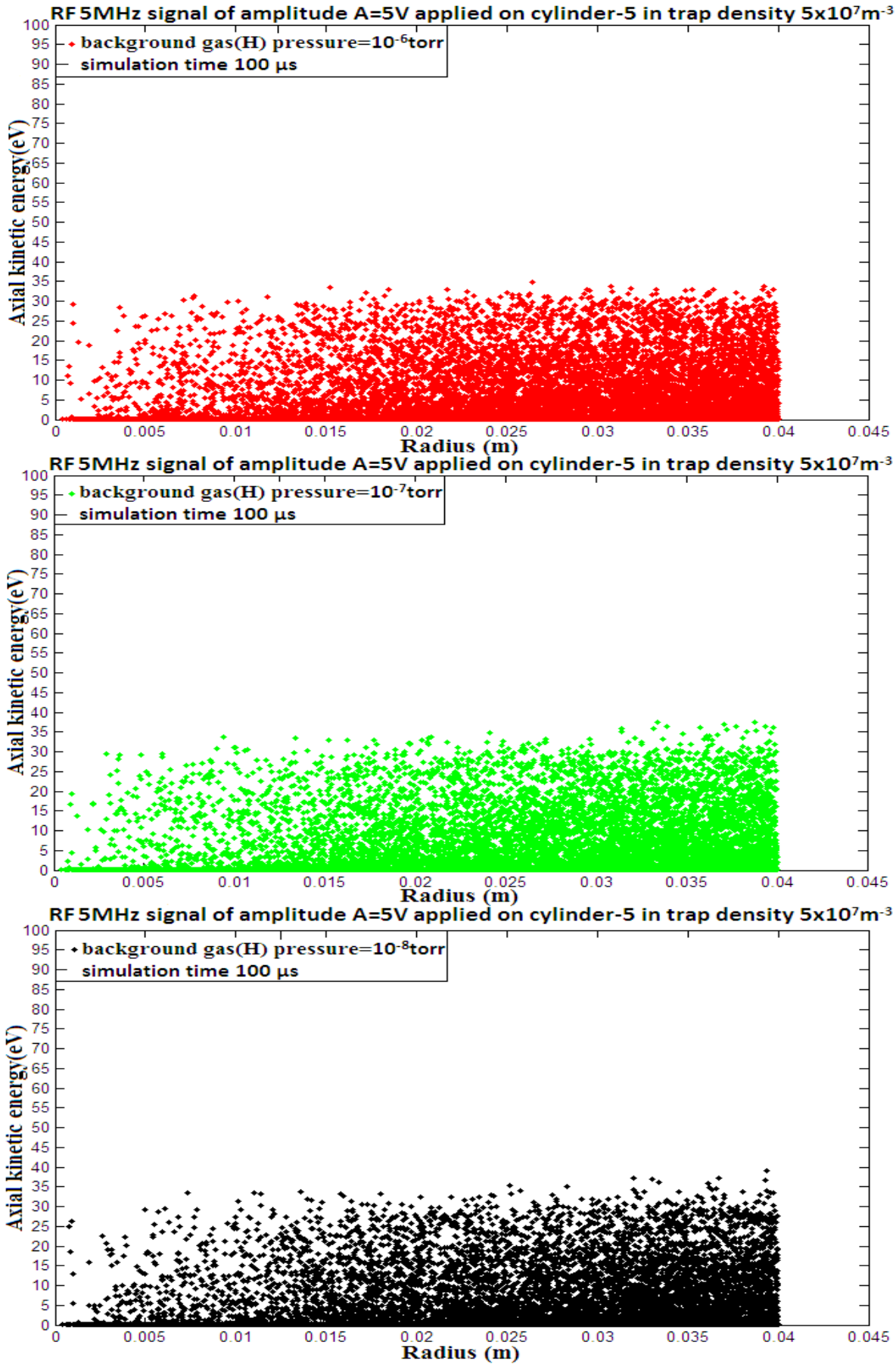

Figure 5.25 Axial kinetic energy (eV) vs radius (m) for an amplitude of the applied RF drive of 5V at 5 MHz frequency at a simulation time of $100\mu s$ for an electron density of $5\times10^{7}\,m^{-3}$.

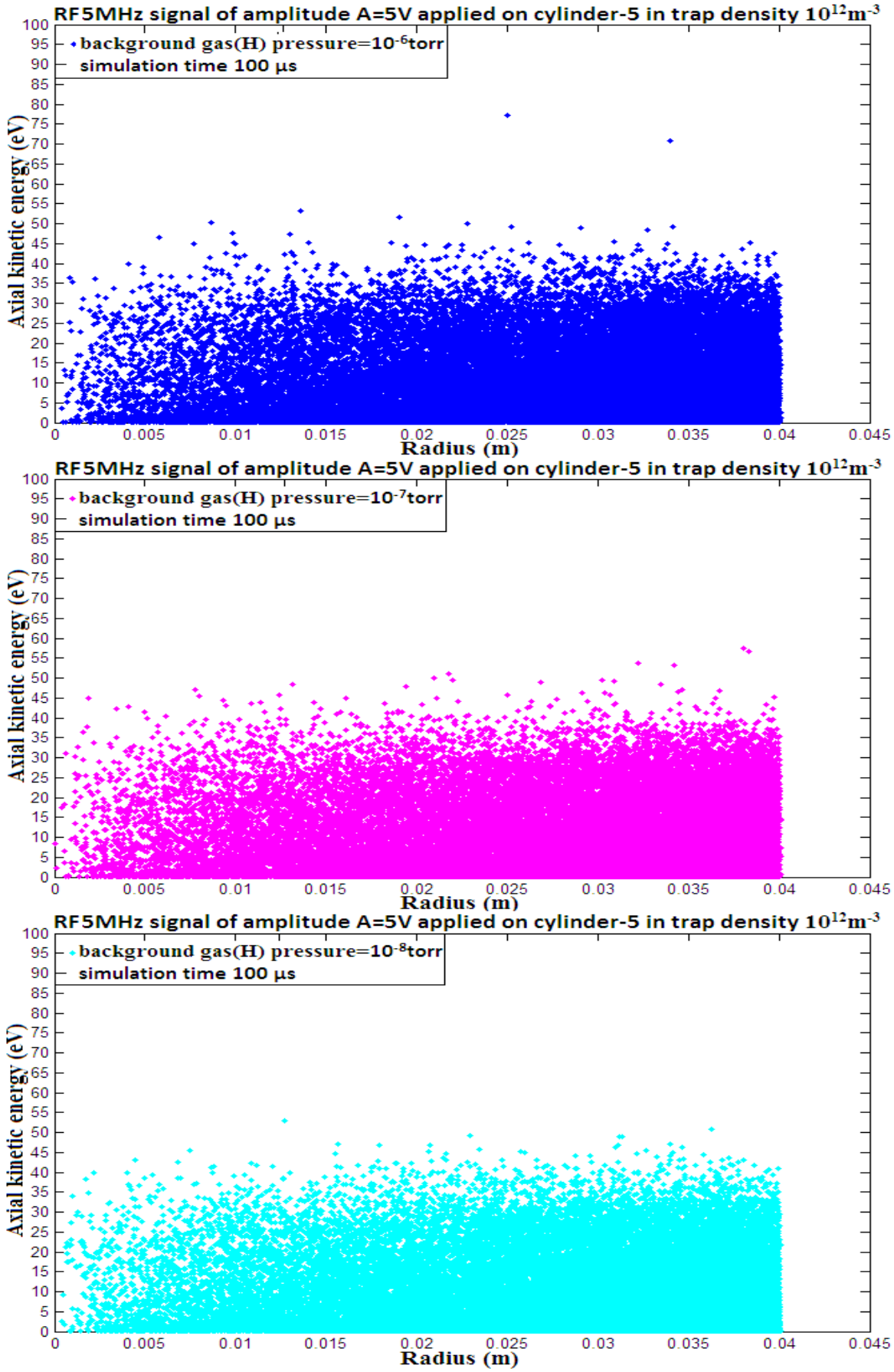

Figure 5.26 Axial kinetic energy (eV) vs radius (m) for an amplitude of the applied RF drive of 5 V at 5 MHz frequency at a simulation time of $100\mu s$ for an electron density of $10^{12}\,m^{-3}$.

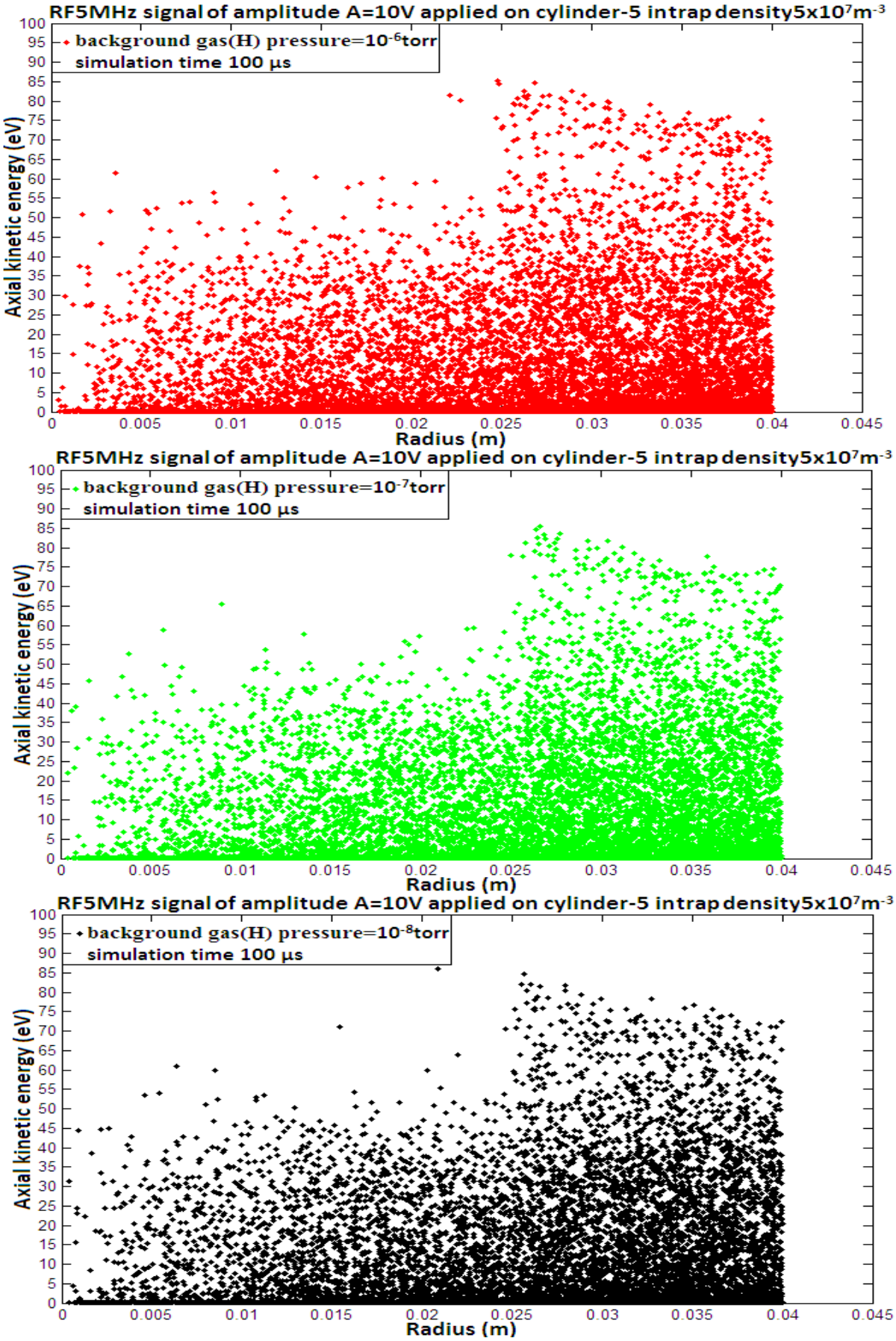

Figure 5.27 Axial kinetic energy (eV) vs radius (m) for an amplitude of the applied RF drive of 10 V at 5 MHz frequency at a simulation time of $100\mu s$ for an electron density of $5\times10^{7}m^{-3}$.

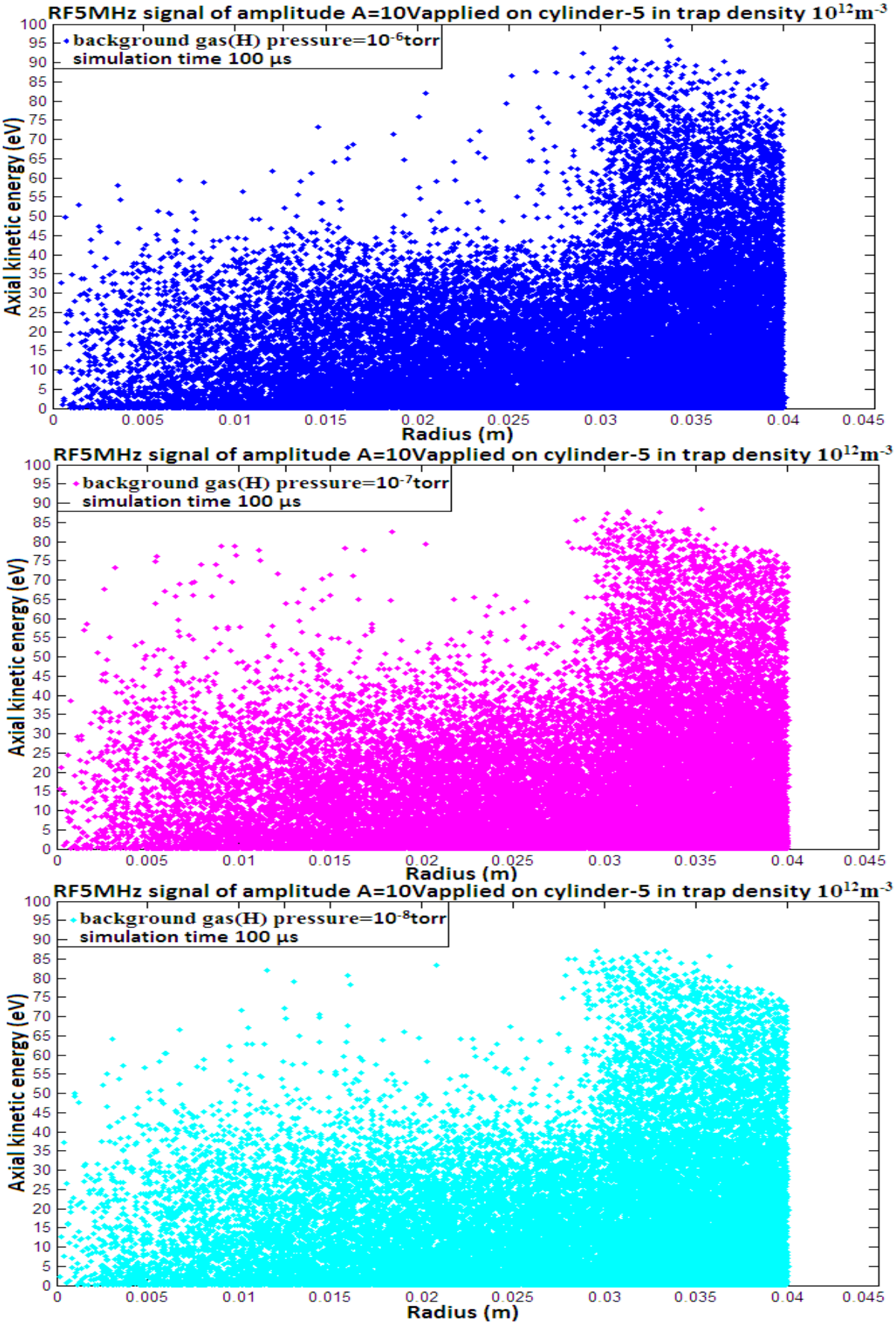

Figure 5.28 Axial kinetic energy (eV) vs radius (m) for an amplitude of the applied RF drive of 10 V at 5 MHz frequency at a simulation time of $100\mu s$ for an electron density of $10^{12}\,m^{-3}$.

Table 5.8 Monte-Carlo electrostatic PIC simulation of electron neutral collision. Summary of ionization, secondary electrons and losses at simulation time 100 µs. At t=0 the total number of macro-particles is 19478 and 37789 for density of (a) $5\times10^{7}\,m^{-3}$ and (b) $10^{12}\,m^{-3}$, respectively.

(a) Density $5\times10^{7}\,m^{-3}$, Input temperature= 0.01 eV

A volts	Pressure=$10^{-8}torr$			Pressure=$10^{-7}torr$			Pressure=$10^{-6}torr$		
	electrons losses	secondary electrons	ions	electrons losses	secondary electrons	ions	electrons losses	secondary electrons	ions
5	0	1	1	0	5	5	0	52	45
10	729	1	1	696	12	12	464	118	118

(b) Density $10^{12}\,m^{-3}$, Input temperature= 1 eV

A volts	Pressure=$10^{-8}torr$			Pressure=$10^{-7}torr$			Pressure=$10^{-6}torr$		
	electrons losses	secondary electrons	ions	electrons losses	secondary electrons	ions	electrons losses	secondary electrons	ions
5	4765	5	5	4760	18	18	4464	270	270
10	9017	3	3	8876	50	50	8545	481	481

5.7 Simulations of the ECRH in ELTRAP

As indicated previously, the available microwave generator has a range of 9 kHz - 3GHz, the maximum magnetic field is 0.2 T and the internal radius if the cylindrical electrodes of ELTRAP is 4.5 cm. Under these conditions, only $TE_{11}=1.9522\,GHz$ and $TM_{01}=2.5499\,GHz$ modes can be excited in ELTRAP.

In the electromagnetic simulations the same spatial grid (J=180, K=45) is used like in the electrostatic case but the time step is reduced to $10^{-12}\,s$ (1ps) for a better accuracy and to respect the Courant limit. The schematic diagram of the electromagnetic PIC simulations of the microwave electron heating is shown in figure 5.29.

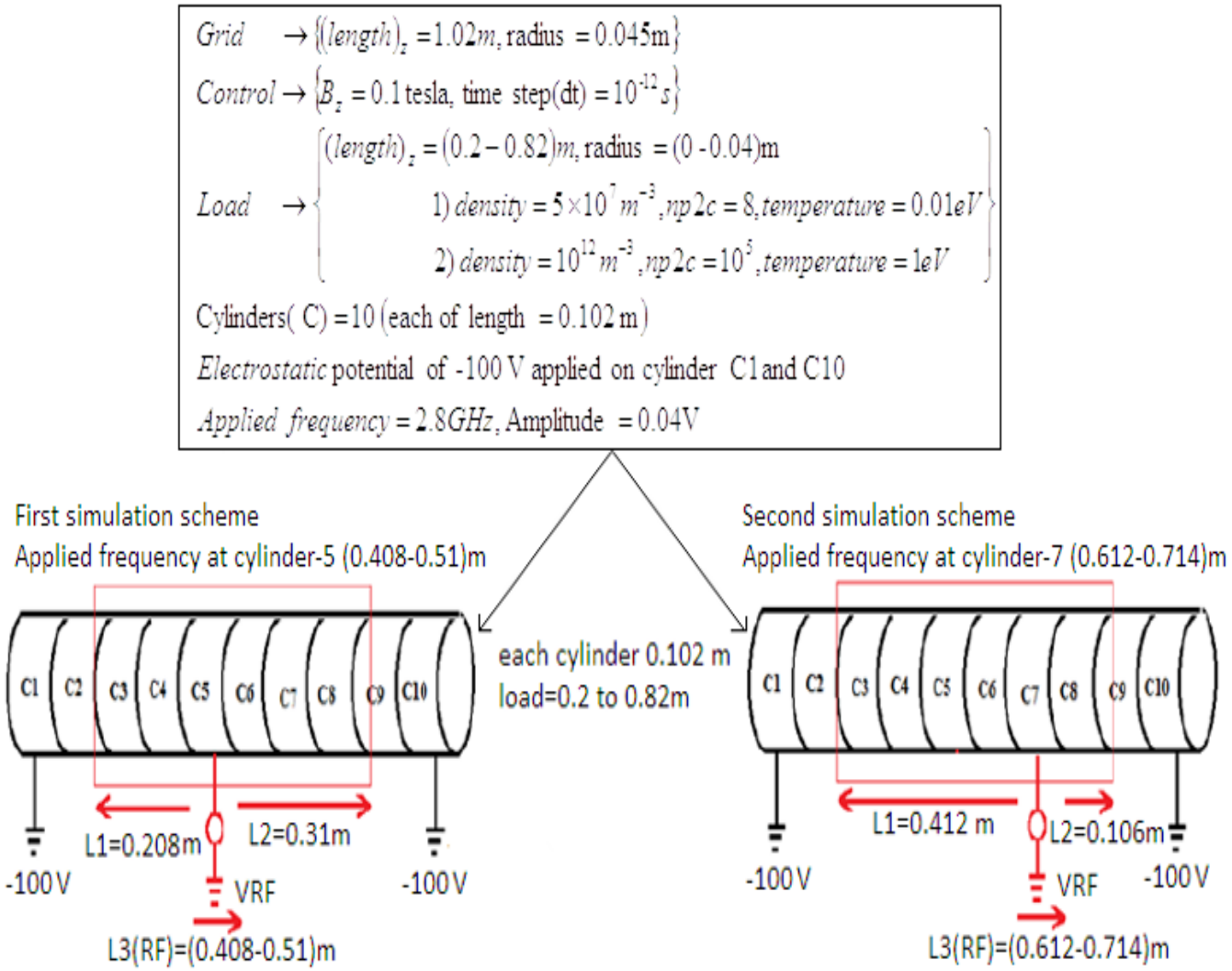

Figure 5.29 Schematic diagram of the electromagnetic PIC simulations of the microwave heating at 2.8 GHz for an electron plasma density of $n_e = 5\times10^7 m^{-3}$ and $10^{12} m^{-3}$.

The maximum power that can be transferred to the ELTRAP electrode stack (circular waveguide) operating with the TE_{11} mode with a 2.8 GHz frequency is:

$$P = 1.99\times10^{-3} a^2 \left(\frac{\lambda}{\lambda_g}\right) E_{\max}^2 \, watts \qquad 5.16$$

where the potential gradient E_{max} is expressed in volts per centimeter, and the power is in watt. As a=4.5 cm, the guide wavelength of the TE_{11} mode is $\lambda_g = \frac{2\pi(4.5)}{1.8412} = 15.356471\,cm$ and the free-space wavelength $\lambda = 10.706785\,\text{cm}$. Therefore the relation between the maximum power and maximum allowable field strength is

$$P = 0.0280961\, E_{\max}^2 \quad \text{watt} \qquad 5.17$$

The maximum field strength in the TE_{11} mode is on the axis and the value is $E_{\max} = 1.88658762$ volts/cm, when computed with the maximum power 20 dBm = 0.1 watt of the RF signal generator. Similarly the maximum power at 2.8 GHz for the TM_{01} mode is

$$P = 7.69 \times 10^{-3} \frac{a^4}{\lambda^2} \left(\frac{\lambda}{\lambda_g} \right) E_{\max}^2 \qquad 5.18$$

where $\lambda_g = \frac{2\pi(4.5)}{2.4049} = 11.756969\, cm$.

Therefore, $$P = 0.025051\, E_{\max}^2 \; watt \qquad 5.19$$

The maximum field strength in the TM_{01} mode is therefore $E_{\max} = 1.9979631$ volts/cm.

In the simulations, a continuous microwave signal of 0.04 V amplitude at 2.8 GHz is applied in the positions of the C5 and C7 cylinders. The simulations are run up to a time of 5μs and the data are saved in 12 dumps, where each dump corresponds to a time interval 5μs.

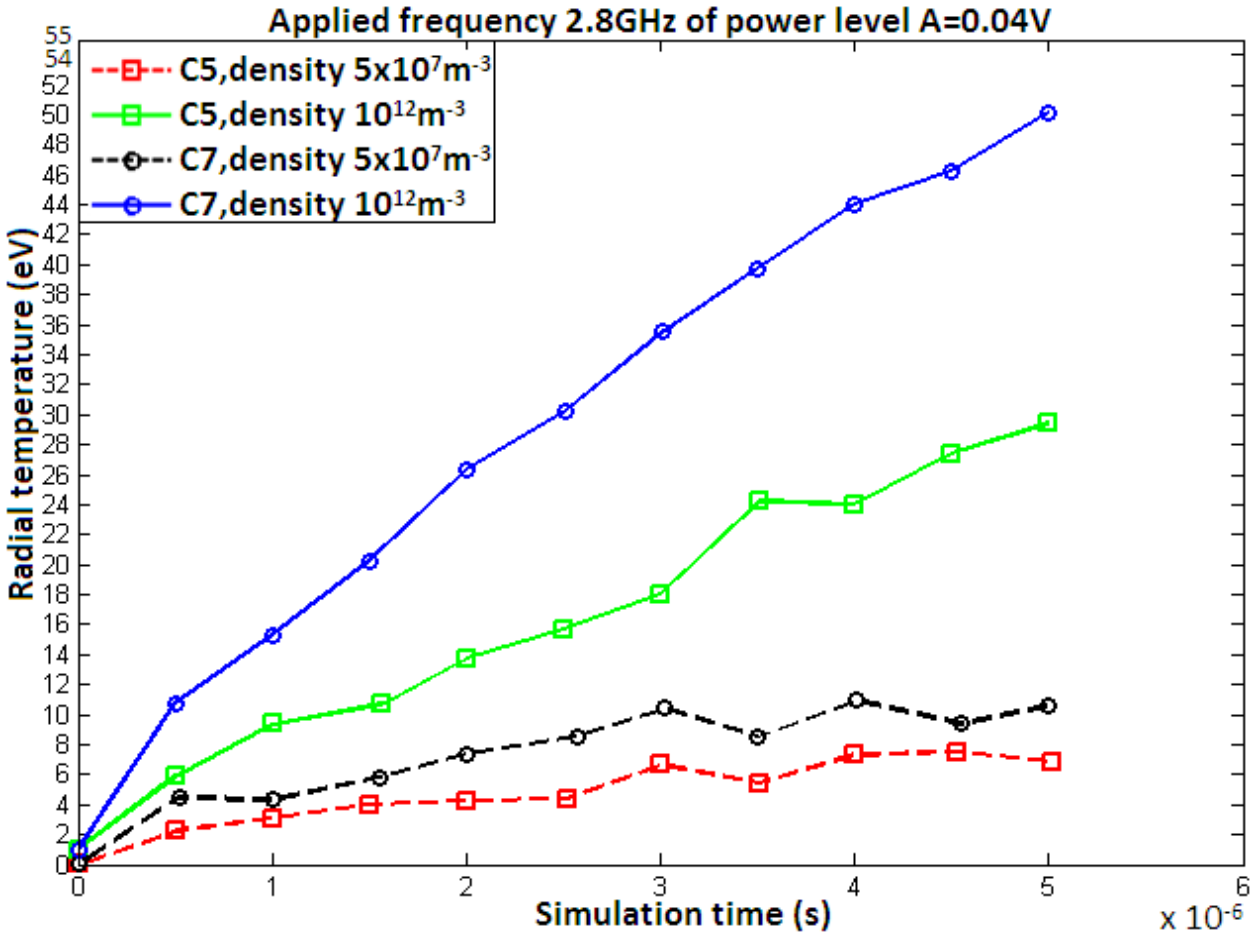

Figure 5.30 Electron radial kinetic energy (eV) vs time for the cases indicated in the legend. The RF frequency is 2.8 GHz.

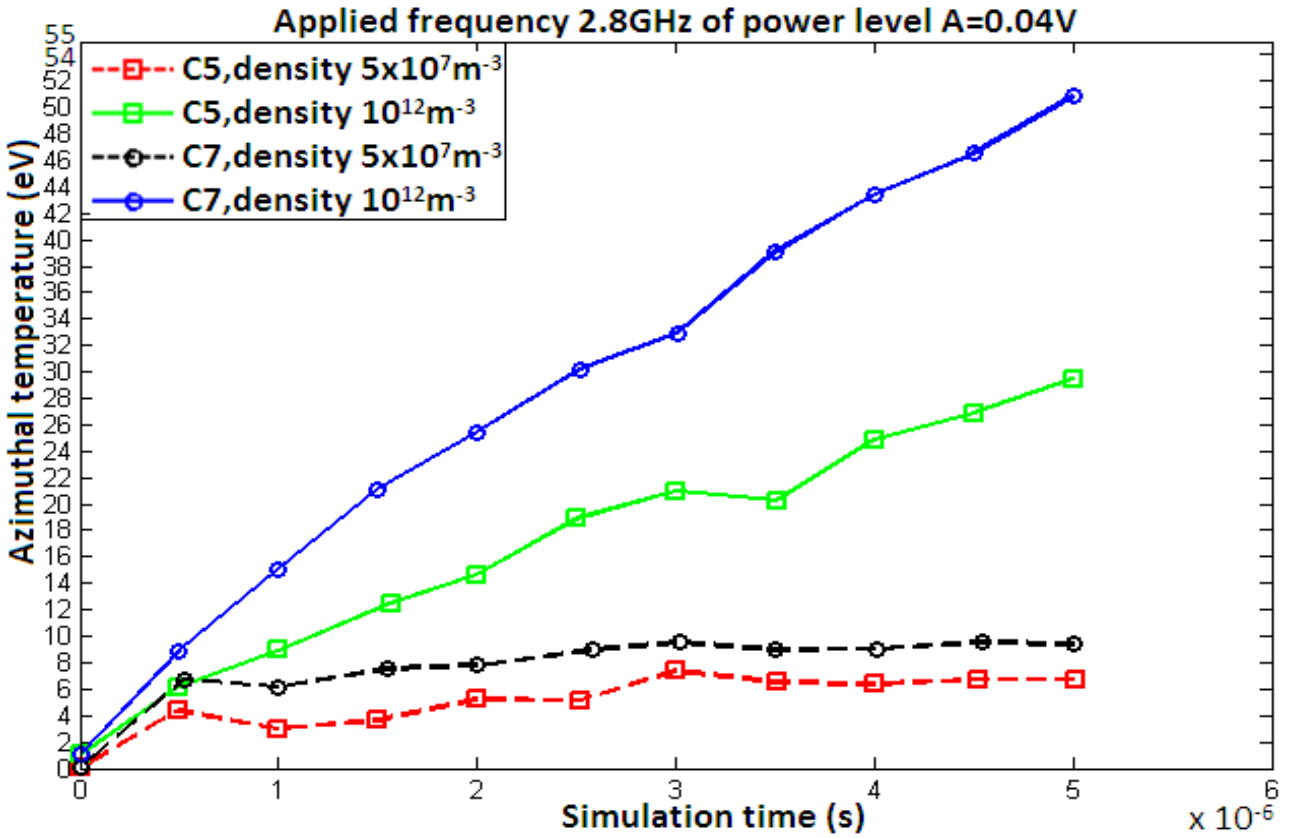

Figure 5.31 Electron azimuthal kinetic energy (eV) vs time for the cases indicated in the legend. The RF frequency is 2.8 GHz.

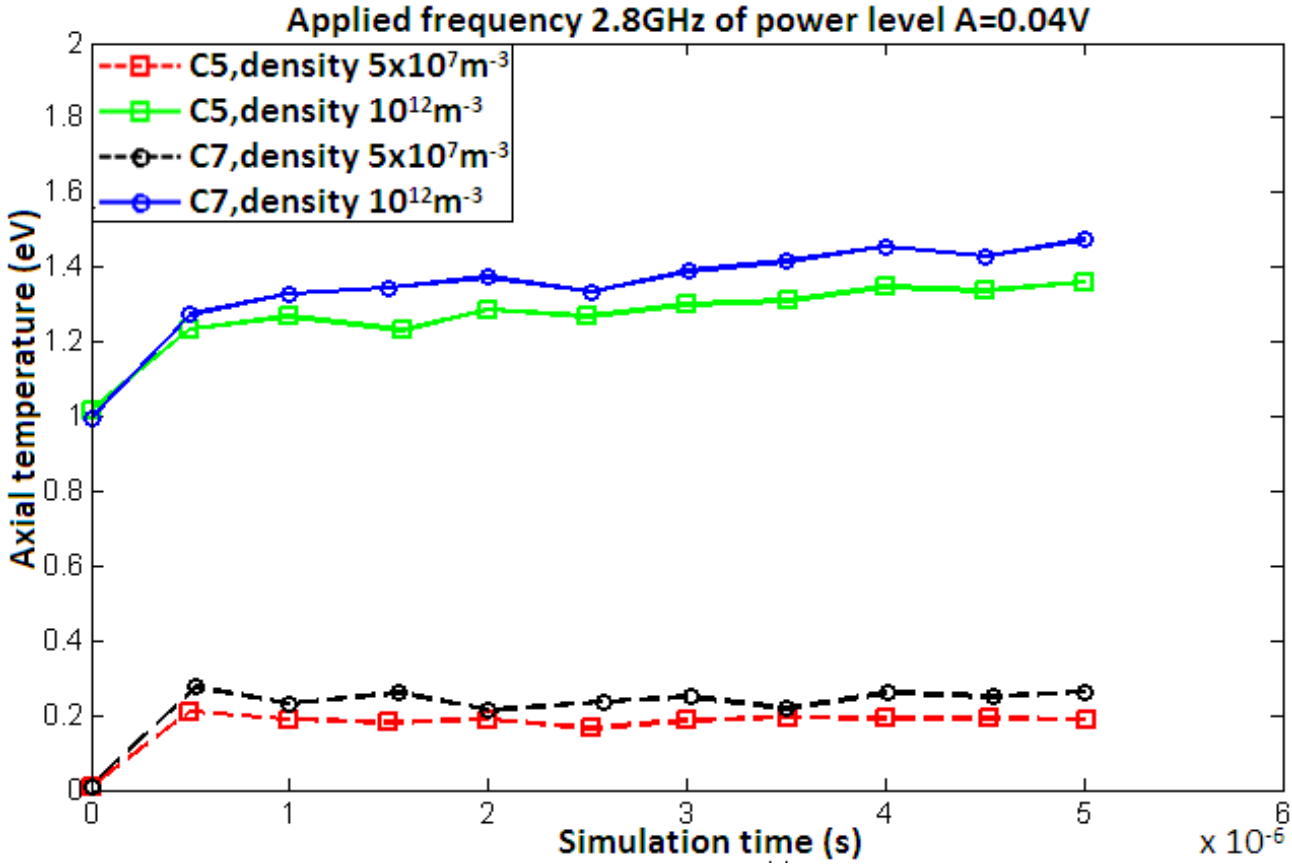

Figure 5.32 Electron axial kinetic energy (eV) vs time for the cases indicated in the legend. The RF frequency is 2.8 GHz.

The figures 5.30-5.32 show the time evolution of the electron kinetic energy computed with the various velocity components (radial, azimuthal, axial). Unlike in the electrostatic simulations, in this case the radial and azimuthal “temperatures” of the electrons is much higher as compared to the axial temperature. The major heating effect is obtained when the RF power is injected from the position of the C7 electrode, i.e., close to one end of the trap.

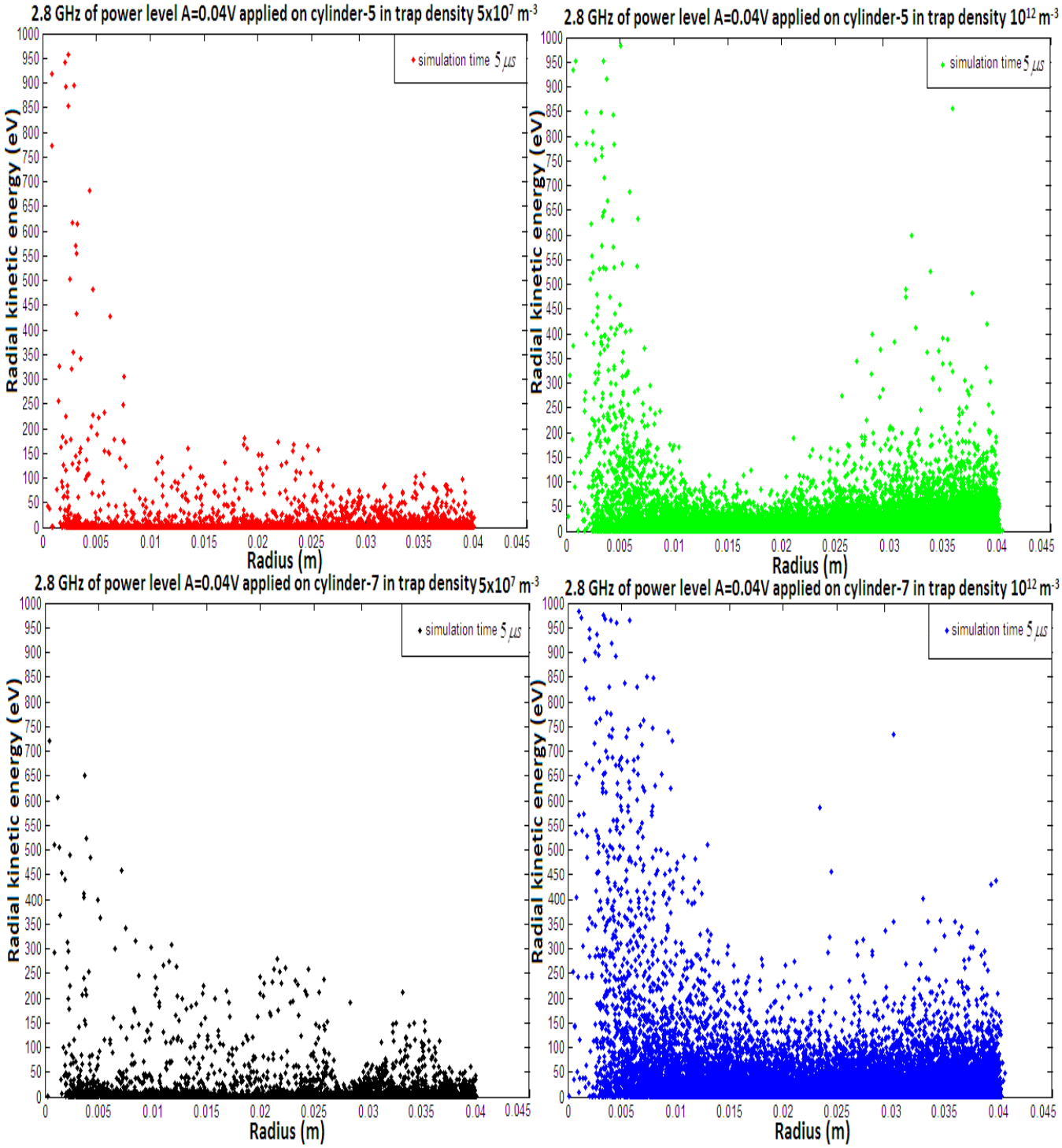

Figure 5.33 Radial kinetic energy distribution vs radius at the simulation time of 5µs.

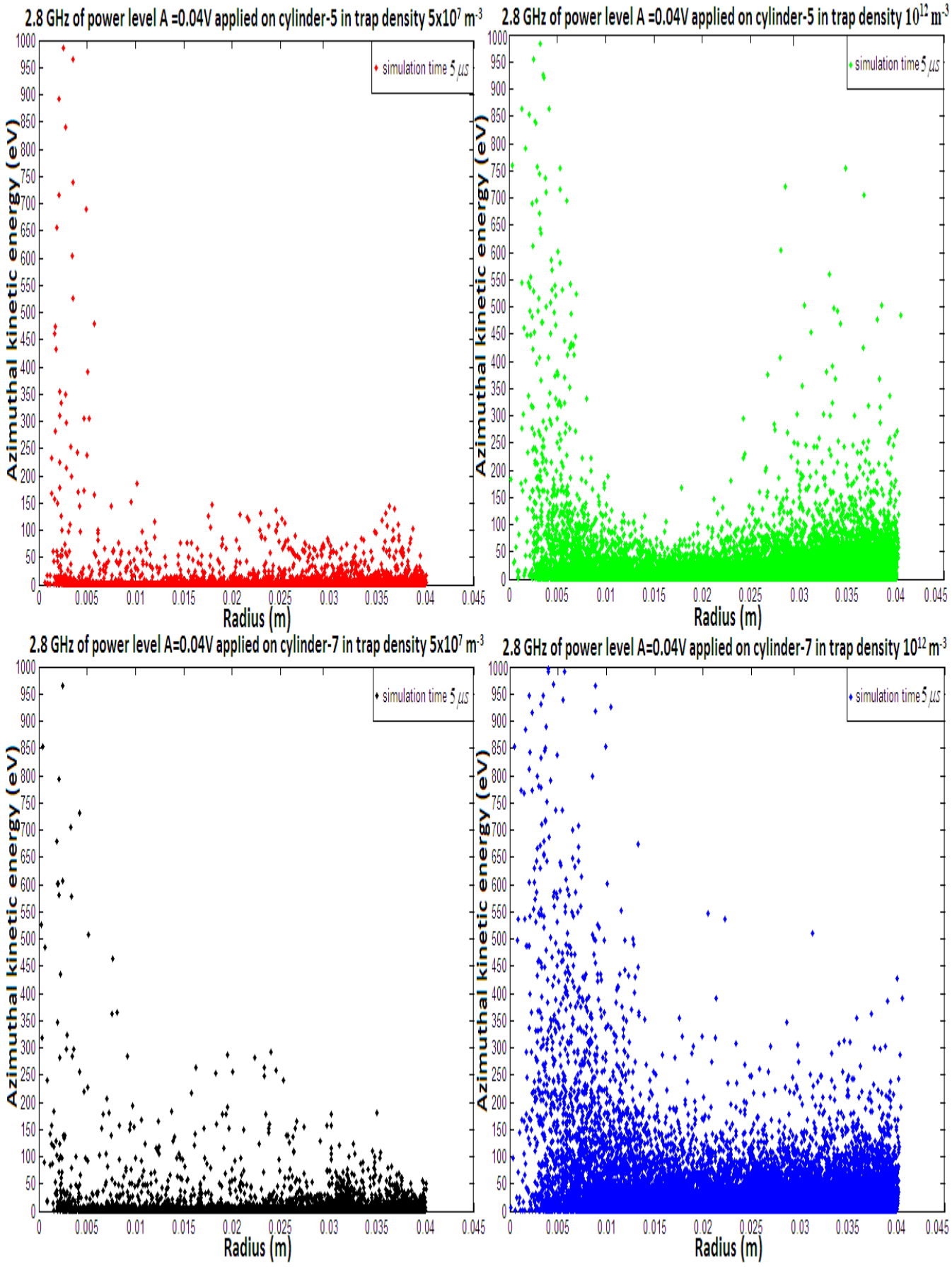

Figure 5.34 Azimuthal kinetic energy distribution vs radius at the simulation time of 5μs.

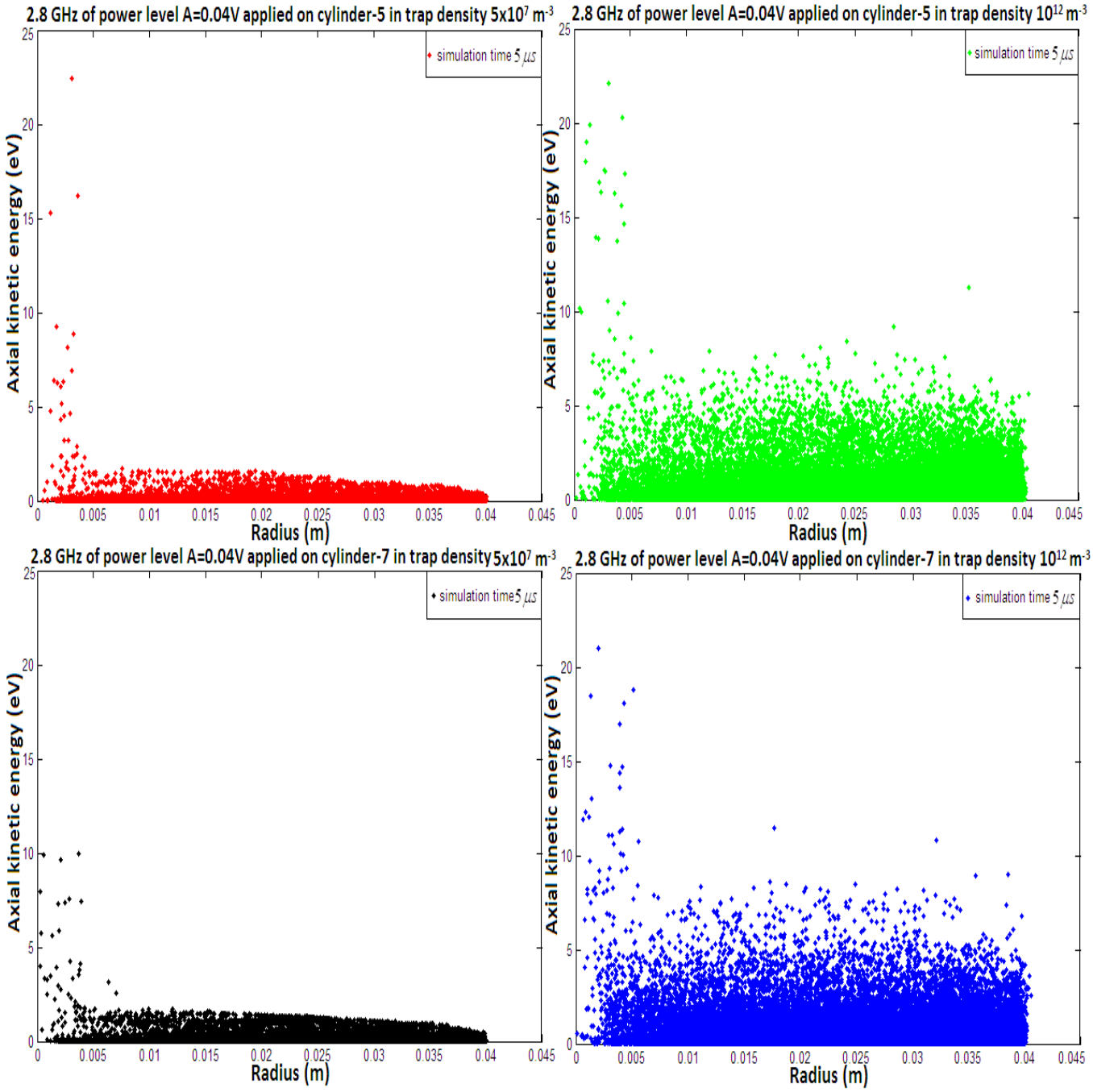

Figure 5.35 Axial kinetic energy distribution vs radius at the simulation time of 5μs.

Table 5.9 Details on number of macro-particles and losses for the electromagnetic simulations

Simulation density	Total number of simulation electrons at simulation time of $10^{-12}\,s$	Electron lost when C-5 (antenna) used for the RF excitation at simulation time of $5\mu s$	Electron lost when C-7 (antenna) used for the RF excitation at simulation time of $5\mu s$
$5\times10^{7}\,m^{-3}$	19478	0	0
$10^{12}\,m^{-3}$	31164	2	7

Table 5.10 Details on the electron energy distribution at the simulation time of 5μs for density of 5 x 10^{7} m^{-3}.

Energy range (eV)	**RF plugging at C5**			**RF plugging at C7**		
	Number of electrons(%) of $KE(u_r)$	Number of electrons(%) of $KE(u_{phi})$	Number of electrons(%) of $KE(u_z)$	Number of electrons(%) of $KE(u_r)$	Number of electrons(%) of $KE(u_{phi})$	Number of electrons(%) of $KE(u_z)$
0-20	19062 (97.864%)	19110 (98.11%)	19477 (99.995%)	18793 (96.483%)	18894 (97.002%)	19478 (100%)
20-70	270 (1.3862%)	243 (1.2475%)	01 (0.0051%)	451 (2.315%)	402 (2.0638%)	0 (0%)
70-100	52 (0.2669%)	46 (0.2362%)	0 (0%)	64 (0.3285%)	56 (0.2875%)	0 (0%)
≥ 100	94 (0.4826%)	79 (0.4056%)	0 (0%)	170 (0.8728%)	126 (0.64688%)	0 (0%)
Total (No,%)	19478 (100%)	19478 (100%)	19478 (100%)	19478 (100%)	19478 (100%)	19478 (100%)

Table 5.11. Details on the electron energy distribution at the simulation time of 5µs for density of 10^{12} m^{-3}.

Energy range (eV)	RF plugging at C5			RF plugging at C7		
	Number of electrons(%) of $KE(u_r)$	Number of electrons(%) of $KE(u_{phi})$	Number of electrons(%) of $KE(u_z)$	Number of electrons(%) of $KE(u_r)$	Number of electrons(%) of $KE(u_{phi})$	Number of electrons(%) of $KE(u_z)$
0-20	26582 (85.297%)	26705 (85.692%)	31159 (99.984%)	24037 (77.131%)	23691 (76.02%)	31154 (99.968%)
20-70	3513 (11.273%)	3416 (10.961%)	03 (0.0096%)	4842 (15.5372%)	5133 (16.471%)	03 0.00903
70-100	420 (1.3477%)	434 (1.3926%)	0 (0%)	859 (2.7564%)	856 (2.7467%)	0 (0%)
≥100	647 (2.076%)	607 (1.9477%)	0 (0%)	1419 (4.5533%)	1477 (4.7394%)	0 (0%)
Total (No,%)	31162 (99.99358%)	31162 (99.99358%)	31162 (99.99358%)	31157 (99.9775%)	31157 (99.9775%)	31157 (99.9775%)

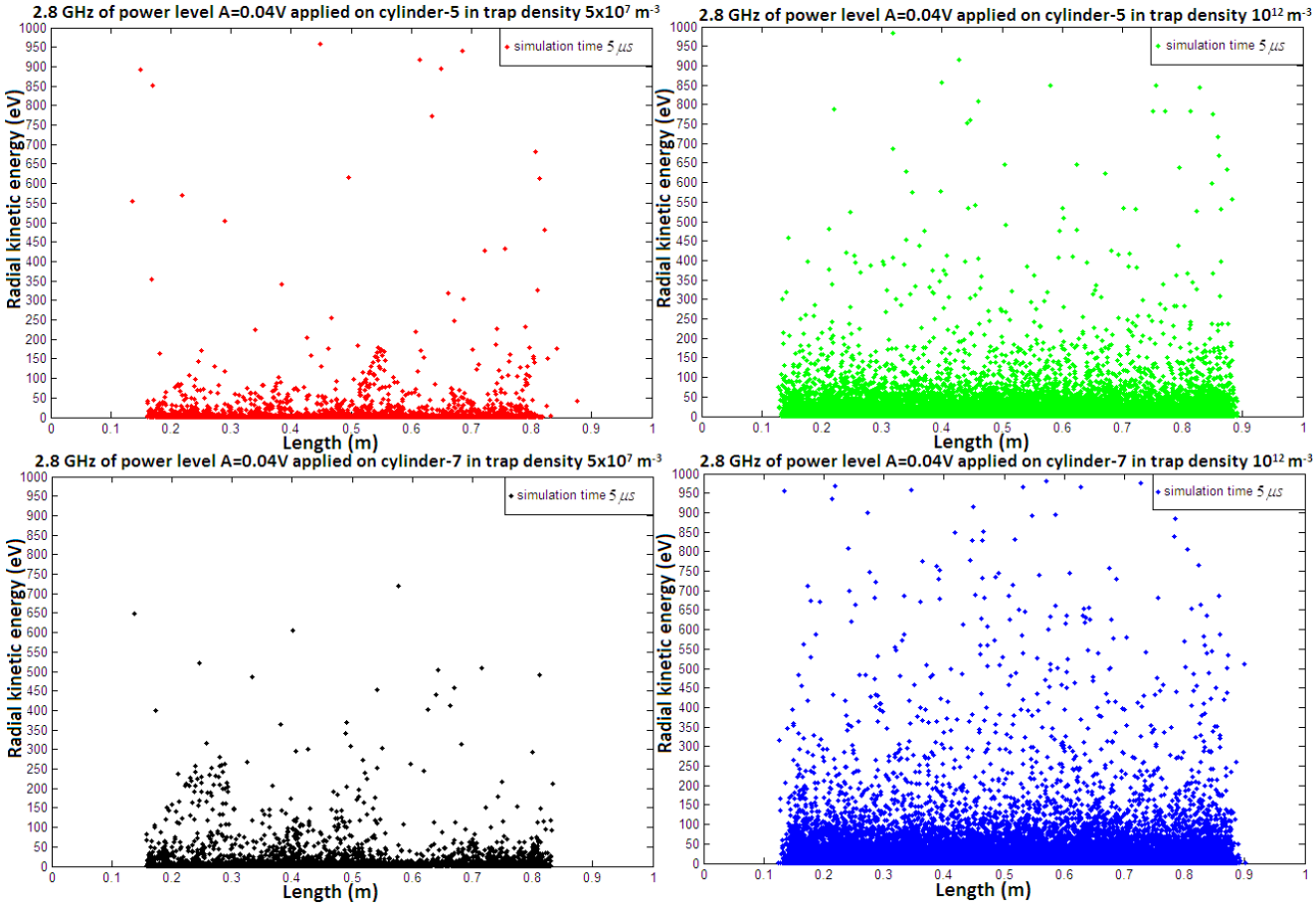

Figure 5.36 Radial kinetic energy distribution vs z at the simulation time of 5µs.

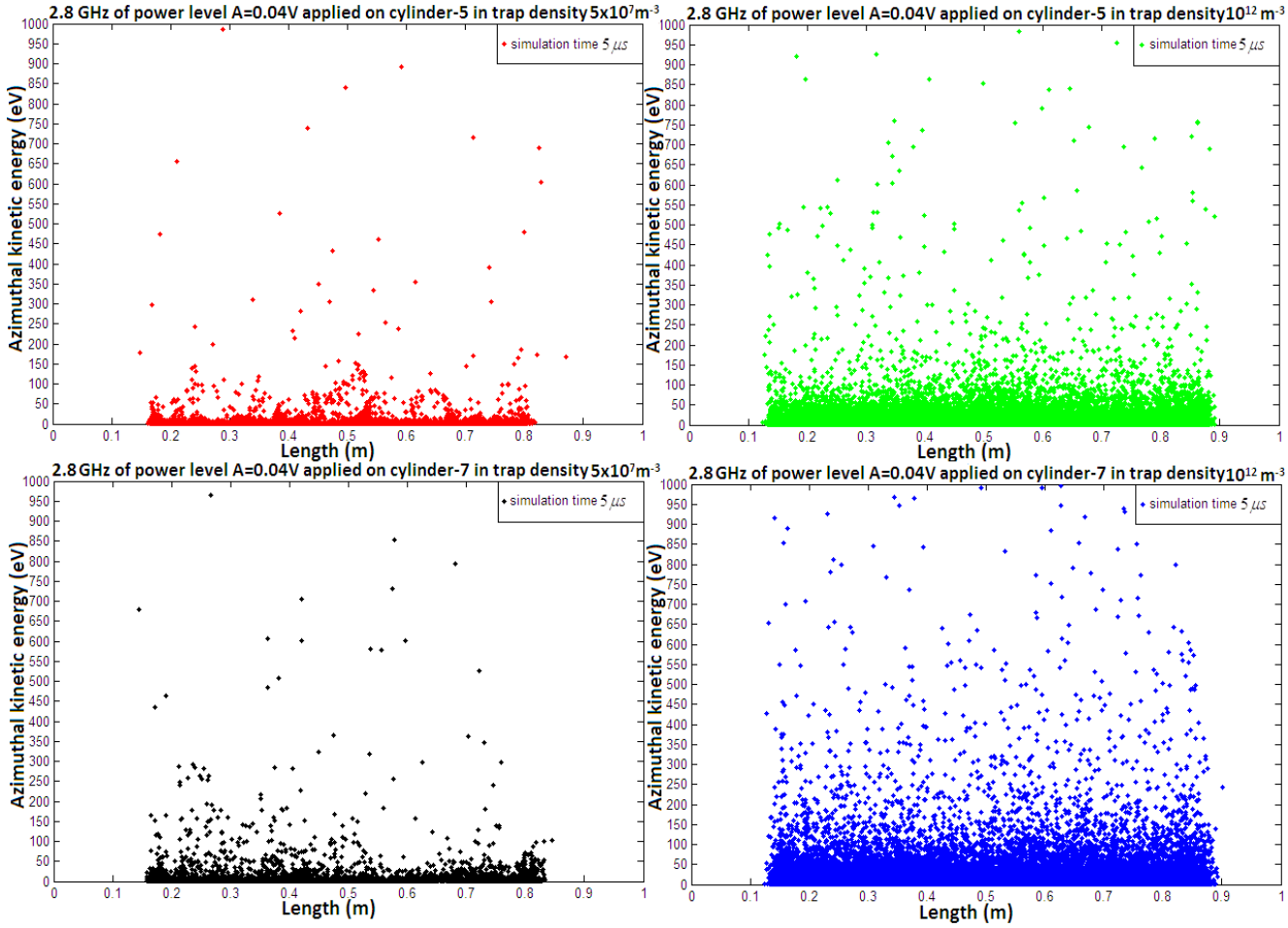

Figure 5.37 Azimuthal kinetic energy distribution vs z at the simulation time of 5μs.

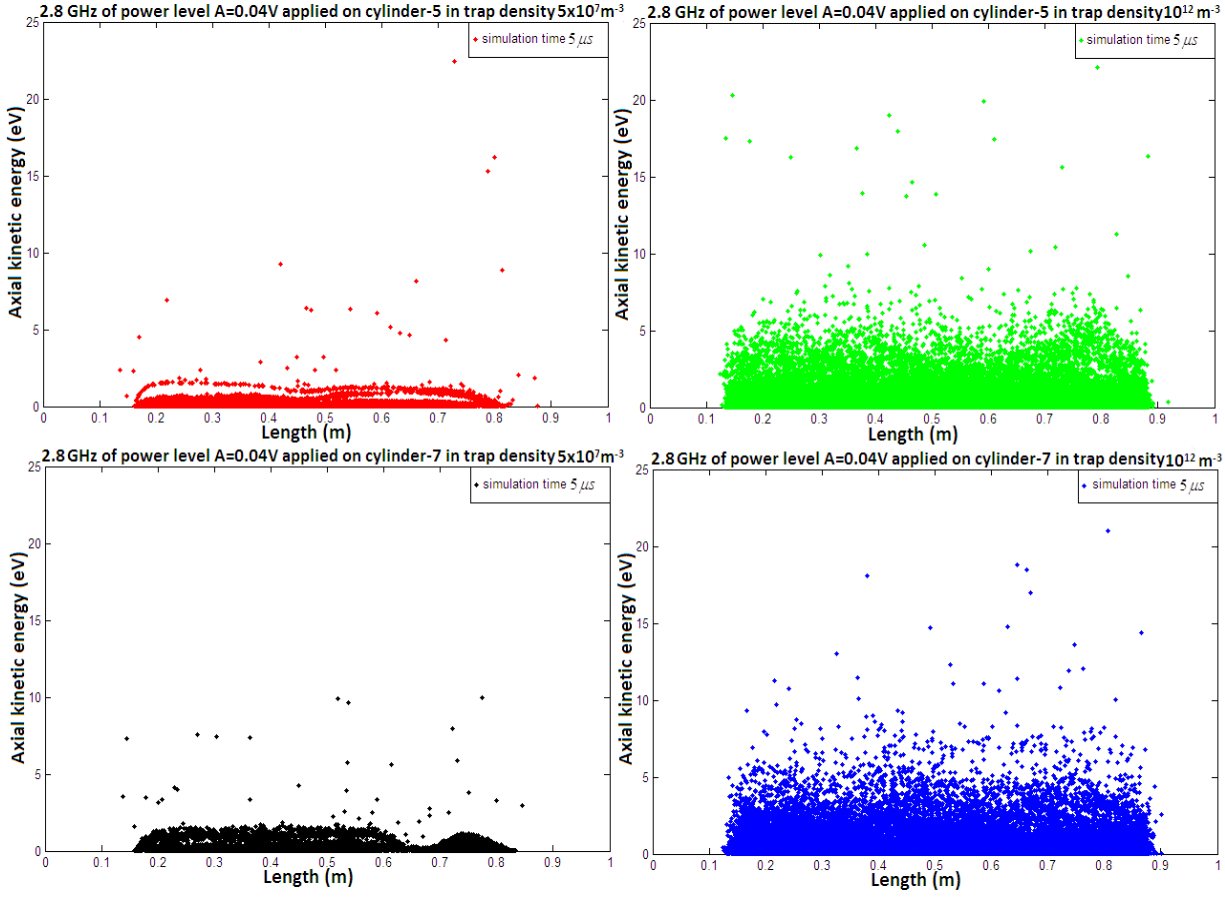

Figure 5.38 Axial kinetic energy distribution vs z at the simulation time of 5μs.

The radial distributions of the electron kinetic energy computed with the various velocity components are shown in figures 5.33-5.35 and the energy distribution of the electrons is indicated in tables 5.10 and 5.11. The results show that energetic electrons and higher heating are located in the central part of the trap, and that they will able to ionize the residual background gas, in order to increase the overall electron plasma density.

Chapter SIX

Summary

One of the objectives of this research work was to estimate the sensitivity of the system installed in the ELTRAP device to perform a Thomson backscattering experiment (discussed in chapter 2). The reachable electron bunch density ($n_b = 4.3\times10^{8} cm^{-3}$) does not allow one to obtain a detectable signal from the laser bunch interaction (with the present setup the minimum density should be $n_e = 3.6\times10^{10} cm^{-3}$). Solutions to increase the signal level and to reduce the noise issues are briefly discussed in chapter 2.

The generation of an electron plasma was realized in ELTRAP under ultra-high vacuum conditions by means of the application of low power RF (1-20 MHz) drives on one of the azimuthally sectored electrodes of the trap. The relevant experimental results have been reviewed in chapter 3.

To investigate the characteristics of the electron heating, electrostatic simulations have been performed using a two- dimensional particle-in-cell code and a realistic geometry of the apparatus (chapter 5). Different excitation frequencies (1 MHz, 5 MHz, 6 MHz, 8 MHz, 10 MHz and 15 MHz) and amplitudes (5 V and 10 V) of the RF drive have been considered. In order to simulate the application of the RF drive in the middle of the trap or close to one of the plug cylinders, the simulations have been performed applying the RF excitation on cylinders C5 and C7. At low electron plasma density ($n_e = 5\times10^{7} m^{-3}$), simulating a situation of electron heating prior to the main plasma formation, the simulations show that the axial temperature of the confined electrons increase with the applied excitation frequency from 1 MHz to 5-6 MHz, while it decreases with a further increase of the excitation frequency (from 8 MHz to 15 MHz). In addition, for given excitation frequency and amplitude, the axial electron temperature turns out to be higher when the RF drive is applied close to one end of the trap. The results for the radial profiles of the electron axial kinetic energy indicate that the electron heating is initially stronger close to the wall of the trap. Later the heating effect is extended towards the central region of the trap. The electrons localized near to wall having higher energy (≥ 20 eV) would then be able to ionize the

residual gas better than the electrons located close to the central part of the trap, and this results is in agreement with the experimental findings (plasma formation close to the wall, evidenced with the optical diagnostics of ELTRAP). Similar results are obtained for an electron plasma density of $10^{12}\,m^{-3}$, simulating a situation in which the RF is applied to an already formed plasma.

Simulations with a residual hydrogen gas have been also performed (at pressures 10^{-8} torr, 10^{-7} torr and 10^{-6} torr) using the same electron plasma densities, in order to investigate the importance of the ionization process. These Monte Carlo simulations are computationally expensive, so the considered final time is shorter than in the simulations performed in the absence of a residual background gas. The results are therefore also more qualitative, and show in particular that an increased collision frequency is obtained at higher RF drive amplitudes due to the higher electron temperature obtained, so that more ionization and secondary electrons are generated. At increasing pressures, electron–neutral collisions will become the dominant factor causing plasma expansion (the expansion rate is expected to increase linearly with the background gas pressure).
In the prospected solution to extend the RF studies to the GHz range, a bench test analysis has been performed of the RF transmission efficiency of a RF injection system up to a few GHz (chapter 4). Using a prototype circular waveguide with the same diameter and length of the ELTRAP electrode stack, it has been shown that a rectangular waveguide of dimensions a = 7.18 cm, b = 3.71 and length = 31 cm would satisfy the desired specifications for reflection and bandwidth. It has been computed in particular that 25.727 % of the working frequency band (from 2 GHz to 3 GHz) has a transmission of at least 50 %, and the maximum value of transmission occurs at a frequency of ≈ 3 GHz. The length of the rectangular waveguide must be reduced from the optimum one (31 cm) to 7 cm, taking into account the geometrical constraints of the vacuum chamber of the ELTRAP apparatus. The return loss measurements of the adopted final configuration (figure 4.17) presented in figure 4.20 indicate that a frequency band of 35% can be obtained with a transmission of at least 50 % at about 2.6 GHz and a frequency band of 20.4 % with a transmission of at least 75 % at about 2.7GHz. The T-junction between the rectangular waveguide and the electrode stack of ELTRAP will be located close to one end of the stack, in order to reduce the perturbation on the confining potential of the electron plasma. It has also been shown in figure 4.23 that the useful frequency band is reduced, when the length of the prototype circular waveguide is increased on the side close to the junction with the rectangular waveguide (see also figures 4.15 and 4.16). Therefore, the location of the T-junction at one end of the trap has also the advantage of a larger useful transmission frequency band.

Electromagnetic PIC simulations have been performed of the ECRH heating in ELTRAP. The generation of a 2.8 GHz signal from a cylindrical antenna (simulating the real situation of the injection into the electrode stack of ELTRAP of a microwave signal from an external rectangular waveguide) has been considered. Unlike in the electrostatic simulations, in this case the radial and azimuthal “temperatures” of the electrons increase much more than the axial temperature. The major heating effect is obtained when the RF power is injected from the position of the C7 electrode, i.e., close to one end of the trap.

The new microwave heating system will therefore allow the extension of the previous RF studies to the GHz range. In particular, resonant cyclotron excitation of the RF-generated plasma will be aimed to increasing the electron temperature and possibly density as a consequence of a higher ionization rate of the residual gas. The installation of the new RF system will open up the possibility to study, e.g., the interaction between the confined plasma and a traveling electron bunch.

Bibliography

1. R. C. Davidson, *Physics of Nonneutral Plasmas* (Imperial College Press and World Scientific, 2001).
2. R. C. Davidson, *Theory of Nonneutral plasmas* (Benjamin, Reading, Massachusetts, 1974)
3. R. C. Davidson and N. A. Krall, Phys. Rev. Lett. **22**, 833 (1969).
4. T. M. O'Neil, Physica Scripta **T59,** 341 (1995).
5. T. M. O'Neil, Phys. Fluids **23**, 2216 (1980).
6. T. M. O'Neil and D. H. E. Dubin, Phys. Plasmas **5**, 2163 (1998)
7. D. H. E. Dubin and T. M. O'Neil, Rev. Mod. Phys. **71**, 87 (1999).
8. T. M. O'Neil, Comm. Plasma Phys. Control. Fusion **5**, 231 (1980).
9. T. M. O'Neil, Phys. Fluids **23**, 2216 (1980).
10. T. M. O'Neil, Phys. Rev. Lett. **55**, 943 (1985).
11. T. M. O'Neil in *Nonneutral Plasma Physics*, AIP Proc. **175**, ed. by C. W. Roberson and C. F. Driscoll (American Institute of Physics, New York, 1988).
12. R. W. Gould, Phys. Plasmas **2**, 2151 (1995).
13. R. C. Davidson and H. Qin, *Physics of Intense Charged Particle Beams in High Energy Accelerators* (Imperial College Press and World Scientific, 2001).
14. R. C. Davidson, H. Qin and G. Shvets, Phys. Plasmas **7**, 1020 (2000).
15. R. C. Davidson and H. Qin, Phys. Rev. ST Accel. & Beams **8**, 064201 (2005).
16. J. H. Malmberg and J. S. deGrassie, Phys. Rev. Lett., **35**, 577 (1975).
17. C. F. Driscoll, J. H. Malmberg and K. S. Fine, Phys. Rev. Lett. **60**, 1290 (1988).
18. C. F. Driscoll, K. S. Fine and J. H. Malmberg, Phys. Fluids **29**, 2015 (1986).
19. G. Gabrielse, L. Haarsma and S. L. Rolston, Int. J. Mass Spec. **88**, 319 (1989).
20. L. S. Brown and G. Gabrielse, Rev. Mod. Phys. **58**, 233 (1986).
21. S. Choroba, *RF Transport, CERN School on High Power Hadron Machines*, 25 May - 02 June 2011, Bilbao, Spain.
22. F. G. Major, V. N. Gheorghe and G. Werth, *Charged Particle Traps Physics and Techniques of Charged Particle Field Confinement* (Springer-Verlag, Germany, 2005).
23. D. L. Eggleston, C. F. Driscoll, B. R. Beck, A. W. Hyatt and J. H. Malmberg, Phys. Fluids B **4**, 3432 (1992).
24. R. G. Greaves and C. M. Surko, Phys. Plasmas **4**, 1528 (1997).

25. B. Paroli, F. De Luca, G. Maero, F. Pozzoli, and M. Romé, Plasma Sources Sci. Technol. **19**, 045013 (2010).
26. R. E. Collin, *Foundation of Microwave Engineering*, second edition (McGraw-Hill, New York, 1992).
27. F. H. Harlow, *A machine calculation method for hydrodynamic problems*, Los Alamos Scientific Laboratory Report (1956).
28. H. M. Mayer, *Measurements with a wide-band probe*, Proceedings of the 6th Int. Conference on Ionization Phenomena in Gases, Vol. 4, 129 (1964).
29. Y.-K. Kim et al., Electron-Impact Ionization Cross Section for Ionization and Excitation Database (2004) [available online at http://physics.nist.gov/ionxsec]
30. O. Buneman, *Fast numerical procedures for computer experiments on relativistic plasmas, Relativistic Plasmas* (The Coral Gables Conference) (Benjamin, New York, 1968).
31. G. Bettega, F. Cavaliere, B. Paroli, M. Cavenago, R. Pozzoli M. and Romé, Phys. Plasmas **14**, 102103 (2007).
32. G. Bettega, B. Paroli, R. Pozzoli and M. Romé, J. Appl. Phys. **105**, 053303 (2009).
33. W. D. White, J. H. Malmberg and C. F. Driscoll, Phys. Rev. Lett. **49**, 1822 (1982).
34. O. Buneman, *Experiments with a large 3-d, e-m particle code*, Bulletin of the American Physical Society **20**, 1328 (1975).
35. O. Buneman, Comp. Phys. Comm. **12**, 21 (1976).
36. O. Buneman, C. W. Barnes, J. C. Green and D. E. Nielsen, J. Comp. Phys. **38**, 1 (1980).
37. C. K. Birdsall, IEEE Trans. Plasma Sci. **19**, 65 (1991).
38. V. Vahedi, G. Di Peso, C. K. Birdsall, M. A. Lieberman, and T. D. Rognlien, Plasma Sources Sci. Technol. **2**, 261 (1993).
39. T. Moreno, *Microwave transmission design data*, first edition (Dover, New York, 1948).
40. N. Marcuvitz, *Waveguide Handbook*, MIT Radiation Laboratory Series Vol. **10** (McGraw Hill, New York, 1951).
41. H. J. Reich, P. F. Ordung, H. L. Krauss and J. G. Skalnik, *Microwave Theory and Techniques* (D. van Nostrand, 1953).
42. D. M. Pozar, *Microwave Engineering* (Wiley, 2004).
43. J. Notte, A. J. Peurrung, J. Fajans, R. Chu and J. S. Wurtele, Phys. Rev. Lett. **69**, 3056 (1992)
44. J. S. deGrassie and J. H. Malmberg, Phys. Rev. Lett. **39**, 1077 (1977).
45. S. A. Prasad and T. M. O'Neil, Phys. Fluids **22**, 278 (1979).
46. J. H. Malmberg and C. F. Driscoll, Phys. Rev. Lett. **44**, 654 (1980).
47. J. S. deGrassie and J. H. Malmberg, Phys. Fluids **23**, 63 (1980).

48. S. A. Prasad and T. M. O'Neil, Phys. Fluids **26**, 665 (1983).
49. J. H. Malmberg, C. F. Driscoll and W. D. White, Phys. Scripta **T2**, 288 (1982).
50. E. A. Startsev, R. C. Davidson and M. Dorf, Phys. Plasmas **15**, 062107 (2008).
51. C. F. Driscoll and J. H. Malmberg, Phys. Rev. Lett. **50**, 167 (1983).
52. W. D. White, J. H. Malmberg and C. F. Driscoll, Phys. Rev. Lett. **49**, 1822 (1982).
53. C. F. Driscoll, J. H. Malmberg and K. S. Fine, Phys. Rev. Lett. **60**, 1290 (1988).
54. D. H. E. Dubin, Phys. Plasmas **17**, 112115 (2010).
55. D. H. E. Dubin, C. F. Driscoll and Yu. A. Tsidulko, Phys. Rev. Lett. **105**, 185003 (2010).
56. R. Pozzoli and D. Ryutov, Electromagn. Waves Electron. Syst. **3**, 12 (1998).
57. B. Paroli, *Thomson backscattering diagnostics of nanosecond electron bunches in high space charge regime*, PhD thesis (Department of Physics, University of Milano, 2012).
58. M. Amoretti, G. Bettega, F. Cavaliere, M. Cavenago, F. De Luca, R. Pozzoli, and M. Romé, Rev. Sci. Instrum. **74**, 3991 (2003).
59. B. Paroli, G. Bettega, F. Cavaliere, F. De Luca, G. Maero, R. Pozzoli, M. Romé, M. Cavenago and C. Svelto, J. Phys. D: Appl. Phys. **42**, 175203 (2009).
60. G. Bettega, F. Cavaliere, M. Cavenago, A. Illiberi, R. Pozzoli and M. Romé, Phys. Plasmas **14**, 042104 (2007)
61. B. Paroli, G. Bettega, G. Maero, M. Romé, M. Norgia, A. Pesatori and C. Svelto, Rev. Sci. Instrum. **81**, 063503 (2010).
62. G. Bettega, F. Cavaliere, A. Illiberi, R. Pozzoli, M. Romé, M. Cavenago and Yu. Tsidulko, Appl. Phys. Lett. **84**, 3807 (2004).
63. M. Romé, F. Cavaliere, M. Cavenago, M. Ikram, G. Maero, B. Paroli and R. Pozzoli, *Development of diagnostic and manipulation systems for space-charge dominated electron beams and confined electron plasmas in ELTRAP*, AIP Conf. Proc. **1521**, 291 (2013).
64. B. Paroli, F. Cavaliere, M. Cavenago, F. De Luca, M. Ikram, G. Maero, C. Marini, R. Pozzoli and M. Romé, J. Inst. **7**, P01008 (2012).
65. B. Paroli, M. Ikram, G. Maero, R. Pozzoli and M. Romé, *Observation of low-frequency oscillations in a radio frequency-stabilized plasma confined in a Malmberg-Penning trap*, Europhysics Conference Abstracts Vol. **37D**, P2.404 (2013).
66. M. Romé, F. Cavaliere, M. Cavenago, M. Ikram, F. Lepreti, G. Maero, B. Paroli and R. Pozzoli, *Experimental and numerical investigation of non-neutral complex plasmas*, AIP Conf. Proc. **1521**, 273 (2013).

67. M. Romé, F. Cavaliere, M. Cavenago, M. Ikram, G. Maero, B. Paroli, and R. Pozzoli, *Development of diagnostic and manipulation systems for space charge dominated electron beams and confined electron plasmas in ELTRAP*, AIP Conf. Proc. **1521**, 291 (2013).
68. G. Maero, F. Cavaliere, M. Cavenago, M. Ikram, F. Lepreti, B. Paroli, R. Pozzoli, M. Romé, *A set-up for the study of non-neutral complex plasma,* Europhysics Conference Abstracts Vol. **36 F**, P1.139 (2012).
69. G. Maero, B. Paroli, R. Pozzoli and M. Romé, Phys. Plasmas **18**, 032101 (2011).
70. M. Romé, F. Cavaliere, M. Cavenago, M. Ikram, G. Maero, C. Marini, B. Paroli and R. Pozzoli, *Experimental investigation of the dynamics of space-charge dominated, traveling and confined electron plasmas in a Penning-Malmberg trap*, Europhysics Conference Abstracts Vol. **36 F**, P1.184 (2012).
71. G. Maero, B. Paroli, F. De Luca, M. Ikram, R. Pozzoli and M. Romé, *Dynamical equilibrium of radio frequency-sustained electron plasma in a Penning-Malmberg trap*, Europhysics Conference Abstracts Vol. **35 G**, P1.010 (2011).
72. B. Paroli, F. Cavaliere, M. Cavenago, F. De Luca, M. Ikram, G. Maero, R. Pozzoli and M. Romé, *Thomson backscattering diagnostics of nanosecond electron bunches traveling in a Penning-Malmberg trap*, Europhysics Conference Abstracts Vol. **35 G**, P1.011 (2011).
73. T. Weilbach, K. Aulenbacher and J. Dietrich, Optical electron beam diagnostics for relativistic cooling devices. Proceedings of DIPAC 2011, Hamburg, Germany, 2011.
74. E. H. Chao, R. C. Davidson, S. F. Paul and K. A. Morrison, Phys. Plasmas **7**, 3 (2000).
75. E. Kawamura, M. A. Lieberman and A. J. Lichtenberg, Phys. Plasmas **13**, 053506 (2006).
76. P. Chabert and N. Braithwaite, *Physics of radio-frequency plasmas* (Cambridge University Press, 2011).
77. E. Fermi, Phys. Rev. **75**, 1169 (1949).
78. C. K. Birdsall and A. B. Langdon, *Plasma physics via computer simulation* (Adam Hilger, Bristol, 1991).
79. R. W. Hockney and J. W. Eastwood, *Computer simulation using particles* (Adam Hilger, Bristol, 1988).
80. G. Bettega, B. Paroli, R. Pozzoli, M. Romé and C. Svelto, Meas. Sci. Tech. **19**, 085703 (2008).
81. J. M. Dawson, Phys. Fluids **7**, 419 (1964).
82. O. Buneman, Comp. Phys. Comm. **12**, 21 (1976).
83. M. A. Lieberman and V. A. Godyak, IEEE Trans. Plasma Sci. **26**, 955 (1998).
84. C. A. Balanis, *Advanced engineering electromagnetics* (Wiley, New York, 1989).
85. *OOPIC Pro, User's Guide Version 2.0.0*, by Tech-X Corporation, Boulder, 1993.

86. D. L. Bruhwiler, R. E. Giacone, J. R. Cary, J. P. Verboncoeur, P. Mardahl, E. Esarey, W. P. Leemans and B. A. Shadwick, Phys. Rev. ST Accel. Beams **4**, 101302 (2001).
87. J. P. Verboncoeur, A.B. Langdon and N.T. Gladd, Comp. Phys. Commun. **87**, 199 (1995).
88. M. Reiser, *Theory and Design of Charged Particle Beams* (Wiley, New York, 1994).
89. R. C. Davidson, Phys. Plasmas **5**, 3459 (1998).
90. *NRL Plasma Formulary* (Naval Research Laboratory, Washington, 2001).
91. D. K. Cheng, *Fundamentals of Engineering Electromagnetics* (Addison-Wesley, 1993).
92. A. Meige, R. W. Boswell and C. Charles, Phys. Plasmas **12**, 052317 (2005).
93. L. Brillouin, Phys. Rev. **67**, 260 (1945).
94. I. A. Kotelnikov, R. Pozzoli and M. Romé, Plasma Phys. Rep. **26**, 960 (2000).
95. I. A. Kotelnikov, R. Pozzoli and M. Romé, Phys. Plasmas **12**, 092105 (2005).
96. M. Amoretti, D. Durkin, J. Fajans, R. Pozzoli and M. Romé, Phys. Plasmas **8**, 3865 (2001).
97. K. S. Fine, C. F. Driscoll and J. H. Malmberg, Phys. Rev. Lett. **63**, 2232 (1989).
98. A. B. Sefkow and R. C. Davidson, Phys. Rev. ST Accel. & Beams **10**, 100101 (2007).
99. I. Kotelnikov and M. Romé, Fus. Sci. Tech. **55**, 205 (2009).
100. G. Bettega, B. Paroli, R. Pozzoli and M. Romé, J. Appl. Phys. **105**, 053303 (2009).
101. J. D. Crawford, T. M. O'Neil and J. H. Malmberg, Phys. Rev. Lett.**54**, 697 (1985).
102. M. C. Myers et al., Rev. Sci. Instrum. **80**, (2009).
103. R. W. Gould, *Progress Report, Wave Particle Interactions in Nonneutral Plasmas*, California Institute of Technology (Pasadena, California), Office of Naval Research Grant N00014-89-J-1264 (1994).
104. C. M. Surko, R. G. Greaves, Rad. Phys. Chem. **68**, 419 (2003).
105. B. P. Cluggish, J. R. Danielson and C. F. Driscoll, Phys. Rev. Lett. **81**, 2 (1998)
106. H. Matzner and S. Levy, *Basic RF technic and Laboratory Manual* (2002).